Universitat Autònoma de Barcelona

QUANTUM INFORMATION IN LATTICES

Bruna Gabrielly

UAB, Department of Physics

ICN2 & ICFO

PhD thesis

QUANTUM INFORMATION IN LATTICES

Supervisors: Prof. Antonio Acín, Prof. Daniel Cavalcanti,

Prof. Stephan Roche

Tutor: Prof. John Calsamiglia

Candidate: Bruna Gabrielly

June 2022

Quantum Information in Lattices

Universitat Autònoma de Barcelona

Facultat de Ciències

Department of Physics - PhD program

A thesis submitted for the degree of *Doctor of Philosophy in Physics.*

Supervisors: Prof. Antonio Acín, Prof. Daniel Cavalcanti, Prof. Stephan Roche.

Tutor: Prof. John Calsamiglia

By

Bruna Gabrielly de Moraes Araújo

BSc. in Physics, Federal University of Pernambuco - Recife, Brazil.

MSc. in Physics, Federal University of Pernambuco - Recife, Brazil.

June, 2022

Abstract

This Ph.D. manuscript is divided into two chapters, related to two different scientific scopes, but with the common point of exploring entanglement phenomena in complex matter or lattices. In the first part of my Ph.D., I did exploratory research studying the origin and formation of intra-particle entanglement, specifically spin-pseudospin bipartite degree of freedoms, in some graphene-based platforms. The intra-particle entanglement is one of the signatures of the quantum spin transport in Dirac matter in the presence of Rashba spin-orbit coupling (pseudo-magnetic field) term and other spin-orbit terms, in the case of the graphene on substract of heterostructures. The second part is a study about effective ways to perform partial quantum state tomography for many-body physics. We adapted an original method of quantum overlapping tomography for qubits and fermions for finite lattices. The main goal of our adaptation is to provide k-particles reduced density matrix to recover the physical observables via local measurements for being applied to quantum simulation in real quantum devices. Consequently, we bridged two research areas usually studied separated, graphene physics and quantum tomography in lattices. Each chapter derives from already published or preprint papers and can be considered self-contained.

Keywords: *Intra-particle Entanglement, Quantum Spin Transport, Random Matrices, Dirac Matter, Reduced Density Matrix, Partial Quantum State Tomography, Local Quantum Overlapping Tomography, Finite and Periodic Lattices, Quantum Computing.*

Contribution during the PhD

Presented in this thesis

- Bruna Gabrielly de Moraes, Aron W. Cummings, Stephan Roche, *Emergence of Intra-Particle Entanglement and Time-Varying Violation of Bell's Inequality in Dirac Matter,* **Phys. Rev. B 102, 041403 (2020).**

- Bruna G. M. Araújo, Márcio M. Taddei, Daniel Cavalcanti,Antonio Acín, *Local overlapping quantum tomography*, **preprint: 2112.03924 [quant-ph]**.

- Axel Pérez-Obiol, Adrián Pérez-Salinas, Sergio Sánchez-Ramírez, Bruna G. M. Araújo, Artur Garcia-Saez, *Adiabatic quantum algorithm for artificial graphene,* **preprint: 2204.03013 [quant-ph].**

Contents

Part I.

Quantum entanglement in graphene-based platforms.

1. Intra-particle entanglement as a hidden variable in spin dynamics for graphene-based systems.

*Most part of the sections 1.1, 1.3 and 1.5 are based in the collaborative work: "**Emergence of Intra-Particle Entanglement and Time-Varying Violation of Bell's Inequality in Dirac Matter**", published in Phys. Rev. B 102, 041403 (2020) , by Bruna Gabrielly de Moraes, Aron W. Cummings, Stephan Roche. The first part of PhD was of purely exploratory research, and section 1.4 is related to some unpublished outcomes.*

1.1. Introduction

The importance of quantum entanglement was sparked by the seminal *gedanken* experiment proposed in 1935 by Einstein, Podolsky and Rosen [1], who in an attempt to demonstrate the incompleteness of quantum mechanics actually inspired the study of nonlocal correlations between distant particles [1, 2, 3].

Beyond the fascinating fundamental debate, which found its resolution in the violation of Bell's inequality [4, 5], quantum entanglement between internal degrees of freedom of particles has become key for understanding emerging topological phases in many-body physics [6, 7], as well as for controlling quantum states in the quest to realize quantum computing applications [8, 9, 10].

Spin is a quantity that can be entangled to create nonlocal quantum correlations, and there have been many proposals to generate spin-entangled electrons [11, 12, 13] or electron-hole pairs [14, 15, 16] in solid state systems.

These have stimulated a variety of experimental studies, including attempts to generate entanglement through the splitting of Cooper pairs [17, 18, 19, 20]. To date

however, the verification of nonlocal quantum correlations between fermions, via a violation of Bell's inequality, remains challenging [21, 22, 23].

In contrast, by taking advantage of *intra*-particle entanglement between the spatial and spin degrees of freedom of a single neutron, the violation of Bell's inequality has been demonstrated in neutron interferometry experiments [24, 25]. Finally, there are many other potential combinations of intra- and inter-particle entanglement, as well as proposals to swap between them [26, 27, 28, 29].

Two-dimensional Dirac materials offer true novelty in this context. In addition to spin, electrons in Dirac materials such as graphene carry other degrees of freedom, including sublattice (aka pseudospin), valley, and layer (in bilayer graphene) [30, 31, 32], which opens new possibilities for intra-particle entanglement. Sharing the mathematical structure of spin, these degrees of freedom can become entangled with one another and with spin in the presence of proximity effects [33].

Entanglement of this kind means that manipulating one degree of freedom will result in an effect on another. For example, when graphene is on a substrate, Rashba spin-orbit coupling (SOC) leads to entanglement between the spin and pseudospin [34]. Identified as a source of spin dephasing in pristine graphene [35, 36, 37], this is a clear example of the effect of intra-particle entanglement on a measurable spin transport property.

Finally, the eigenstates of bilayer graphene also exhibit strong sublattice-layer entanglement near the charge neutrality point [38]. However, there are currently no studies of the formation and dynamics of intra-particle entanglement in 2D Dirac materials.

As the main result of this chapter, we explore the origin, dynamics, and magnitude of intra-particle entanglement between the spin and pseudospin degrees of freedom of electrons propagating in graphene. We show that Rashba SOC drives the generation and time evolution of this entanglement, which emerges regardless of the initial quantum state.

It is primarily shown that the emergence of an intra-particle entanglement is thus a general feature of graphene on a substrate, opening the possibility of its measurement or exploitation for quantum information processing.

This chapter is structured as follows:

- In **Sec. 1.2**, we present the state of art and some concepts to understand the main results of this chapter.

- In **Sec. 1.3** we present our main results for Rashba spin-orbit coupling graphene monolayer.

- In **Sec. 1.4** we present some non-published results about Rashba SOC graphene on a substract and how some spin-orbit terms act suppressing the entanglement of these systems.

- In **Sec. 1.5** we make our concluding remarks.

1.2. Preliminaries

1.2.1. Dirac matter

Recently, a new class of materials has emerged with the discovery of graphene, a stable crystal formed only by a single layer of carbon. The "honeycomb" hexagonal crystal lattice (with the atoms distributed on the vertices of each hexagon) and its single atom thickness result in exceptional electronic properties, such as the quantum Hall effect with unusual quantization [39, 40] .

Graphene is a transparent conductor [41], mathematically described from the analogy with particle physics that includes an exotic type of tunneling, initially predicted by Oscar Klein, when massless relativistic particles tunnel without backscattering through arbitrarily high and wide potential barrier [42]. Low energy states in graphene have been shown to give birth to massless quasi-relativistic particles which behave similarly, and become unimpeded in presence of long range disorder potentials. Klein tunneling was theoretically discussed [43], and experimentally proven in Graphene [44] and as a result, electronic transport in graphene can be ballistic over unprecedented distances.

The 2010 Nobel Prize in Physics was awarded the two scientists who first isolated graphene. They are Andre K. Geim and Konstantin S. Novoselov, both from the University of Manchester in the United Kingdom. Let us direct our gaze to the incredible variety of carbon in nature. This element is of crucial importance for life, it is present from DNA and in all life on earth.

Furthermore, carbon can exist in many forms, the most common being graphite which has a hexagonal structure. Under high pressures diamond is formed, which is the metastable form of carbon. A new form of molecular carbon is fullerene. The most common is the C-60 composed of 60 carbon atoms, its topology resembles a football bag. The discovery of fullerene was awarded the 1996 Nobel prize in chemistry. An almost one-dimensional form of carbon has been known for several decades [45] and walled nanotubes since 1993 [46, 47]. These can be formed from sheets of graphene, which are rolled up to form tubes, and their ends are half spherical in the same way as fullerenes.

The electronic and mechanical properties of a single metallic nanotube have many similarities with graphene. Graphite is known to consist of hexagonal carbon sheets that are stacked on top of each other, but it was believed for many years that a single sheet would not be stable under ambient conditions.

It therefore came as a great surprise to the physics community when in October 2004, Konstantin Novoselov, Andre Geim and their collaborators [48] showed that a single layer can be isolated and transferred to another substrate. In July 2005 they published electrical measurements in a single layer [49]. This single layer of carbon is what we call graphene. Graphene, a two dimensional carbon allotrope, has proven over the last decade to be a truly wonder material. Despite its simple structure and chemical composition, its use in a variety of fields such as coatings, sensors, energy, biomedicine, photonics, and optoelectronics has demonstrated the richness of its properties and its potential industrial impact [50].

1.2.2. Dirac equation: from profound to applied

Surprisingly, Dirac materials have built a bridge between high-energy and condensed matter physics, enabling the exploration of relativistic phenomena at low energy and in a conventional experimental laboratory.

We start by introducing the Dirac's relativistic equation for the electron, brought from its original formulation in quantum field theory in the (3+1) - dimension, and we will demonstrate how an low-energy quasiparticle in graphene can be described effectively by massless Dirac Hamiltonian (2+1) - dimensions.

We will also describe briefly the topological nature of the intriguing **Dirac points**, which are related in the momentum space to **topological winding numbers**. We will unveil the symmetries that stabilize their existence. We are concern about them because our intraparticle entanglement arises from these electronic features.

Then we will proceed to demonstrate how symmetry breaking elements induce intriguing phenomena such as the generation of pseudo-magnetic fields, which can be connected to the presence of Rashba SOC term, for instance, responsible to emergence of the intraparticle quantum correlations.

Quantum field theory results from the unification of quantum mechanics and relativity, and its fundamental equation for single electron has been derived by Paul M. Dirac in 1928 [51]. The Dirac equation has profound consequences such as the prediction of antimatter and the explanation of the origin of the spin degree of freedom. To capture its essential derivation, it is instructive to start with the

Schrödinger equation:

$$i\hbar\frac{\partial}{\partial t}\psi_S\left(\overrightarrow{r},t\right)=\frac{-\hbar^2}{2m}\nabla^2\psi_S\left(\overrightarrow{r},t\right). \tag{1.1}$$

This expression can be built from non-relativistic energy-momentum relation dispersion $E=\left|\overrightarrow{p}\right|^2/2m$, converting the classical variables to operators such as $\overrightarrow{p}\rightarrow -i\hbar\nabla$ and $E\rightarrow i\hbar\partial_t$. These operators act on a complex scalar wave function which is interpreted as a probability amplitude, and its square modulo as an probability density.

As we know, in the relativistic theory, space and time are linked, thus, a relativistic version for the Schrödinger equation requires that exists a symmetry between the the first derivates of the space and time.

Klein and Gordon were the first to proposed a tentative solution for a relativistic quantum mechanics equation, by inserting the Einstein's energy-momentum relation $E^2=c^2\left|\overrightarrow{p}\right|^2+m^2c^4$ into a wave equation, such that:

$$\frac{1}{c^2}\frac{\partial^2}{\partial t^2}\psi_{KG}\left(\overrightarrow{r},t\right)=\left(\nabla^2-\frac{m^2c^2}{\hbar^2}\right)\psi_{KG}\left(\overrightarrow{r},t\right), \tag{1.2}$$

where c is the speed of light. Unfortunately, while the Klein-Gordon equation is Lorentz-invariant, it presented a serious problem, the probability density was no longer positive definite. In other words, the relativistic scalar ψ_{KG} cannot be described describe as a probability amplitude as in the Schrödinger's equation.

To solve this issue, Dirac thought in a equation that was in first order in the space and time, keeping the Lorentz-invariance and providing a positive-definite probability density. He took the square-root of the Klein- Gordon formulation by conjecturing a first-order wave equation of the form:

$$i\hbar\frac{\partial}{\partial t}\psi_D\left(\overrightarrow{r},t\right)=\left(-i\hbar c\gamma\cdot\overrightarrow{\nabla}+\gamma_0 m^2c^2\right)\psi_D\left(\overrightarrow{r},t\right) \tag{1.3}$$

Considering $\gamma=[\gamma_1,\gamma_2,\gamma_3]$ and γ_i $(i=0,1,2,3)$ are mathematical objects, which must obey stringent. The algebraic properties which must be obeyed by γ_i, include that they must anti commute with one another

$$\gamma_i^2=1,\qquad \{\gamma_i,\gamma_j\}=2\delta_{ij}1, \tag{1.4}$$

where 1 is the identity and δ_{ij} is the kronecker delta function. Dirac found that ordinary number fail to obey this requirement, but 2×2 Pauli matrices can make his equation consistent

$$\sigma_x = \begin{pmatrix} 0 & 1 \\ 1 & 0 \end{pmatrix}, \qquad \sigma_y = \begin{pmatrix} 0 & -i \\ i & 0 \end{pmatrix}, \qquad \sigma_z = \begin{pmatrix} 1 & 0 \\ 0 & -1 \end{pmatrix}. \tag{1.5}$$

Thus, with this set of matrices we can start to glimpse a connection between relativity and quantum mechanics to describe the electron with intrinsic spin $1/2$ angular momentum. But, to satisfy all conditions for $(3+1)$ dimensions we need four matrices instead of the sole Pauli's matrices. To obtain the full description in this dimension, we need 4×4 matrices that can be built from Pauli matrices and identity operator, such as

$$\gamma_x = \begin{pmatrix} 0 & \sigma_x \\ \sigma_x & 0 \end{pmatrix}, \qquad \gamma_y = \begin{pmatrix} 0 & \sigma_y \\ \sigma_y & 0 \end{pmatrix}, \qquad \gamma_z = \begin{pmatrix} 0 & \sigma_z \\ \sigma_z & 0 \end{pmatrix}, \tag{1.6}$$

$$\gamma_0 = \begin{pmatrix} 1_2 & 0 \\ 0 & 1_2 \end{pmatrix}. \tag{1.7}$$

where 1_2 is the 2×2 identity matrix, and which implies that the electron wavefunction ψ_D can no longer be a scalar, but a 4- component spinor. Surprisingly, the low-energy limit of Dirac's relativistic equation recovered the phenomenological Pauli's theory of the electron, defined by a 2-components wavefunction capturing the $1/2$ spin degree of freedom, and which was shown to explain the anomalous gyromagnetic ratio.

Regarding the full relativistic theory, what happens with the other two components of the 4 component spinor?

These components predicted by the Dirac theory embed additional solutions for negative energies. These negative energies in the classical theory are dropped out as unphysical.

But, inspired by the ideas of condensed matter from that time about hole - particle symmetry, Dirac also posed that quantum theory with small perturbation could induce transitions from the positive-energy to negative-energy states.

Remarkably, he proposed that this "empty" space that is part of the 4-spinor

solution, it is not empty at all, it is filled by electrons with negative-energy states, also called Dirac sea, which ones are stabilized by Pauli's exclusion principle. Thus, he presented a physical solutions for the problem [51]. From this, he conjectured the existence of the anti-electron which he viewed as a hole in the Dirac sea.

This was a dare prediction because there was no empirical evidence to suggest the existence of anti-particle, a couple of years latter (1932), Carl Anderson observed anomalous cosmic-ray tracks via a cloud chamber that matched the mass to charge ratio of an electron, but being in opposite direction, he called this anti-particle, positron due to their positive charge.

1.2.3. Graphene

It was quite natural to expect that the Dirac's relativistic equation, described in the previous section, will not play any important role to describe condensed matter physics. However, as already shown for non-relativistic quantum mechanic, particles propagating in a crystal may acquire emerging properties (such as an effective mass) different from their free space characteristics.

Indeed, conventional band theory allows to describe particles moving in a crystal through a Schrödinger equation with a renormalized effective. In Dirac materials, we can find a much more exotic scenario, where quasi-particles are governed by a pseudo-relativistic Dirac equation and a straightforward way to show this is to derive an effective model from a tight-binding model [52]

Two-band model for graphene:

To describe the low-energy properties of particles in graphene, let us observe first that the crystallographic structure of the graphene is not a Bravais lattice. The carbon atoms are located at periodic positions $\overrightarrow{R}_A = \overrightarrow{R} + \overrightarrow{d}_A$ and $\overrightarrow{R}_B = \overrightarrow{R} + \overrightarrow{d}_B$, which form two inequivalent hexagonal sublattices that we label A and B, respectivelly. Thus, the basis vector are

$$\overrightarrow{d}_A = \frac{a_{cc}}{2}\left[0, -1\right], \quad \overrightarrow{d}_B = \frac{a_{cc}}{2}\left[0, 1\right], \tag{1.8}$$

located at the positions of the carbon atoms within the unit cell, where $a_{cc} \approx 1.42\overset{o}{A}$ is the carbon-carbon distance. Furthermore, $\overrightarrow{R} = l_1\overrightarrow{a}_1 + l_2\overrightarrow{a}_2$ represent the set of

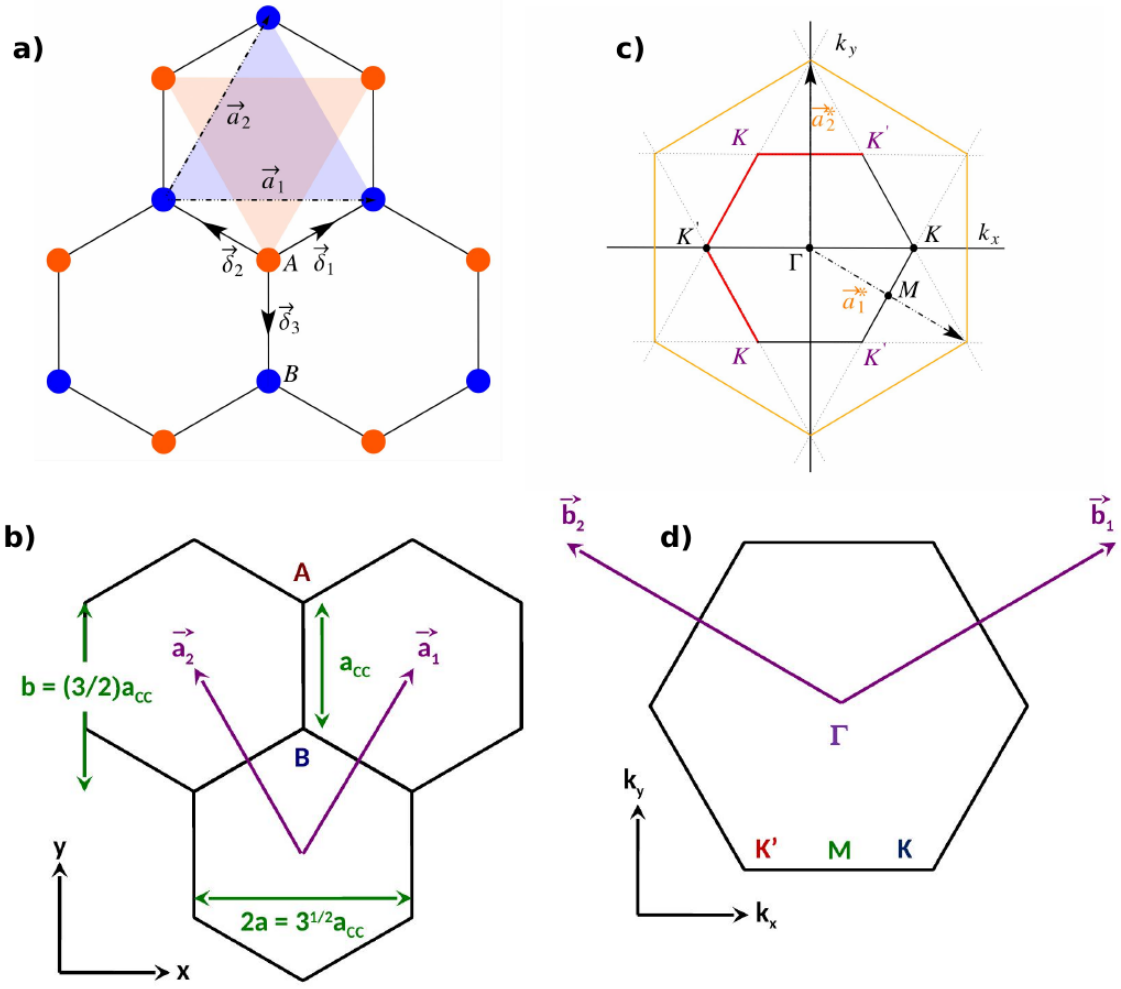

Figure 1.1.: ***Crystallographic structure (real and reciprocal space) of a monolayer graphene. Left*** *(**a)** and **b)**): Sketch of the monolayer graphene which is composed of two inequivalent hexagonal sub-lattices of carbon atoms which is called A and B respectivelly. The primitive lattice vectors are* $\vec{a}_1$ *and* $\vec{a}_2$*. The essential electronic properties of graphene can be extracted with a simple tight-binding model where t is the nearest-neighbor hopping parameter.* ***Right*** *(**c)** and **d)**): The corresponding first Brillouin zone (**FBZ**) in momentum space where the high-symmetry points are labelled* $\vec{b}_1$ *and* $\vec{b}_2$ *form the primitive reciprocal lattice vectors.*

lattice translation vectors describing the underlying hexagonal Bravais lattice, where $l_1, l_2 \, \epsilon \, \mathbb{Z}$ are integers and

$$\overrightarrow{a}_1 = \frac{\sqrt{3}}{2} a_{cc} \left[-1, \sqrt{3}\right], \qquad \overrightarrow{a}_2 = \frac{\sqrt{3}}{2} a_{cc} \left[1, \sqrt{3}\right], \tag{1.9}$$

are the primitive reciprocal lattice vectors which define the Brillouin zone shown in the figure 1.1b). The basic electronic properties of graphene are captured by a single-orbital, spinless tight-binding which in the language of second quantization, reads

$$H = -t \sum_{R_B} \sum_{n=1}^{3} b^{\dagger}_{R_B} a_{R_B + e_n} + h.c. \tag{1.10}$$

Where $a^{\dagger}_{R_A}$ and $a^{\dagger}_{R_B}$create electron in the $2p_z$ orbitals located at $\overrightarrow{R}_A$ and $\overrightarrow{R}_B$ on the A and B sublattices. In this approach all onsite energies of the $2p_z$ orbital as equals (to zero) and defining the reference energy. Taking $t \approx 2.7$ eV is the nearest-neighbor hopping parameter which dictates the energy scale of the bands, and

$$\overrightarrow{e}_1 = a_{cc} \left[0, -1\right], \qquad \overrightarrow{e}_2 = a_{cc} \left[\sqrt{3}, 1\right], \qquad \overrightarrow{e}_3 = a_{cc} \left[-\sqrt{3}, 1\right], \tag{1.11}$$

are the nearest-neighbor vectors that connect the inequivalent sublattices. We can exploit the discrete translational symmetry of the lattice by introducing the Fourier transform of the operators

$$a^{\dagger}(k) = \frac{\sqrt{\tilde{w}}}{2\pi} \sum_{R_A} a^{\dagger}_{R_A} e^{i \overrightarrow{k} . \overrightarrow{R}_A}, \qquad b^{\dagger}(k) = \frac{\sqrt{\tilde{w}}}{2\pi} \sum_{R_B} b^{\dagger}_{R_B} e^{i \overrightarrow{k} . \overrightarrow{R}_B}, \tag{1.12}$$

which create Bloch functions that extend over the A and B sublattices. Consider $\overrightarrow{k} = [k_x, k_y]$ is the 2D Bloch wave-vector that is restricted to the **FBZ** shown (Fig. 1.1, right panel), and $\tilde{w} = 3\sqrt{3} a^2_{cc}/2$ is the area of the unit cell shown in the Fig. 1.1 (left panel). Using the Eq. 1.12 we can easily diagonalize the tight-binding Hamiltonian described in the momentum space which can be written in matrix form

as

$$H = \int \int_{FBZ} d^2k \psi^\dagger (k) H (k) \psi (k), \tag{1.13}$$

where $\psi^\dagger (k) = \left[a^\dagger (k), b^\dagger (k)\right]$ is a spinor operator. The 2×2 single-particle Bloch Hamiltonian in the sublattice space is

$$H (k) = \begin{pmatrix} 0 & f (k) \\ f^* (k) & 0 \end{pmatrix}, \tag{1.14}$$

where the off-diagonal matrix elements are given by

$$f (k) = -t \sum_{n=1}^{3} e^{-i \overrightarrow{k} \cdot \overrightarrow{e_n}}. \tag{1.15}$$

Eq. (1.14) can be diagonalized to obtain the spectrum of the electronic bands

$$E_\lambda (k) = \lambda |f (k)|, \tag{1.16}$$

being $\lambda = \pm 1$, regarding the valence bands we have $\lambda = -1$ and to the conduction bands $\lambda = 1$. Corresponding spinor eigenstates:

$$|\psi_\lambda (k)\rangle = \frac{1}{\sqrt{2}} \begin{pmatrix} 1 \\ \lambda e^{i\varphi(k)} \end{pmatrix}, \tag{1.17}$$

the above eigenvector encodes the **pseudospin degree of freedom**, where the two components of the vector describe the relative amplitude and phase of the eigenvector on the two inequivalent sublattices. Representing the spinor eigenstate of the pseudo-spin vector on the Bloch sphere, we have:

$$S_\lambda (k) = \langle \psi_\lambda (k) | \sigma | \psi_\lambda (k) \rangle = \lambda \left[\cos \varphi (k), \sin \varphi (k), 0\right]. \tag{1.18}$$

Being $\overrightarrow{\sigma} = [\sigma_x, \sigma_y, \sigma_z]$ is the vector of the Pauli matrices and the azimutal angle

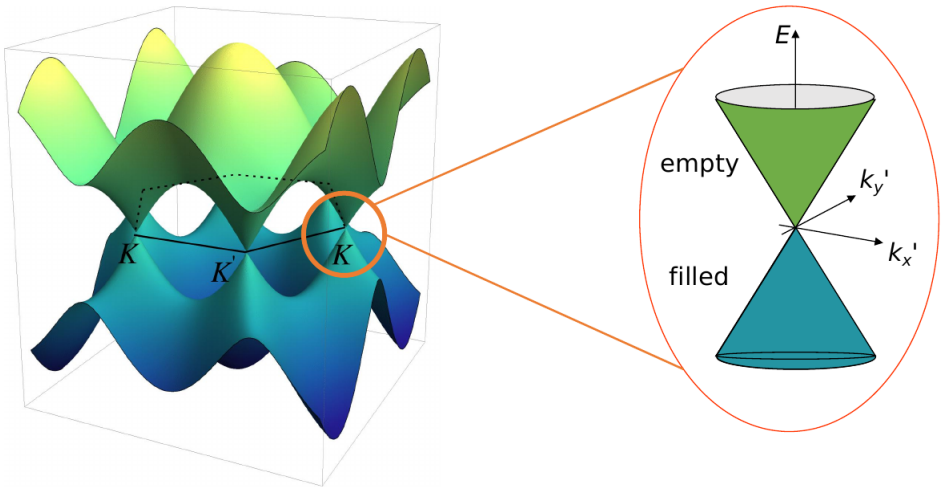

Figure 1.2.: *Graphene band structure and Dirac cone and its symmetry electron-hole. In this approach the bands are symmetric with respect to the valence and conduction bands. The linear dispersion relation close to the K^+ and K^- in the FBZ in 2D that originate the "Dirac cones" as shown in the right. Close to these cones k_x and k_y are used to denote the shift from the corresponding K(K') point.*

is given by

$$\varphi(k) = \arg\left[f^*(k)\right]. \tag{1.19}$$

Fig. 1.2 presents the electronic band structure within the nearest-neighbor approximation. The most notable fact is that the conduction and valence bands are degenerate at the corners of the **FBZ**, specifically at the so-called Dirac points, and it seems like we have six Dirac points, but only two of them are inequivalents while the others are regarding the same states - related to the reciprocal lattice vectors. In our work for graphene clean and graphene/TMDC's heterostructures we will focus in the Dirac points located at

$$K(K') = \left[\pm\frac{2\pi}{3\sqrt{3}a_{cc}}, \frac{2\pi}{3a_{cc}}\right] \tag{1.20}$$

1.2.4. Effective Dirac physics

In pristine graphene the two bands are half filled and the Fermi Energy is located

at the charge neutrality point (Dirac point-zero energy reference). As in most of problems of condensed matter emerging from a quantum field theory formulation we usually derive a mapping to an a effective field theory.

Thus to access in a very simple way the electronic quasi-particles near Fermi energy zero, we will derive an effective Hamiltonian to obtain proper knowledge of physics in this region. For this we expand the Eq. (1.15) around K/K' points as $\widetilde{\mathbf{k}} = k + \tau K$:

$$f_\tau\left(\widetilde{\mathbf{k}}\right) \simeq \hbar\nu_F\left(\tau k_x - ik_y\right), \tag{1.21}$$

where $\nu_F = 3ta/2\hbar$ is the Fermi velocity. Therefore, we can write the effective Hamiltonian near the Fermi energy as:

$$H_{eff} = \sum_{\tau=\pm 1}\int\int d^2k\psi_\tau^\dagger\left(\widetilde{\mathbf{k}}\right) H_\tau\left(\widetilde{\mathbf{k}}\right)\psi_\tau\left(\widetilde{\mathbf{k}}\right), \tag{1.22}$$

being $\psi_\tau^\dagger\left(\widetilde{\mathbf{k}}\right) = \left[a_\tau^\dagger(k), b_\tau^\dagger(k)\right]$ is the spinor operator in each valley. Therefore, the effective single-particle Hamiltonian for a unique K valleys reads

$$H_+\left(\widetilde{\mathbf{k}}\right) = \hbar\nu_F\begin{pmatrix} 0 & k_x - ik_y \\ k_x + ik_y & 0 \end{pmatrix} = \hbar\nu_F\,\overrightarrow{\sigma}\cdot\overrightarrow{k}, \tag{1.23}$$

while the effective single-particle Hamiltonian regarding the K' point is

$$H_-\left(\widetilde{\mathbf{k}}\right) = \hbar\nu_F\begin{pmatrix} 0 & -k_x - ik_y \\ -k_x + ik_y & 0 \end{pmatrix} = -\hbar\nu_F\,\overrightarrow{\sigma}\cdot\overrightarrow{k}. \tag{1.24}$$

thus, via this effective model, the low-energy quasiparticles within each valley are effectively described by a pseudo-relativistic Dirac Hamiltonian. Knowing that the fermions in graphene exist in a 2+1 dimensional space, the effective Hamiltonians described above are generated by 2×2 Pauli matrices also described in Dirac equation formulation in previous section.

Besides, we must point out that the matrix structure of the Hamiltonian does not originate from real spin of the electron, when we are considering this kind of graphene system. However, the physics of this effective Hamiltonian emerges from the presence of the two inequivalent sublattices, precisely the pseudo-spin degree of freedom. Thus the Pauli matrices act in the sublattice space.

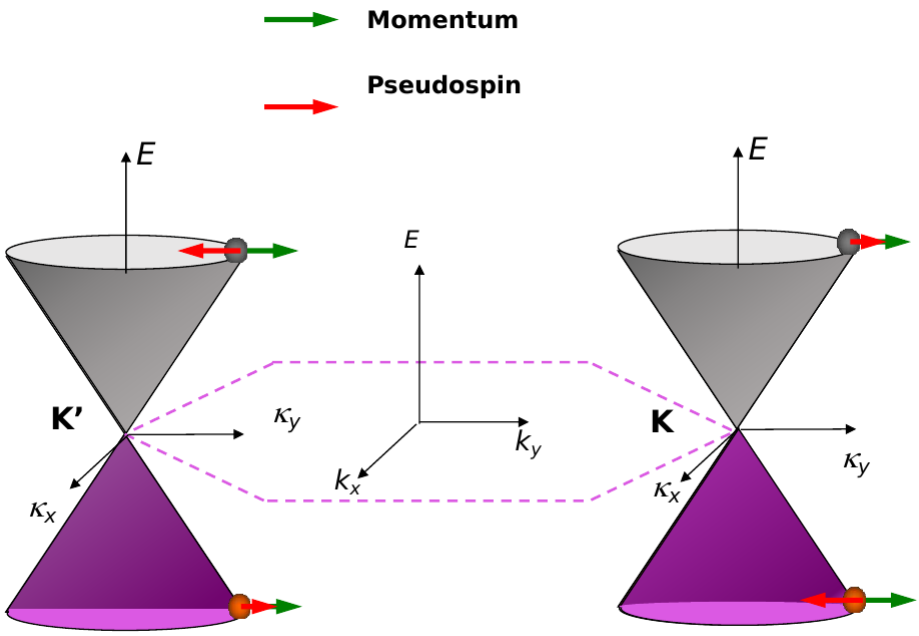

Figure 1.3.: *Pseudospin and momentum. The two inequivalent Dirac cones at K^+ and K^- points of the first Brillouin zone, together with direction of the pseudospin parallel or antiparallel to the momentum p of selected energies in conduction and valence bands.*

As we can realize, the Pauli matrix σ_z does not appear in the Hamiltonian of the graphene. This means that the electronic quasi-particles behave like massless Dirac fermions, described by a pseudo-relativistic linear spectrum near their Dirac points K(K') as

$$E_\lambda\left(\widetilde{\mathbf{k}}\right) = \lambda\hbar\nu_F\left|\widetilde{\mathbf{k}}\right|, \tag{1.25}$$

this dispersion relation clearly determines massless Dirac cones. Consequently, the massless Dirac fermions exhibit a kind of chirality where the pseudo-spin is intrinsically locked to momentum.

Thus, the spinor eigenstate of an effective Hamiltonian for each valley to be considered is described by

$$\left|\psi_{\tau\lambda}\left(\widetilde{\mathbf{k}}\right)\right\rangle = \frac{1}{\sqrt{2}}\begin{pmatrix} 1 \\ \tau\lambda e^{i\tau\varphi\left(\widetilde{\mathbf{k}}\right)} \end{pmatrix}, \tag{1.26}$$

with the pseudo-vector described by the same expression of the Eq. (1.18) just

including the proper sign regarding the Dirac point to be considered and $\varphi(k) = \arctan\left(\frac{k_x}{k_y}\right)$. For the K valley, the energy eigenstates are simultaneous eigenstates of the chirality operator

$$\overrightarrow{\sigma} \cdot \hat{k} \left|\psi_{+\lambda}\left(\widetilde{\mathbf{k}}\right)\right\rangle = \lambda \left|\psi_{+\lambda}\left(\widetilde{\mathbf{k}}\right)\right\rangle \tag{1.27}$$

where the pesudospin is pointing out in the opposite direction to the momentum as presented in the Fig. 1.3. This chiral nature of these particles are responsible for many intriguing properties in **graphene Klein tunneling**, **anomalous weak antilocalization effects**, **zero energy Landau level** and **half-integer Quantum Hall effect**, and so forth [52].

These features will not be explored here in more details, but are important its understanding for creating protocols of detection of entanglement or use these intra-particle quantum correlation as usefull resource in these 2D physical platforms.

1.2.5. Topological features of the Dirac points

In the prior section, we have described how to derive the continuous (effective) massless Dirac Hamiltonian for graphene, starting from a tight-binding model, and introducing the pseudopsin degree of freedom, which will become the resource for a new kind on intraparticle entanglement.

Indeed, importantly, in addition to the exotic low-energy electronic properties of graphene, the Dirac points are also unique in the sense that they are the natural habitat of the spin-pseudospin entanglement under the action of a pseudo-magnetic field like the one associated to a Rashba spin-orbit coupling field.

Therefore, it is essential to understand how stable are these Dirac points to perturbations and to understand the symmetries which protect their existence.

In this way, we will extract important lessons about how we must proceed in the future regarding the study quantum computing protocols or simulations based on the real and artificial graphene and Dirac-like, for example. With this goal, it is important to understand how robust are the properties of the massless Dirac fermions.

What will happen if we try to change the features of the pristine graphene? Like if we consider long-range hopping between distant neighbors, change the on-site energies of the sublattices A, B, or even consider anisotropic hopping parameters? Will graphene's chirality be fixed, or the Dirac fermions be massless?

To analyze in-depth those questions we can come back to the effective Hamiltonian

described in previous section.

$$H(k) = \begin{pmatrix} \varrho_o(k) + \varrho_z(k) & \varrho_x(k) - i\varrho_y(k) \\ \varrho_x(k) + i\varrho_y(k) & \varrho_0(k) - \varrho_z(k) \end{pmatrix}, \tag{1.28}$$

$$= \varrho_o(k)\, 1_2 + \overrightarrow{\sigma} \cdot \overrightarrow{\varrho}(k). \tag{1.29}$$

Being $\overrightarrow{\varrho}(k) = [\varrho_x(k), \varrho_y(k), \varrho_z(k)]$, and $\varrho_i(k) \ \epsilon \ \Re$ the spectrum of the Hamiltonians is

$$E_\lambda(k) = \varrho_o(k) + \lambda\,|\varrho(k)| = \varrho_o(k) + \lambda\sqrt{\varrho_x^2(k) + \varrho_y^2(k) + \varrho_z^2(k)}, \tag{1.30}$$

representing the spinor eigenstates via pseudo-spin vector on the Bloch sphere which is described by

$$S_\lambda(k) = \lambda\widehat{\varrho}(k) = \frac{\lambda}{|\widehat{\varrho}(k)|}\left[\varrho_x(k), \varrho_y(k), \varrho_z(k)\right]. \tag{1.31}$$

By inspecting the last two expressions above, we can say that the diagonal term $\varrho_o(k)$ modifies the spectrum and consequently can modify suddenly the properties of the system. However this term does not affect the spinor eigenstate and plays no role in determining the stability of the Dirac points.

Invoking the Von Neumann-Wigner theorem [53], in order to have an accidental degeneracy that is not by virtue of any symmetries, we need to tune all parameters of the vector $\overrightarrow{\varrho}(k)$. The degeneracy criterium requires that all coefficients of the anticommuting Pauli matrices disappear, thus

$$\varrho_x(k) = 0, \qquad \varrho_y(k) = 0, \qquad \varrho_z(k) = 0. \tag{1.32}$$

But in Dirac matter we just have a 2D system where the momentum $k = [k_x, k_y]$ varied along the FBZ in two directions. As consequence of this, the band degeneracies are unstable in 2D systems, which means that is required a sensitive tuning of parameters of these systems is required.

We will in this section, try to understand this instability from the topological point of view. Consider a closed contour Γ in the FBZ where the bands are gapped and

taking $k \to \overrightarrow{\varrho}(k)$ defines a map from a circle $S^1 \to S^2$ to the Bloch sphere. Since all points of sphere can be continuously deformed to a unique point (trivial group) $\Pi_1(S^2) = 0$.

Therefore, ***there is no exists topological invariants, in such 2D systems, that can protect the band crossing.*** Here we need to point out that this conclusion is regarding short-range perturbations, which disrupt sublattice symmetry and consequently leads to gap opening.

Differently, for long-range perturbations such topological protection is maintained. We will see, in our results presented here, with the additions of the SOC terms in graphene-based Hamiltonians, will profoundly affect the electronic structures, spin textures and spin dynamics of particles.

In the absence of interacting terms like SOC, we can consider some symmetries which can add constraints that stabilize the Dirac points in graphene.

In general, 2D systems has no crossing points. The reason that graphene has crossing points is because the σ_z term is not present in the Hamiltonian without SOC.

In what follows, we will explain a bit the role of the time-reversal $\Gamma: \quad t \to -t$, and spatial inversion $\Theta: [x, y] \to [-x, -y]$ symmetries on the low-energy electronic properties (following Ref. [54]).

Spatial inversion symmetry:

The hexagonal lattice has a spatial symmetry Θ, regarding the center of the carbon-carbon bonds and hexagons. This operation swaps the sublattices A and B, and can be represented by the unity operator: $U_\Theta = \sigma_x$. The Θ operation also transforms $k \to -k$, inducing a constraint on the Bloch Hamiltonian:

$$\Theta: U_\Theta H(k) U_\Theta^{-1} = \sigma_x H(k) \sigma_x = H(-k), \tag{1.33}$$

which is satisfied if

$$\varrho_0(k) = \varrho_0(-k), \ \varrho_x(k) = \varrho_x(-k), \ -\varrho_y(k) = \varrho_y(-k), \ -\varrho_z(k) = \varrho_z(-k).$$

Time - reversal symmetry:

As the time-reversal symmetry Γ does not affect the sublattices (A, B), it will

be represented by an anti-unitary operator $U_\Gamma = \Upsilon$ which is related the complex conjugation operation. Furthermore, Γ also transforms $k \to -k$, thus, the constraint on Hamiltonian regarding this operation reads

$$\Gamma : U_\Gamma H(k) U_\Gamma^{-1} = H^*(k) = H(-k), \tag{1.34}$$

which is satisfied if

$$\varrho_0(k) = \varrho_0(-k),\ \varrho_x(k) = \varrho_x(-k),\ -\varrho_y(k) = \varrho_y(-k),\ \varrho_z(k) = \varrho_z(-k). \tag{1.35}$$

From this, we can conclude that the application of a unique operation being Γ or Θ, is not sufficient to provide a condition of stability at Dirac point, given the operations acting on the Bloch Hamiltonian at k or $-k$, these operations does not impose a constraint in the general momentum of the Hamiltonian. However, if we apply the product of these two operations, we have

$$\Theta\Gamma : (U_\Theta U_\Gamma) H(k) (U_\Theta U_\Gamma)^{-1} = \sigma_x H^*(k) \sigma_x = H(k), \tag{1.36}$$

which is satisfied if

$$\varrho_0(k) = \varrho_0(k),\ \varrho(k) = \varrho_x(k),\ \varrho_y(k) = \varrho_y(k),\ -\varrho_z(k) = \varrho_z(k). \tag{1.37}$$

Therefore, this $\Theta\Gamma$ symmetry requires that the σ_z term of the Hamiltonian vanish, thus

$$\varrho_z(k) = 0, \tag{1.38}$$

with this, we showed that is possible to have stable Dirac points in 2D in the presence of the $\Theta\Gamma$ symmetry. We just have to fulfill two conditions regarding the momentum variables which vary along the FBZ. Also, from the viewpoint of topology, in the presence of the $\Theta\Gamma$ symmetry, the pseudo-vector is localized at the equatorial region

of the Bloch sphere, thus we can write

$$S_{\lambda}(k) = \lambda\hat{\varrho}(k) = \lambda\left[\cos\varphi(k), \sin\varphi(k), 0\right], \tag{1.39}$$

the azimutal angle being given by

$$\varphi(k) = \arg\left[\varrho_x(k) + i\varrho_y(k)\right]. \tag{1.40}$$

Considering the same closed contour Γ in the FBZ where the bands are gapped, thus $k \to \hat{\varrho}(k)$ we have a map from a circle S^1 to the equatorial plane of the Bloch sphere S^1. The fundamental group of this circle is non-trivial $\Pi_i(S^1) = \mathbb{Z}$, and the symmetry-protected topological invariant is the pseudo-spin winding number

.

$$w = \oint_{\Gamma} \frac{dk}{2\pi} \cdot \nabla_k \varphi(k) \quad \epsilon \quad \mathbb{Z}, \tag{1.41}$$

with $\nabla_k = \left[\partial_{k_x}, \partial_{k_y}\right]$. This number counts the number of rotations that the pseudo-spin vector does in the transverse closed path Γ in the anticlockwise direction - it does not depend on the contour and change by an integer whenever the contour is a closed loop in k-space. It is worth observing that, for a general path, the winding number cannot tell you how many Dirac points are contained on the contour. It is only possible to access the information related the total sum of topological charges associated the enclosed Dirac points.

The above figure, show us that the Dirac points correspond to vortices in the pseudo-spin field, which can be viewed as "topological defects" in the momentum space. The topological charge of the two inequivalent Dirac points K(K'), can be obtained via the calculation along small contour Γ_τ enclosing each one of the Dirac points in the **FBZ**. Using the effective Hamiltonian for each valley, we have

$$w(\tau K) = \oint_{\Gamma_\tau} \frac{d\overrightarrow{k}}{2\pi} \cdot \nabla_{\overrightarrow{k}} \arg(\tau k_x + i k_y) = \oint_{\Gamma_\tau} \frac{d\overrightarrow{k}}{2\pi} \cdot \nabla_{\overrightarrow{k}} \left[\tau\phi_k\right] = \tau. \tag{1.42}$$

We conclude that the Dirac point in the K - valley corresponds to a vortex with topological charge +1, where the pseudo-spin point in the anti-clock wise direction, while the K' valley correspond to an anti-vortice with topological charge -1, where the pseudo-spin point in the clockwise direction.

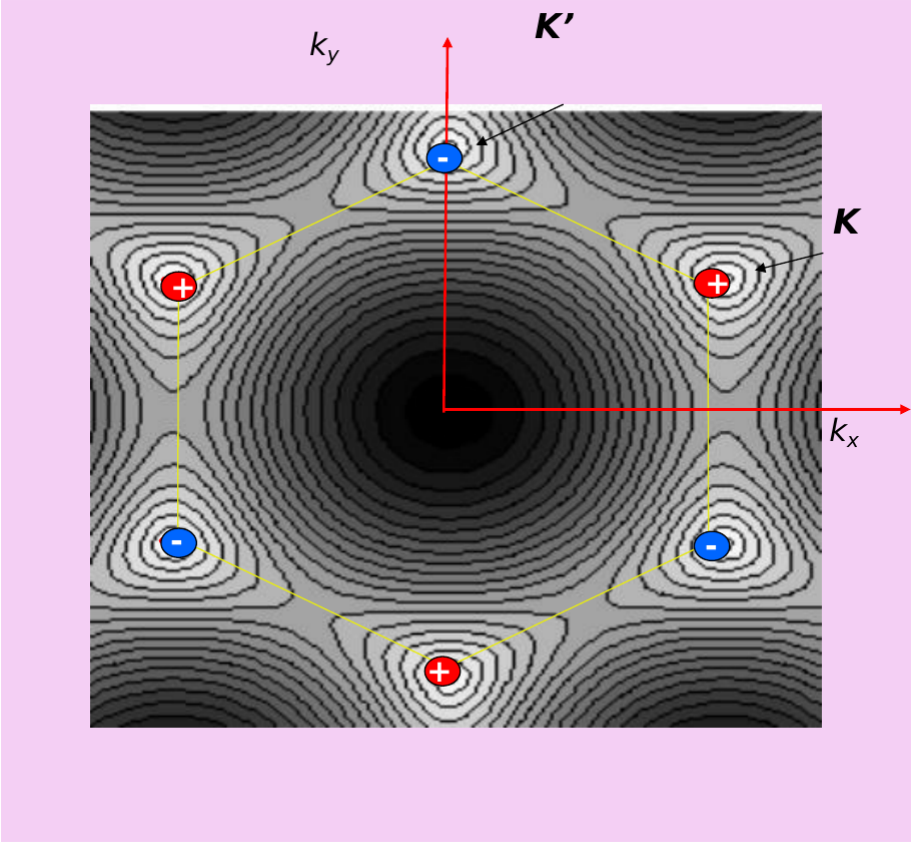

Figure 1.4.: *Topology of Dirac points. Blue negative charge and red positive charge.*

This vorticity associated to the Dirac points provides local stability in this region. Thus, under any perturbation which preserve the $\Theta\Gamma$ symmetry, it is not possible to open a gap, but it remains possible to locally shift the location of the Dirac points.

It is worth highlighting that despite the fact that the two Dirac points have opposite topological charges, they are not globally stable and the symmetry of the system can be broken when strong enough long range perturbations is applied (for instance using strain fields), leading to annihilation of the Dirac points by merging [55].

Besides, if we break the spatial or time-reversal symmetries, we can gap out the Dirac points and generate (as in the case of hexagonal boron-nitride) an insulator, with other rich topological and geometrical features.

1.2.6. Opening a gap in graphene

In the prior subsections, we discussed the role played by the time-reversal and spatial symmetries to protect topologically the graphene without SOC, which has the effective Hamiltonian presented in the Eq. (1.28), with the element of matrices: $h_{11}(k)$, $h_{12}(k)$, $h_{21}(k)$, $h_{22}(k)$. Being, with $h_{11}(k) = 0$ and $h_{22} = h_{11}(k)^*$.

In that case, graphene is gapless, $h_{11}(k) = 0$. But, when we break one of the symmetries presented which protect topologically the Dirac points, $\varrho_z(k)$ is no longer is null and arises a gap. Therefore, the term which breaks the spatial symmetry is:

$$h_{11}(k)\,\sigma_z = \pm m\sigma_z \tag{1.43}$$

which put inequivalent on-site potential on the two atoms in the primitive cell. This is precisely the situation of hexagonal boron-nitride lattice. Basically, the term that we can add to break the time-reversal symmetry is added as a next-neighbor hopping term of complex nature, such as: $t^{'}e^{i\varphi}$. This term is quite known because Haldane (see Ref. [56]) used it to start his studies in the field of topological materials.

Spin orbit interaction (SOC)

The usefulness of graphene for spintronics has early on been recognized, owing to its high electron mobility [57, 58, 59], small spin-orbit coupling (SOC) [60, 61, 62, 63] and negligible hyperfine interaction [64, 65]. All together these factors result in coherent spin propagation over unprecedented microscopic distances [66, 67, 68, 69, 70], proving graphene to be a suitable enabling material for passive spin components [71][72, 73, 74, 75, 76, 77]. Additionally, an increasing body of evidence shows that SOC in

graphene can be enhanced through interaction with a substrate or with adatoms [72, 73, 74, 75, 76, 77, 78, 79, 80, 81, 82], opening a path for the implementation of active graphene-based spintronic devices. Between these two approaches, high-SOC substrates are preferred [83, 78, 79, 80] because they are chemically inert and electrically insulating, and thus will have little impact on graphene's electronic properties. Meanwhile, weak hybridization with the substrate can enhance the SOC in the graphene layer, potentially leading to predicted phenomena such as the spin Hall effect (SHE) [84, 85] or the quantum spin Hall effect [86].

Experiments carried out over the past few years have reported strong evidence of such proximity-induced SOC enhancement in graphene when interfaced with transition metal dichalcogenides (TMDCs), and new spin device functionalities have been proposed [75, 74, 83, 78, 79, 80]. Therefore, an in-depth understanding and characterization of the properties of graphene/TMDC heterostructures appears to be fundamental for the field of spintronics. The materials used in spintronics applications can be characterized by three fundamental figures of merit: the spin relaxation time τ_s, the spin diffusion length λ_s, and the spin Hall angle γ_{sH}.

The relaxation time dictates the upper time limit within which spin information can be transmitted and manipulated, hence large τ_s is desired. The spin diffusion length denotes the distance over which spin currents can propagate without losing information, and must also be maximized. Both quantities are related by the spin diffusion coefficient D_s, which depends on the sample mobility and the transport regime, and is given in the diffusive regime by $\lambda_s = \sqrt{D_s \tau_s}$.

Finally, the spin Hall angle, which is the figure of merit of the spin Hall Effect [87], measures the efficiency of charge-to-spin conversion and vice versa. This quantity must be maximized for practical use in data storage or future non-charge-based information processing technologies. These parameters are usually evaluated through three different types of experiments: (i) measurements of Hanle precession in lateral spin valves, (ii) measurements of the weak antilocalization effect, and (iii) measurements of magnetic-field-modulated nonlocal resistance in Hall bar geometries. Each of these approaches yields some combination of τ_s, λ_s, and γ, but the obtained values can differ depending on the measurement technique. This has led to some apparent contradictions when compared to the available theoretical framework, and calls for a better understanding of these phenomena and the relationship between them in order to move forward into practical applications.

Rashba SOC

We will first present the essential aspects of spin-orbit coupling (**SOC**) properties

in graphene, including the derivation of the **SOC** from the Dirac equation, as well as the implementation of such interaction in tight-binding and continuous models.

Spin-orbit coupling in graphene

Understanding the origin and nature of **SOC** in graphene is fundamental to further study the main spin transport properties. In a nutshell, **SOC** is a relativistic effect, which can be derived from the Dirac equation, between electrons and a local electric field either due to internal or external electric fields, and which has the general form $\mathcal{H}_{so} = \frac{\mu_B}{2mc^2}\vec{E}.(\vec{\sigma} \times \vec{p})$.

Indeed fast moving electrons sense an effective magnetic field in their rest frame, which by virtue of the Zeeman effect affects their spin degree of freedom through a generic term writting $\mathcal{H}_{so} = \frac{g\mu_B}{2}\vec{B}_R.\vec{\sigma}$. The corresponding effective magnetic field $\vec{B}_R \sim \vec{E}.(\vec{p} \times \hat{z})$ (usually named a Rashba field) is parallel to the graphene plane, and induces a precession of the electron spin with a frequency (Larmor frequency) given by $\Omega = \frac{\mu_B|\vec{B}_R|}{\hbar}$.

A more complete derivation, from the relativistic Dirac Hamiltonian, is both instructive and necessary to further elaborate realistic tight-binding parameters in complex interface geometries. It starts with the definition of the Hamiltonian as [88]

$$H = \begin{pmatrix} 0 & c\mathbf{p}.\boldsymbol{\sigma} \\ c\mathbf{p}.\boldsymbol{\sigma} & 0 \end{pmatrix} + \begin{pmatrix} mc^2 & 0 \\ 0 & -mc^2 \end{pmatrix} + V. \tag{1.44}$$

The solution of the Dirac equation $H|\psi\rangle = E|\psi\rangle$ is a two-components wave function (spinor) $|\psi\rangle = (\psi_A, \psi_B)^T$ which satisfies

$$\psi_B = \frac{c\mathbf{p}.\boldsymbol{\sigma}}{E - V + mc^2}\psi_A \tag{1.45}$$

$$\mathbf{p}.\boldsymbol{\sigma}\frac{c^2}{E - V + mc^2}\mathbf{p}.\boldsymbol{\sigma}\psi_A = (E - V - mc^2)\psi_A \tag{1.46}$$

In the non-relativistic limit, ψ_B becomes negligible compared to ψ_A, since from $E = mc^2 + \epsilon$ and $V \ll mc^2$, Eq. (1.45) is rewritten as

$$\psi_B = \frac{\mathbf{p}.\boldsymbol{\sigma}}{2mc}\psi_A \ll \psi_A \tag{1.47}$$

and at the lowest order in (v/c), Eq. (1.45) reduces to the Schrödinger equation. [1]

$$\left(\frac{p^2}{2m} + V\right)\psi_A = \epsilon\psi_A \tag{1.48}$$

Here ψ_A is solution of the Schrödinger wave function ψ. At higher orders of (v/c), the normalization condition of the wave function implies

$$\int \left(\psi_A^+\psi_A + \psi_B^+\psi_B\right) = 1 \tag{1.49}$$

and by using Eq. (1.45), one founds

$$\int \psi_A^+ \left(1 + \frac{p^2}{4m^2c^2}\right)\psi_A = 1 \tag{1.50}$$

A normalized wave function is obtained when $\psi = \left(1 + \frac{p^2}{8m^2c^2}\right)\psi_A$. Substituting it into the Dirac equation, and using for $\frac{c^2}{E-V+mc^2}$ the expansion

$$\frac{1}{2m}\left(1 - \frac{\epsilon - V}{2mc^2} + ...\right), \tag{1.51}$$

one derives after some rearrangement the Pauli equation

$$\left(\frac{p^2}{2m} + V - \frac{p^4}{8m^3c^2} - \frac{\hbar}{4m^2c^2}\boldsymbol{\sigma}.\mathbf{p} \times \boldsymbol{\nabla}V + \frac{\hbar^2}{8m^2c^2}\nabla^2 V\right)\psi = \epsilon\psi, \tag{1.52}$$

where the first and second terms are usual parts of the non-relativistic Hamiltonian, while the third term denotes the relativistic correction to the kinetic energy, the fourth term is the **SOC** term and the final part is a potential-induced energy shift. The **SOC** term can be actually derived in a more intuitive manner, assuming that an electron is moving with a velocity $\mathbf{v}$ under the action of an electric field $-e\mathbf{E} = -\boldsymbol{\nabla}V$. Such electric field is generated by an external potential V stemming either from the presence of adatoms or due to the interaction and symmetry breaking induced by an underlying substrate. The electron is equivalently submitted in its rest frame to an

[1] using $(\boldsymbol{\sigma}.\boldsymbol{A})(\boldsymbol{\sigma}.\boldsymbol{B}) = \mathbf{A}.\mathbf{B} + i\boldsymbol{\sigma}.(\mathbf{A} \times \mathbf{B})$

effective magnetic field $\mathbf{B} = -\mathbf{v} \times \mathbf{E}/c$, leading to an interaction energy as

$$V_{\mu_s} = -\boldsymbol{\mu}_s \mathbf{B} = -\frac{g_s \mu_B}{2ec} \boldsymbol{\sigma}.\mathbf{v} \times \boldsymbol{\nabla} V = -\frac{g_s \hbar}{4m^2c^2} \boldsymbol{\sigma}.\mathbf{p} \times \boldsymbol{\nabla} V = -\frac{\hbar}{2m^2c^2} \boldsymbol{\sigma}.\mathbf{p} \times \boldsymbol{\nabla} V \tag{1.53}$$

This result turns out to double the **SOC** term appearing in the Pauli equation, a difference explained by Thomas [89]. Fundamentally, the electron moves in a rotating frame of reference, which leads to its spin precession under the action of

$$\mathbf{B} = -\frac{\mathbf{v} \times \mathbf{E}}{2c} \tag{1.54}$$

which yields the full **SOC** term

$$V_{SOC} = -\frac{\hbar}{4m^2c^2} \boldsymbol{\sigma}.\mathbf{p} \times \boldsymbol{\nabla} V \tag{1.55}$$

where j is the nearest-neighbor of i and γ_1 and V_R are material and interface-dependent parameters. The full **SOC-TB** Hamiltonian finally reads :

$$\mathcal{H}_{SOC} = -\gamma_0 \sum_{\langle ij \rangle} c_i^+ c_j + \frac{2i}{\sqrt{3}} V_I \sum_{\langle\langle ij \rangle\rangle} c_i^+ \mathbf{s}.(\hat{\mathbf{d}}_{kj} \times \hat{\mathbf{d}}_{ik}) c_j + i V_R \sum_{\langle ij \rangle} c_i^+ \hat{\mathbf{z}}.(\mathbf{s} \times \hat{\mathbf{d}}_{ij}) c_j \tag{1.56}$$

Close to the Dirac point, a low energy Hamitonian approximation $h(\mathbf{k})$ can be easily derived in the basis $\{|A\rangle, |B\rangle\} \otimes \{|\uparrow\rangle, |\downarrow\rangle\}$, with

$$h(\mathbf{k}) = h_0(\mathbf{k}) + h_R(\mathbf{k}) + h_I(\mathbf{k}) \tag{1.57}$$

and where

$$\begin{aligned} h_0(\mathbf{k}) &= \hbar v_F (\eta \sigma_x k_x + \sigma_y k_y) \otimes 1_s \\ h_R(\mathbf{k}) &= \lambda_R \left(\eta \left[\sigma_x \otimes s_y\right] - \left[\sigma_y \otimes s_x\right]\right) \\ h_I(\mathbf{k}) &= \lambda_I \eta \left[\sigma_z \otimes s_z\right] \end{aligned} \tag{1.58}$$

with Fermi velocity $v_F = \frac{3}{2}\gamma_0$, Rashba **SOC** $\lambda_R = \frac{3}{2} V_R$ and intrinsic SOC $\lambda_I = 3\sqrt{3} V_I$ [90], all **SOC** terms being momentum-independent. The spin directly couples with the pseudospin instead of momentum as in conventional metals or semiconductors,

while the usual SOC term ($\mathbf{k} \times \mathbf{s}$) is small and usually neglected. By diagonalizing the Hamiltonian given in Eq. (1.57), the low-energy electronic bands are derived [62, 91]:

$$\epsilon_{\mu\nu}(\mathbf{k}) = \mu\lambda_R + \nu\sqrt{(\hbar v_F k)^2 + (\lambda_R - \lambda_I)^2} \tag{1.59}$$

where μ and $\nu = \pm 1$ are band indexes. In absence of Rashba-SOC, the electronic system is gapped with $\Delta = 2\lambda_I$ (See Fig. 1.5(c) left panel). In presence of a Rashba **SOC**, the competition between Rashba and intrinsic **SOC** determines the existence or not of a finite Δ value. The gap remains finite $\Delta = 2(\lambda_I - \lambda_R)$ for $0 < \lambda_R < \lambda_I$ (Fig. 1.5(c)), whereas it closes when $\lambda_R > \lambda_I$, and the electronic structure then becomes a zero gap semiconductor with quadratically dispersing bands (Fig. 1.5(c) right panel). The spin branch $\mu = 1$ is shown in solid and $\mu = -1$ in dashed, corresponding to the different Dirac cones in (a). Fermi velocity is $v_F = 0.833 \times 10^6$ m/s (Fermi level is at zero). The analytical form of the eigenfunctions writes

$$\psi_{\mu\nu}(\mathbf{k}) = \left(\chi_-|\eta e^{-i\eta\varphi}\left[\frac{\epsilon_{\mu\nu} - \lambda_I}{\nu\hbar v_F k}\right]^\eta, 1\rangle + \mu\chi_+|-i\eta e^{-i(1+\eta)\varphi}, ie^{-i\varphi}\left[\frac{\lambda_I - \epsilon_{\mu\nu}}{\nu\hbar v_F k}\right]^\eta\rangle\right)/C_{\mu\nu}$$

with $\tan\varphi = k_y/k_x$ and the normalization constant $C_{\mu\nu} = \sqrt{2}\left(1 + \left[\frac{\lambda_I - \epsilon_{\mu\nu}}{\hbar v_F k}\right]^{2\eta}\right)^2$. The expectation value of the spin polarization of electronic states is further derived as [62, 91],

$$\mathbf{s}_{\mu\nu}(\mathbf{k}) = \frac{\hbar v_F(\mathbf{k} \times \hat{\mathbf{z}})}{\sqrt{(\hbar v_F k)^2 + (\lambda_I - \mu\lambda_R)^2}} = \frac{\hbar v_F k}{\sqrt{(\hbar v_F k)^2 + (\lambda_I - \mu\lambda_R)^2}}\mathbf{n}(\mathbf{k}) \tag{1.60}$$

where $\mathbf{n}(\mathbf{k}) = (\sin\varphi, -\cos\varphi, 0)$ is the unit vector along the spin direction, called spin vector. As seen from Eq. (1.60), the remarkable characteristic of the spin polarization is that it remains in-plane and perpendicular to the electron momentum $\mathbf{k}$, while its magnitude vanishes when $k \to 0$.

As a result near the Dirac point, the spin and the pseudospin are strongly coupled, a fact which generates strong entanglement between the spin and pseudopsin dynamics and gives rise to an hitherto unknown source for spin relaxation, especially dominating in the ultra clean graphene limit (see Sect. 1.2.8 and [35, 92, 37]).

Importantly, one notes that at high energies $\hbar v_F k \gg \lambda_R + \lambda_I$, the pseudospin becomes fully controlled by the momentum dynamics via $h_0(\mathbf{k})$ and thus aligns in

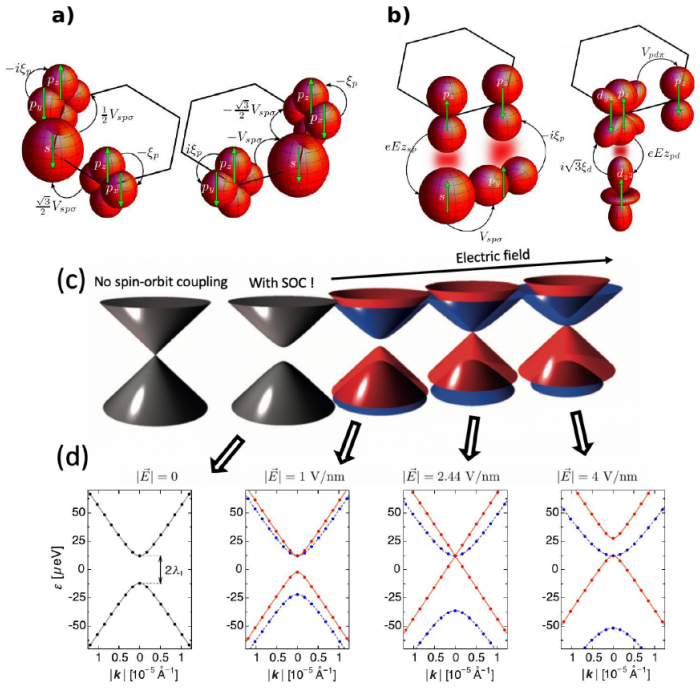

Figure 1.5.: *(a): Two of the possible nnn hopping paths through the s, p orbitals. (b): A representative leading hopping path, arrows, which is responsible for the Rashba SOC effect, by coupling states of different spins. (c) Band structures of graphene with SOC in a external transverse electric field. Touching Dirac cones exist only when spin–orbit coupling is neglected (first from left). When SOC is switched on, the orbital degeneracy at the Dirac point is lifted and the spin–orbit gap appears (second from left). In an external electric field perpendicular to graphene, due to a gate or a substrate, the Rashba effect lifts the remaining spin degeneracy of the bands (third, fourth and fifth from left). If the intrinsic and Rashba couplings are equal, at a certain value of the electric field, two bands form touching Dirac cones again (fourth from left). If the Rashba coupling dominates (fifth from left), the spin–orbit gap closes. (d) Ab initio band structures of graphene are represented by circles and fitted with an analytical model. ((a) and (b) are reproduced with permission from [63]. Copyright (2010) by the American Physical Society. (c) is reproduced by permission from Macmillan Publishers Ltd: Nature Nanotechnology [65], copyright (2014). (d) is reproduced with permission from [62]. Copyright (2009) by the American Physical Society.*

the same direction (in plane). The spin dynamics is then dictated by its coupling with pseudospin via $h_R(\mathbf{k})$, which leads to a saturation (to 1) of the spin polarization for a certain momentum in Eq. (1.60).

By successive unitary rotations of $h(\mathbf{k})$ first into the eigenbasis of $h_0(\mathbf{k})$ and then into the spin basis with respect to the direction $\mathbf{n}(\mathbf{k})$, an effective Bychkov-Rashba-type 2×2 Hamiltonian is obtained for both holes and electrons [93],

$$\tilde{h}(\mathbf{k}) = \nu(\hbar v_F k - \lambda_I) - \nu\lambda_R \mathbf{n}(\mathbf{k}).\mathbf{s} \tag{1.61}$$

The second term in Eq.(1.61) ressembles the Bychkov-Rashba Hamiltonian in semiconductor heterostructures $H_{\mathbf{k}} = \hbar\mathbf{\Omega}(\mathbf{k}).\mathbf{s}/2$, evidencing that the SOC also acts on the electrons spin as an in-plane magnetic field, of constant amplitude but perpendicular to $\mathbf{k}$. In this effective magnetic field the spin precesses with a frequency and a period of [93]

$$\Omega = \frac{2\lambda_R}{\hbar}, \qquad T_\Omega = \frac{\pi\hbar}{\lambda_R} \tag{1.62}$$

All such results have been confirmed quantitatively by numerical simulations using real-space order N method implemented for spin dynamics [35, 36, 37] .

1.2.7. Theoretical estimation of the SOC terms magnitude

SOC in graphene is clearly expected to be weak owing to the low atomic number of carbon ($Z = 6$, while spin-orbit interaction scales as Z^4). Moreover, the natural occurrence of zero nuclear spin isotope C^{12} is close to 99% and makes hyperfine interaction a vanishingly small decoherence mechanism. The precise magnitude of **SOC** is actually a highly complicate question, but concurrently a critical information to determine the spin lifetime and the dominant spin relaxation mechanism.

A theoretical estimate for intrinsic **SOC** $\lambda_I \sim 100\mu eV$ has been first proposed by Kane and Mele [86]. This value was reduced by Min *et al.* [94] to $0.5\mu eV$ by using microscopic **TB** model and second-order perturbation theory, a result later supported by Huertas-Hernando *et al.* [61] with a **TB** model and by Yao *et al.* [95] using first-principles calculations.

Another **DFT** calculation of Boettger and Trickey [96], using a Gaussian-type orbital fitting function methodology finally provided $25\mu eV$. The studies published in Ref. [61, 95, 94] gave similarly small values for λ_I, but these calculations only involved the **SOC** induced by the coupling between p_z (forming the π bands) and s orbitals (forming the σ band) orbitals. However, as pointed out in Ref. [63], the

coupling of the p_z orbitals to the d orbitals (See Fig. 1.5 (a) and (b)) dictates the spin orbit effects near the $K(K')$-points.

Indeed, owing to a finite overlap between the neighboring p_z and d_{xz}, d_{yz} orbitals, the intrinsic splitting λ_I is linearly proportional to the spin-orbit splitting of the d states, ξ_d (orbitals higher than d have a smaller overlap and contribute less). Differently, due to the absence of the direct overlap between the p_z and σ-band orbitals, the spin-orbit splitting induced by the $\sigma - \pi$ mixing depends only quadratically on the spin-orbit splitting of the p_z orbital, ξ_p, yielding a negligible contribution [61, 95, 94] (Fig. 1.5(a)).

$$\lambda_I \simeq \frac{2(\varepsilon_p - \varepsilon_s)}{9V_{sp\sigma}^2}\xi_p^2 + \frac{9V_{pd\pi}^2}{2(\varepsilon_d - \varepsilon_p)^2}\xi_d, \tag{1.63}$$

where $\varepsilon_{s,p,d}$ are the energies of s, p, d orbitals, respectively and $V_{sp\sigma}$ and $V_{pd\pi}$ are hopping parameters of the p orbital to the s and d orbital, respectively. This **TB** calculation leads to an intrinsic SOC of $\lambda_I = 12\mu eV$ [63], agreeing with **DFT** simulations [62]. Such results also suggest that the Rashba term (absent for zero electric field) is tunable with an external electric field E (which is perpendicular to graphene plane)

$$\lambda_R \simeq \frac{2eEz_{sp}}{3V_{sp\sigma}}\xi_p + \sqrt{3}\frac{eEz_{sp}}{(\varepsilon_d - \varepsilon_p)}\frac{3V_{pd\pi}}{(\varepsilon_d - \varepsilon_p)}\xi_d, \tag{1.64}$$

where z_{sp} and z_{pd} are the expectation values $\langle s|\hat{z}|p_z\rangle$ and $\langle p_z|\hat{z}|d_{z^2}\rangle$, respectively, of the operator $\hat{z}$ (Fig.1.5(b)). All these calculations predicted that the Rashba **SOC** is directly proportional to the electric field E, but the estimated values vary by about one order of magnitude from $5\mu eV$ in Ref. [62] to $40 - 50\mu eV$ in Ref. [61, 97] and to $67\mu eV$ in Ref. [94], for a typical electric field of $E = 1\text{V/nm}$.

Four-band model for graphene

For further studying intra-particle entanglement, the most convenient starting model is the total Hamiltonian in the continuous approximation. The graphene with Rashba **SOC** Hamiltonian in the continuous model that is equivalent to the full tight-binding version presented previously, is given by (assuming the **K** valley):

$$\begin{aligned} H = {} & \hbar\upsilon_F\left(\sigma_x k_x + \sigma_y k_y\right) \otimes 1_s + \lambda_R\left(\sigma_x \otimes s_y - \sigma_y \otimes s_x\right) + \\ & + \tfrac{\lambda_R a_{cc}}{2}\left[k_x\left(\sigma_x \otimes s_y + \sigma_y \otimes s_x\right) + k_y\left(\sigma_x \otimes s_x + \sigma_y \otimes s_y\right)\right]. \end{aligned} \tag{1.65}$$

The second-order term Rashba **SOC** just promotes a simple dephasing regarding the curve of concurrence for each direction k_x, k_y at very high-energy, similar to what happens with the anisotropic spin- lifetime in high-energy. The kronecker products of the spin and pseudospin Pauli matrices are:

$$\sigma_x \otimes 1_s = \begin{pmatrix} 0 & 1 \\ 1 & 0 \end{pmatrix} \otimes \begin{pmatrix} 1 & 0 \\ 0 & 1 \end{pmatrix} = \begin{pmatrix} 0 & 0 & 1 & 0 \\ 0 & 0 & 0 & 1 \\ 1 & 0 & 0 & 0 \\ 0 & 1 & 0 & 0 \end{pmatrix} \overset{2\Leftrightarrow 3}{\rightarrow} \begin{pmatrix} 0 & 1 & 0 & 0 \\ 1 & 0 & 0 & 0 \\ 0 & 0 & 0 & 1 \\ 0 & 0 & 1 & 0 \end{pmatrix}. \quad (1.66)$$

$$\sigma_y \otimes 1_s = \begin{pmatrix} 0 & -i \\ i & 0 \end{pmatrix} \otimes \begin{pmatrix} 1 & 0 \\ 0 & 1 \end{pmatrix} = \begin{pmatrix} 0 & 0 & -i & 0 \\ 0 & 0 & 0 & -i \\ i & 0 & 0 & 0 \\ 0 & i & 0 & 0 \end{pmatrix} \overset{2\Leftrightarrow 3}{\rightarrow} \begin{pmatrix} 0 & -i & 0 & 0 \\ i & 0 & 0 & 0 \\ 0 & 0 & 0 & -i \\ 0 & 0 & i & 0 \end{pmatrix}. \quad (1.67)$$

$$\sigma_x \otimes s_y = \begin{pmatrix} 0 & 1 \\ 1 & 0 \end{pmatrix} \otimes \begin{pmatrix} 0 & -i \\ i & 0 \end{pmatrix} = \begin{pmatrix} 0 & 0 & 0 & -i \\ 0 & 0 & i & 0 \\ 0 & -i & 0 & 0 \\ i & 0 & 0 & 0 \end{pmatrix} \overset{2\Leftrightarrow 3}{\rightarrow} \begin{pmatrix} 0 & 0 & 0 & -i \\ 0 & 0 & -i & 0 \\ 0 & i & 0 & 0 \\ i & 0 & 0 & 0 \end{pmatrix}. \quad (1.68)$$

$$\sigma_y \otimes s_x = \begin{pmatrix} 0 & -i \\ i & 0 \end{pmatrix} \otimes \begin{pmatrix} 0 & 1 \\ 1 & 0 \end{pmatrix} = \begin{pmatrix} 0 & 0 & 0 & -i \\ 0 & 0 & -i & 0 \\ 0 & i & 0 & 0 \\ i & 0 & 0 & 0 \end{pmatrix} \overset{2\Leftrightarrow 3}{\rightarrow} \begin{pmatrix} 0 & 0 & 0 & -i \\ 0 & 0 & i & 0 \\ 0 & -i & 0 & 0 \\ i & 0 & 0 & 0 \end{pmatrix}. \quad (1.69)$$

We did some permutations regarding the second and third rows in each kronecker products in ordering of obtaining a Hamiltonian in the spin-pseudospin basis.

Therefore, the higher-order Rashba continuous Hamiltonian is gives by

$$\hat{H} = \begin{pmatrix} 0 & \epsilon_0 e^{-i\theta} & 0 & 0 \\ \epsilon_0 e^{i\theta} & 0 & -2i\lambda_R & 0 \\ 0 & 2i\lambda_R & 0 & \epsilon_0 e^{-i\theta} \\ 0 & 0 & \epsilon_0 e^{i\theta} & 0 \end{pmatrix} \tag{1.70}$$

where $\epsilon_0 = \hbar\nu_F \mathbf{k}$ and $\theta = tan^{-1}(k_y/k_x)$. The representation of the relevant bipartite degree of freedom can be described as

- Spin:

$$s_x = \begin{pmatrix} 0 & 1 \\ 1 & 0 \end{pmatrix}, \qquad s_y = \begin{pmatrix} 0 & -i \\ i & 0 \end{pmatrix}, \qquad s_z = \begin{pmatrix} 1 & 0 \\ 0 & -1 \end{pmatrix} \tag{1.71}$$

- Pseudospin:

$$\sigma_x = \begin{pmatrix} 0 & 1 \\ 1 & 0 \end{pmatrix}, \qquad \sigma_y = \begin{pmatrix} 0 & -i \\ i & 0 \end{pmatrix}, \qquad \sigma_z = \begin{pmatrix} 1 & 0 \\ 0 & -1 \end{pmatrix} \tag{1.72}$$

1.2.8. Spin-pseudopsin entanglement and spin relaxation

Pseudospin-related effects (and the associated Berry phase) are known to drive most of the unique transport signatures of graphene (Klein tunneling, weak antilocalization, anomalous quantum Hall effect), but the role of such extra degree of freedom on spin relaxation has been discovered only recently. Pseudospin and spin dynamics are usually perceived as decoupled from one another, with pseudospin dynamics much faster when compared to spin rotation.

However, this picture collapses in the vicinity of the Dirac point, a region that is out of reach for semi-classical and perturbative approaches, but is particularly relevant for experiments. In the presence of **SOC**, spin couples to orbital motion, and therefore to pseudospin [98], so that spin and pseudospin dynamics cannot be treated independently.

Here we present the main ideas underpinning a new relaxation mechanism and driven by a spin-pseudospin entanglement effect. To capture the unusual behavior of the spin lifetime at low energies, it is first instructive to investigate the Kane-Mele-Rashba (**KMR**) Hamiltonian in the vicinity of both valleys K and K'. At low energy (when $|\vec{k}| \to 0$) the term which couples pseudospin and momentum ($h_0(\vec{k})$)

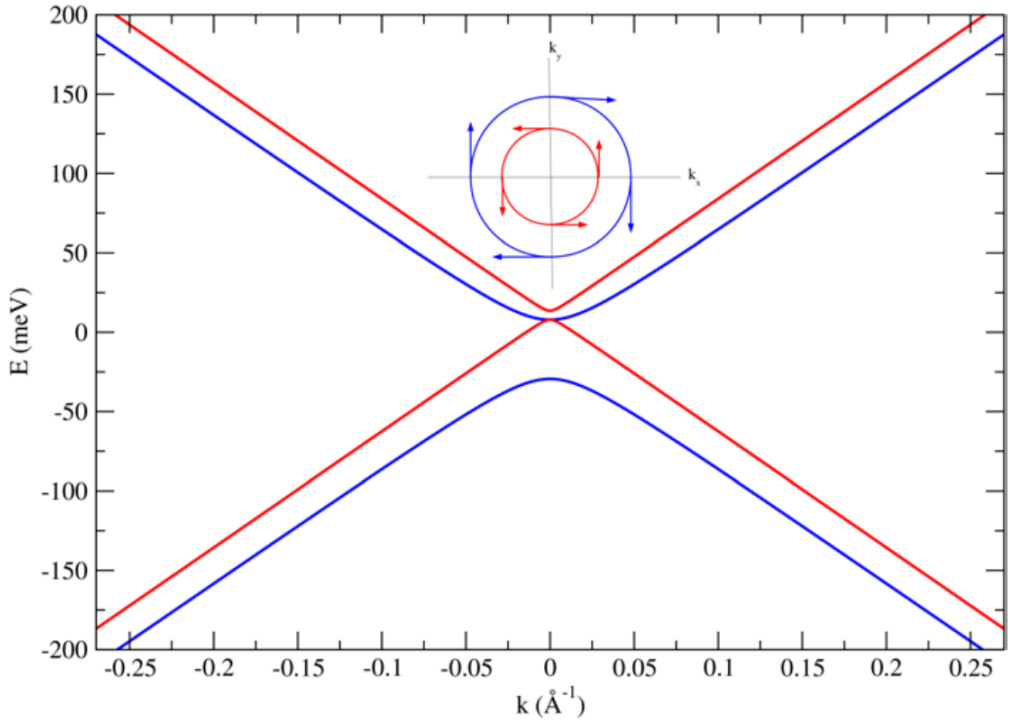

Figure 1.6.: *Band structure calculated using the Kane-Mele-Rashba model for 8% adatom concentration generating an overall Rashba* ***SOC****. The inset shows the typical Rashba-like spin texture for the conduction bands. (Reprinted by permission from Macmillan Publishers Ltd: Nature Physics [35], copyright (2014).)*

vanishes, in contrast to the Rashba term ($h_R(\vec{k})$) which connects spin and pseudospin. Hence close to the Dirac point, the term $h_R(\vec{k})$ dictates the spin and pseudospin precession motion and leads to a spin-pseudospin locking feature.

On the contrary, for high energies ($|\vec{k}| > 0$) the term $h_0(\vec{k})$ exceeds the Rashba term and disrupts the locking effect. Fig.1.6 gives the computed band structure of the Kane-Mele-Rashba Hamiltonian assuming 8% impurity coverage [35]. The Rashba term generates a counter-propagating spin texture in the k_x, k_y plane that tends to vanish close to the Dirac point as [98]:

$$\vec{S}_{\nu\mu}(\vec{k}) = \frac{\mu\hbar v_F(\vec{k} \times \vec{z})}{\sqrt{\lambda_R^2 + \hbar^2 v_F^2 k^2}} \tag{1.73}$$

We further calculate the modulus of the spin polarization vector $|\vec{S}| = |(\langle s_x \rangle, \langle s_y \rangle, \langle s_z \rangle)|$ from the eigenstates of the full Hamiltonian in Eq.(1.57) with both intrinsic and

Rashba **SOC**

$$\Psi_{\vec{k},\pm} = \left[\begin{pmatrix} c_{A,\uparrow} \\ c_{B,\uparrow} \end{pmatrix} \otimes |\uparrow\rangle \pm i \begin{pmatrix} c_{A,\downarrow} \\ c_{B,\downarrow} \end{pmatrix} \otimes |\downarrow\rangle \right] \mathrm{e}^{i\vec{k}\vec{r}}, \tag{1.74}$$

where, in presence of the Rashba SOC term, the Bloch states with well-defined spin polarization are no longer eigenstates of the complete Hamiltonian [99]. The clear signature of spin-pseudospin entanglement is actually evidenced at low energies ($\vec{k} \to 0$) since the electronic states write

$$\Psi^{I}_{\vec{k},\pm} = \begin{pmatrix} 0 \\ 1 \end{pmatrix} \otimes |\uparrow\rangle \pm \begin{pmatrix} i \\ 0 \end{pmatrix} \otimes |\downarrow\rangle \tag{1.75}$$

$$\Psi^{II}_{\vec{k},\pm} = \begin{pmatrix} 1 \\ 0 \end{pmatrix} \otimes |\uparrow\rangle \pm \begin{pmatrix} 0 \\ i \end{pmatrix} \otimes |\downarrow\rangle. \tag{1.76}$$

In both cases, a change in sublattice (pseudospin) index entails a change in spin index. This means that at low energy spin and pseudospin are completely locked and $|\vec{S}| \approx 0$. The situation is different for high energies ($|\vec{k}| > 0$), when pseudospin-momentum coupling comes into play, all coefficients become equally weighted ($|c_{\sigma,s}| \approx 0.5$) and spin and pseudospin are unlocked leading to $|\vec{S}| \approx 1$.

It is also instructive to explore the spin propagation in graphene using more general quantum dynamics methods, and taking into account the specificity of the graphene band structure in the presence of **SOC** and disorder (energy broadening and electron-hole puddles).

Studies have been realized using an exact calculation of spin dynamics through time dependent evolution methods [35, 92, 37, 88]. The advantage of such approaches is to capture the effect of both disorder of any kind and strong SOC regimes, beyond the reach of perturbation theory.

Concerning the nature of disorder in (clean) exfoliated graphene samples, it is known that the strength and size of electron-hole puddles can vary significantly for different substrates (such as SiO_2 or hBN), and in the situation of clean supported graphene it is generally assumed that a weak Rashba-**SOC** field is always present because of mirror symmetry breaking and surrounding electric fields.

When the disorder is strong enough to yield $\tau_p \ll T_\Omega$ (case of electron-hole puddles for graphene/SiO_2), then the numerical simulations [92] confirm a scaling for the spin lifetime as $\tau_s \sim 1/n_i$ where n_i is the puddle density, and a ratio $\tau_s^{\perp}/\tau_s^{\parallel} = 1/2$ in

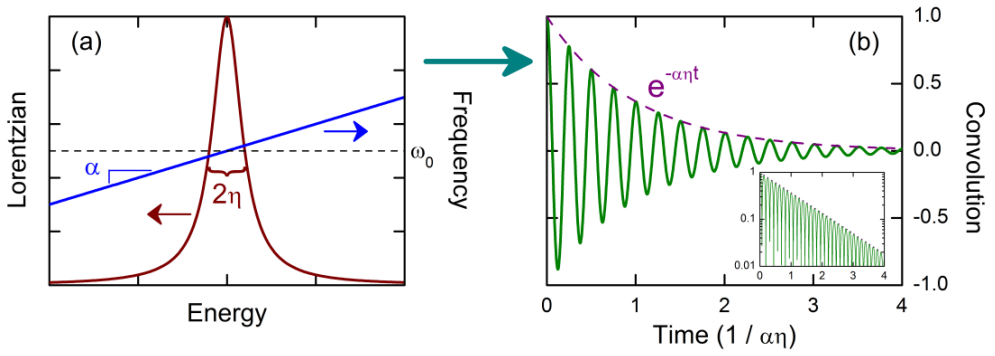

Figure 1.7.: *(a) Convolution of the spin precession frequency (right axis) with a Lorentzian energy broadening (left axis). The η parameter gives the HWHM of the Lorentzian, while α denotes the variation of the spin precession frequency. (b) Exponentially decaying cosine, with frequency ω_0 and decay time $1/\alpha\eta$. By courtesy of A.W. Cummings, reproduced from [100].*

full agreement with the conditions required for the **DP** regime [101] (see also Fig. 1.8).

However, for cleaner graphene samples and flat substrates (e.g. electron-hole puddles for hBN) the regime $\tau_p \gg T_\Omega$ can be eventually reached; a regime where **DP** regime ceases to apply, as well as the conventional **EY** regime. In such a (quasi)-ballistic transport regime in graphene, τ_p is no longer a relevant timescale for understanding spin relaxation.

It has been actually found that in this limit, the spin relaxation is dictated by the presence of energy broadening and, more importantly a *non-uniform precession frequency*, a fundamental ingredient which has been neglected in prior studies [93].

The presence of **SOC** generates the effective magnetic field B_{eff} which monitors the spin rotation. When the magnitude of B_{eff} (or its direction) depends on the electron energy (or momentum) distribution (defined by temperature or effective disorder-induced broadening), then the total spin signal derives from interference and dephasing between different precession frequencies.

As a matter of illustration, let us focus on the case illustrated in Fig.1.7, where the spin precession frequency varies linearly with $\omega(E) = \omega_0 + \alpha E$, while the energy occupation for electrons is given by a Lorentzian distribution $L(E) = \eta/[\pi(E^2 + \eta^2)]$ (η as the half-width at half-maximum (**HWHM**)). From simple considerations, the

total spin signal $s(t)$ is obtained from [37]

$$L(E)\cos(\omega(E)t) = \int_{-\infty}^{+\infty} (\eta/\pi)/(E^2+\eta^2)\cos((\alpha E+\omega_0)t)dE, \tag{1.77}$$

$$= e^{-\alpha\eta t}\cos(\omega_0 t). \tag{1.78}$$

Eq. (1.77) indicates that the combination of energy broadening and nonuniform spin precession leads to a dephasing of the spin signal which is eventually lost at a rate proportional to both the broadening η and the precession variation. This decay (not necessarily exponential) occurs even in the ballistic regime provided the existence of a frequency mixing in energy or momentum.

Indeed, when replacing the Lorentzian with a Gaussian distribution, Eq.(1.77) gives $e^{-(\alpha\sigma t)^2/2}$, with σ the standard deviation, whereas a Fermi distribution produces $\Xi t/\sinh(\Xi t)$ ($\Xi = \alpha\pi kT$ and kT is the thermal energy) [37].

In conclusion if **DP** dominates for dirty graphene with low mobility, in the limit of clean (and even ballistic) limit, a new spin dephasing mechanism, driven by strong coupling between spin and pseudospin, gives rise to an intricated mixing of precession frequencies which dictate the energy variation of the spin lifetime, as well as its upper value [35, 92, 37].

Actually, the approximation of an energy-independent spin precession frequency made in Ref. [93] was demonstrated to be the origin of the astonishing discrepancy of such earlier calculations compared with experimental data [37].

To get the full picture, Fig. 1.8 shows the $\tau_s(1/\tau_p)$ for both numerical and experimental data taken from [67]. In the main frame the simulation for the SiO_2 substrate, the scaling matches well with the **DP** relation, $\tau_s = (T_\Omega/2\pi)^2/\tau_p$, where $T_\Omega = 2\pi\hbar/(3V_R)$, whereas for the hBN substrate the opposite scaling trend is seen, with τ_s proportional to τ_p, reminiscent of the EY mechanism.

The crossover is related to the ratio τ_p/T_Ω. For SiO_2, one clearly obtains a regime where $\tau_p \ll T_\Omega$ meaning that momentum scattering frequently interrupts the spin dynamics, inducing motional narrowing of the precession as described in the **DP** relaxation mechanism.

Differently, for the hBN substrate, numerical simulations show that $\tau_p \geq T_\Omega$, allowing for spin precession between scattering events. In this case, the momentum scattering acts as an effective broadening of states, leading to increased dephasing and relaxation.

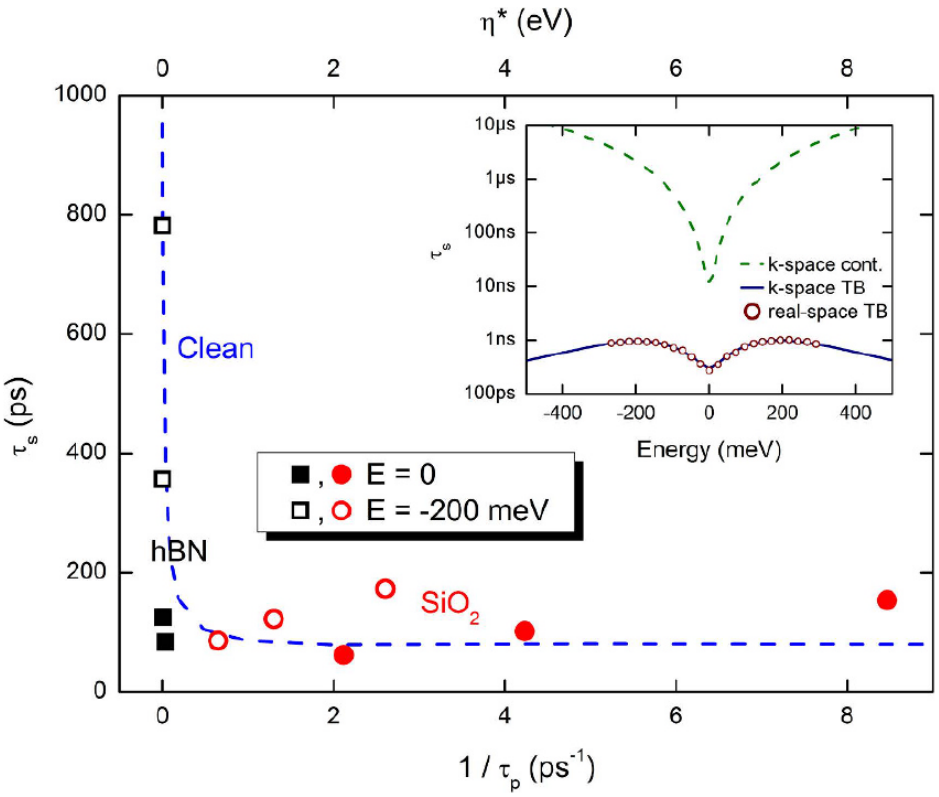

Figure 1.8.: *Spin lifetime vs.* $1/\tau_p$ *for graphene in the presence of SOC and e-h puddles. Squares (circles) are for graphene on hBN* (SiO_2) *substrate. Closed (open) symbols are for spin relaxation at the Dirac point (at* $E = -200$ *meV). The blue dashed line shows the spin lifetime assuming only energy broadening (top axis). Inset: experimental results for spin lifetime vs. electron mobility on hBN and* SiO_2 *substrates.(The main panel is reprinted from [92]. The inset is Reprinted with permission from ([67]). Copyright (2014) American Chemical Society.)*

This behaviour can be qualitatively reproduced by tuning the broadening parameter in the case of clean graphene (blue dashed line). Similar trends have been obtained in experiments that compare spin relaxation on SiO_2 and hBN substrates [67].

As shown in the inset of Fig. 1.8, these measurements indicate an inverse relationship between τ_s and the sample mobility for SiO_2 substrates in agreement with **DP** [101].

Meanwhile, spin lifetimes of single-layer graphene on hBN substrates appear to show a positive correlation between τ_s and the mobility, therefore supported with the new theoretical picture.

1.2.9. Graphene/TMDC's heterostructures.

1.2.9.1. Enhancement of SOC in graphene

Additionally, we give an overview of the most relevant evidence of spin-orbit coupling enhancement in graphene and how it was determined. Both of these discussions will serve as a baseline for understanding our motivation to try to explore how eletronic properties in these systems are connected with intraparticle bipartite entanglement which we have studied in the previous section.

Recently, a three-order-of-magnitude enhancement of SOC was reported in weakly hydrogenated graphene [72]. Subsequently, a large number of experiments have also reported evidence of **SOC** enhancement in graphene, opening a new era for graphene-based spintronics [102, 72, 73, 74, 75, 78, 103, 83, 80, 79, 104, 105, 106].

The presence of spin-orbit coupling in a material can be detected by measuring weak antilocalization or the spin Hall effect, as in general these phenomena will not exist without **SOC**. In this regard, graphene is a special case because there can be weak antilocalizaton due to the presence of pseudospin [107]. However, this happens under very special experimental conditions which are not the general situation.

The first experimental measurements were focused on detecting the spin Hall effect through measurements of nonlocal resistance in a Hall bar geometry. Such measurements indeed found large nonlocal signals, and these were attributed to enhancement of the **SOC** in graphene by adatoms [72, 73, 74]. However, using this approach can be complicated given that a variety of phenomena unrelated to spin may also lead to large nonlocal signals [108, 81, 82, 109, 110].In graphene/TMDC heterostructures, the initial measurements were centered on detecting weak antilocalization, which is then fitted to WAL theory [111] to obtain the corresponding spin relaxation rates. Following this approach, a variety of groups have confirmed the undeniable presence of proximity-induced **SOC** [112, 75, 78, 83, 103, 80, 102, 106].

SOC parameters can be indirectly evaluated from WAL measurements by connecting spin-orbit relaxation rates to spin relaxation mechanisms. However, all but the most recent analyses have ignored the impact of valley-Zeeman **SOC**, despite simulations based on density functional theory (**DFT**) showing it to be the dominant term [112, 113, 103, 114].

Finally, it was recently proposed that a giant spin lifetime anisotropy is a signature of proximity-induced SOC in graphene/TMDC heterostructures [115]. This effect was subsequently confirmed by two independent groups using variations of the Hanle precession measurement [104, 105].

These measurements make it clear that TMDCs induce a strong **SOC** in graphene, and that the nature of this **SOC** leads to unusual features in the spin transport. In the following section we provide the theoretical framework to understand the nature of spin transport in these systems.

1.2.9.2. Tight-binding model for graphene/TMDC's

To capture the main features of the *ab initio* calculations, a tight-binding (**TB**) model was developed using group theory by Gmitra and coworkers [113, 116]. Thus, here we will follow up on these seminal works and focus on the effective hamiltonian for spin and pseudospin degree of freedom only, for a given **K(K')**. We consider the tight-binding Hamiltonian of graphene on a TMDC, with all orders of Rashba, intrinsic and **PIA SOC**, such as

$$\begin{aligned} H = t \sum_{\langle\langle i,j\rangle\rangle} c_{i\sigma}^{\dagger} c_{j\sigma} + \Delta \sum_{i} \xi_{ci} c_{i\sigma}^{\dagger} c_{i\sigma} + \tfrac{2i}{3} \lambda_R \sum_{\langle i,j\rangle} c_{i\sigma}^{\dagger} c_{j\sigma'} \left[(\vec{s} \times d_{ij})_z \right]_{\sigma\sigma'} + \\ + \tfrac{i}{3} \sum_{\langle\langle i,j\rangle\rangle} c_{i\sigma}^{\dagger} c_{j\sigma'} \left[\tfrac{\lambda_I^{c_i}}{\sqrt{3}} \nu_{ij} s_z + 2\lambda_{PIA}^{c_i} (\vec{s} \times D_{ij})_z \right]_{\sigma\sigma'}, \end{aligned} \tag{1.79}$$

where $c_{i\sigma}^{\dagger} = \left(a_{i\sigma}^{\dagger}, b_{i\sigma}^{\dagger}, \right)$ and $c_{i\sigma} = (a_{i\sigma}, b_{i\sigma},)$, describe the creation and annihilation operators for an electron on a lattice site i that belongs to the sublattice A or B, respectively, and hosts spin σ. The two first terms in Eq. (1.79) are responsible for governing the dynamics of these systems on the orbital scale, where the nearest-neighbor hopping (sum over $\langle i,j\rangle$) is parametrized by a hybridization t, and the staggered on-site potential Δ is an effective energy difference experienced by the sublattices **A** ($\xi_{ai} = 1$) and **B** ($\xi_{bi} = -1$) .

The other three terms of the above equation represent the spin-orbit coupling (**SOC**) regarding the nearest (sum over $\langle i,j\rangle$) and next-nearest (sum $\langle\langle i,j\rangle\rangle$) neighbor hoppings. Between the **SOC** terms, the first one is regarding the Rashba **SOC** with its parameter given by λ_R . It arises when the monolayer graphene is placed on top

of any XY_2 TMDC. The last two terms of the above equation are the next-neighbor terms that arises from sublattice (pseudospin) symmetry breaking. Pseudospin inversion asymmetry (**PIA**) induced term parametrized by $\lambda_{PIA}^{c_i} = \lambda_{PIA}^{A}\left(\lambda_{PIA}^{B}\right)$, being c_i the sublattice **A(B)**. also arises from sublattice (pseudospin) symmetry breaking mechanism.

In Eq. (1.79), $\hat{s}$ is a vector of Pauli matrices acting on the spin subspace and the spin factor $\nu_{ij} = 1\,(-1)$ means the clockwise (counterclockwise) hopping path from the site j to i, which is described by d_{ij} for the nearest neighbors, and by $\overrightarrow{D}_{ij}$ for the next-nearest neighbors.

As we know to obtain the energy spectrum from the tight-binding model, we need to rewrite Eq. (1.79) in form of the Bloch state operators $c_\sigma^\dagger\left(\overrightarrow{k}\right)$ and $c_\sigma\left(\overrightarrow{k}\right)$ which can be described as

$$c_\sigma^\dagger\left(\overrightarrow{k}\right) = \frac{1}{\sqrt{N}}\sum_m e^{i\overrightarrow{q}\cdot\overrightarrow{R}_m} c_{m,\sigma}^\dagger, \tag{1.80}$$

$$c_\sigma\left(\overrightarrow{k}\right) = \frac{1}{\sqrt{N}}\sum_m e^{-i\overrightarrow{q}\cdot\overrightarrow{R}_m} c_{m,\sigma}, \tag{1.81}$$

where $\overrightarrow{R}_m$ is the lattice vector of an atomic site m, for a give sublattice and **m** runs over all **N** sites, forming a macroscopic system. After a Fourier transform, the Bloch Hamiltonian $H\left(\mathbf{k}\right)$, which one is expressed in the spin-pseudospin entangled basis $\{|A\uparrow\rangle, |B\uparrow\rangle, |A\downarrow\rangle, |B\downarrow\rangle\}$ is

$$H\left(\mathbf{k}\right) = \begin{pmatrix} \Delta - \lambda_I^A f_I\left(\mathbf{k}\right) & t f_{orb}\left(\mathbf{k}\right) & \lambda_{PIA}^A f_{PIA}\left(\mathbf{k}\right) & i\lambda_R f_R\left(\mathbf{k}\right) \\ t f_{orb}^*\left(\mathbf{k}\right) & -\Delta + \lambda_I^B f_I\left(\mathbf{k}\right) & -i\lambda_R f_R\left(-\mathbf{k}\right) & -\lambda_{PIA}^B f_{PIA}\left(\mathbf{k}\right) \\ \lambda_{PIA}^A f_{PIA}^*\left(\mathbf{k}\right) & i\lambda_R f_R^*\left(-\mathbf{k}\right) & \Delta + \lambda_I^A f_I\left(\mathbf{k}\right) & t f_{orb}\left(\mathbf{k}\right) \\ -i\lambda_R f_R^*\left(\mathbf{k}\right) & -\lambda_{PIA}^B f_{PIA}^*\left(\mathbf{k}\right) & t f_{orb}^*\left(\mathbf{k}\right) & -\Delta - \lambda_I^B f_I\left(\mathbf{k}\right) \end{pmatrix}. \tag{1.82}$$

Considering $a = \frac{\sqrt{3}}{2}a_{cc}$, $b = \frac{3}{2}a_{cc}$, the *spin-orbital tight-binding functions* $f_{orb}\left(\mathbf{k}\right)$, $f_R\left(\mathbf{k}\right)$, $f_I\left(\mathbf{k}\right)$, $f_{PIA}\left(\mathbf{k}\right)$ are described by

$$f_{orb}\left(\mathbf{k}\right) = \exp\left(-ik_y a\right)\left[1 + 2\exp\left(ik_y b\right)\cos\left(k_x a\right)\right], \tag{1.83}$$

$$f_R(\mathbf{k}) = \frac{2}{3}\exp(-ik_y a)\left[1 + 2\exp(ik_y b)\cos\left(k_x a - \frac{2\pi}{3}\right)\right], \tag{1.84}$$

$$f_I(\mathbf{k}) = \frac{4}{3\sqrt{3}}\sin(k_x a)\left[\cos(k_y b) - \cos(k_x a)\right], \tag{1.85}$$

$$f_{PIA}(\mathbf{k}) = \left(\frac{4i}{3}\right)\left[\cos(k_y b)\sin(k_x a) + \sin(2k_x a) - i\sqrt{3}\cos(k_x a)\sin(k_y b)\right], \tag{1.86}$$

where k_x and k_y are the cartesian components of the center of the **FBZ** (Γ).

1.2.9.3. Continuous model for graphene/TMDC's

In the continuous model, the Hamiltonian from Eq. (1.82) is expanded for small momenta around the **K** and **K'** point of the first Brillouin zone (**FBZ**), and by fitting the electronic structure and spin texture to the *ab initio* results, the strength of the various **SOC** parameters can be estimated. The model is given as

$$H = H_{orb} + H_{SOC}, \tag{1.87}$$

where the first term

$$H_{orb} = \hbar\nu_F(\kappa\sigma_x k_x + \sigma_y k_y) + \Delta\sigma_z, \tag{1.88}$$

represents the orbital part of the Hamiltonian, described by the Dirac equation with v_F the Fermi velocity, σ_i the Pauli matrices acting on the pseudospin subspace, $\kappa = 1(-1)$ for the **K** (**K'**) valley, and Δ a mass term arising from a weak superlattice effect induced by the TMDC [113, 116]. Being H_{SOC} composed by

$$H_{SOC} = H_R + H_{PIA} + H_I + H_{VZ} + H_{\Delta PIA}, \tag{1.89}$$

with:

$$\begin{aligned} H_R &= \lambda_R(\sigma_x s_y - \sigma_y s_x), \\ H_{PIA} &= a\lambda_{PIA}\sigma_z(k_x s_y - k_y s_x), \\ H_I &= \lambda_I \kappa \sigma_z s_z, \\ H_{VZ} &= \lambda_{VZ}\kappa s_z, \\ H_{\Delta PIA} &= a\lambda_{\Delta PIA}(k_x s_y - k_y s_x), \end{aligned} \tag{1.90}$$

- The first element is a Rashba SOC with strength λ_R, arising from a perpendicular electric field.

- H_{PIA} is a SOC that appears due to the absence of horizontal reflection symmetry and which renormalizes the Fermi velocity.

- H_I is the intrinsic SOC in graphene, which opens a topological gap $2\lambda_I$ at the Dirac point [86].

- H_{VZ} is a valley-Zeeman term, which spin polarizes the bands out of the graphene plane with opposite orientation in the K and K′ valleys, also known as spin-valley locking.

- $H_{\Delta PIA}$ is a second-order Rashba term that causes a k-linear splitting of the bands, as in traditional 2D electron gases (**2DEGs**) with Rashba **SOC** [117]. Except for the **PIA** terms, this Hamiltonian is the same as that considered in other works [76, 103, 78, 114].

The values of these parameters are on the order of ∼1 meV except for the intrinsic **SOC**, which remains on the order of a few tens of μeV, similar to pristine graphene [113]. In the spin-pseudospin basis, the continuum full Hamiltonian, including the valley index ($\tau = \pm 1$), is described in Ref. [118] by

$$H_{eff} = \begin{pmatrix} \Delta + \tau\lambda_I^A & E_{\mathbf{k}} & w^* E_{PIA}^A & E_R^+ \\ E_{\mathbf{k}}^* & -\Delta - \tau\lambda_I^B & E_R^- & w^* E_{PIA}^B \\ w E_{PIA}^A & \left(E_R^-\right)^* & \Delta - \tau\lambda_I^A & E_{\mathbf{k}} \\ \left(E_R^+\right)^* & w E_{PIA}^B & E_{\mathbf{k}}^* & -\Delta + \tau\lambda_I^B \end{pmatrix}, \tag{1.91}$$

where $E_{\mathbf{k}}^* = (\tau \, \exp(i\tau\theta))\, \hbar\nu_F \mathbf{k}$, $E_R^{\pm} = i(\tau \pm 1)\, \lambda_R$, $E_{PIA}^{A,B} = a\mathbf{k}\lambda_{PIA}^A$, and $w^* = i \, \exp(i\theta)$.

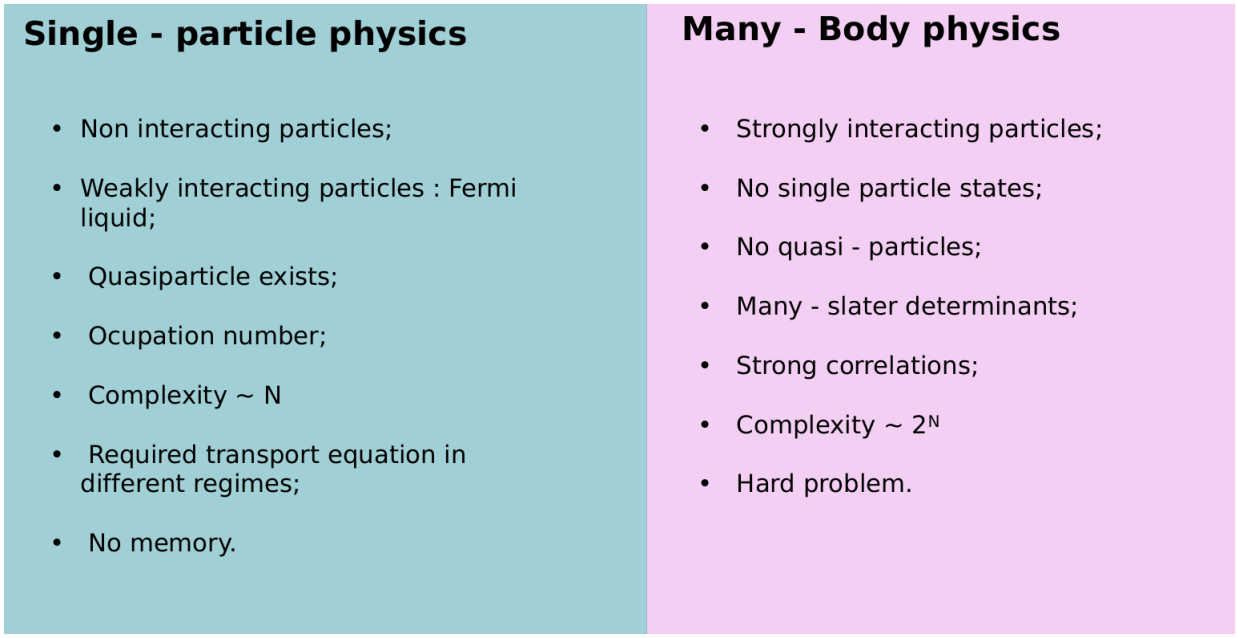

Figure 1.9.: *Many-body physics vs. single-particle physics.*

1.2.10. Entanglement in condensed matter

An entanglement measure quantifies how much entanglement is contained in a quantum state. Formally it is any non-negative real function of a state which cannot increase under local operations and classical communication (**LOCC**) - this is due to the monotonicity of this function.

This quantify goes to zero for separable states. In our work presented here, for exploring bipartite intra-particle entanglement in a closed system, we introduce the concurrence as the main quantity for this specific case for convenience.

In general, the problem of quantifying the entanglement in condensed matter is not trivial. Still, in our case, we are working on the simplest case that consists of a bipartite system within the a single particle approximation.

Let us point out the main differences between two huge classes of systems in condensed matter to understand the complexity of studying entanglement on the hardest platforms and in comparison with our platform that naively could look simple in the computational point of view but not trivial from the complex physics of the weakly correlated system known as graphene.

We choose to point out this difference because many materials regarding this topic are not explicitly explained. Those unfamiliar with this subject can confuse different regimes to tackle entanglement in condensed matter. Thus, we can visualize the

main difference between single particles in many-body physics in the Fig. 1.9

Thus, we can imagine that tackling bipartite entanglement is a pretty straightforward question at first glance. However, connecting entanglement and quantum transport in Dirac matter sometimes could be a bumpy road due to the physical interpretation...

1.2.11. Correlations

The search for non-local correlations in experiments is key to understand the ultimate nature of quantum phenomena, and technically demands for analysing large set of experimental data of correlated physical events. After many repetitions of similar experimental events, distribution probabilities of correlations between events are extracted and allow to determine the presence and strength of entanglement. Experiments of correlations are excellent to invalidate classical concepts to describe quantum phenomena, because they does not depend of any particular model, just of the statistic outcomes obtained in the experiment [119, 120].

Simplest case: scenario (2,2,2)

Consider the simplest scenario for studying correlations composed by two parts **A** and **B** (Alice and Bob), where each of the parts can perform two possible measurements with two possible outcomes, as we can see in the Fig. 1.10

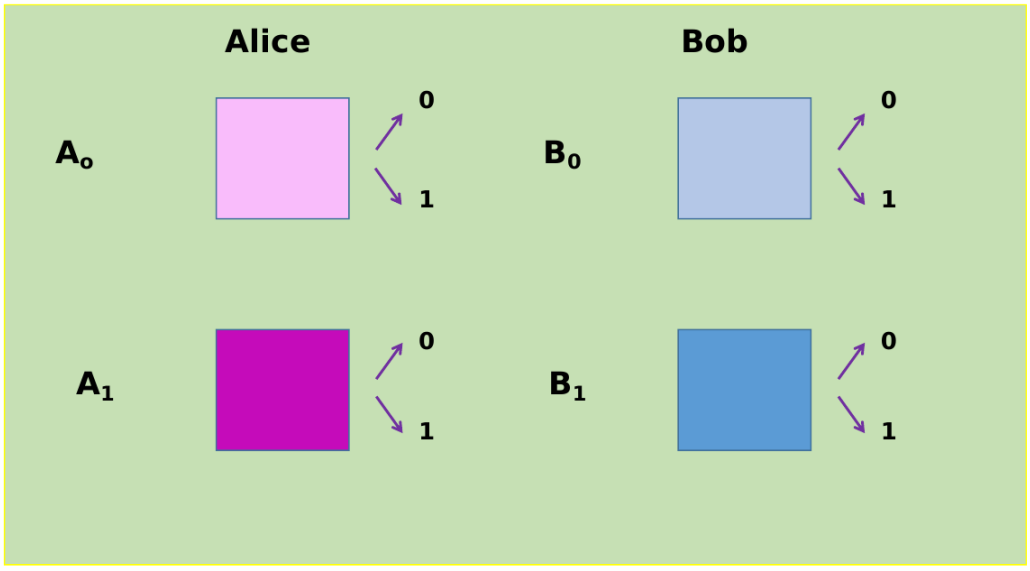

Figure 1.10.: ***Bipartite correlation:*** *Alice can choose to perform the measurements A_0 and A_1, each with two possible outcomes: 0 or 1. The same happens to Bob part.*

Clauser-Horner-Shimony-Holt inequality

The CHSH inequalities were proposed in 1969 by J. Clauser, M. Horne, A. Shimony and R. Holt [121]. They are one of the famous versions of the Bell inequalities because they could allow direct experimental check . According to the scheme presented in the Fig. 1.10, consider the expression

$$\beta_{CHSH} = p_{a=b|A_0,B_0} - p_{a\neq b|A_0,B_0} + p_{a=b|A_0,B_1} - p_{a\neq b|A_0,B_1} + \tag{1.92}$$

$$+ p_{a=b|A_1,B_0} - p_{a\neq b|A_1,B_0} - p_{a=b|A_1,B_1} + p_{a\neq b|A_1,B_1},$$

where

$$p_{a=b|A_x,B_y} = p_{0,0|A_x,B_y} + p_{1,1|A_x,B_y}, \tag{1.93}$$

$$p_{a\neq b|A_x,B_y} = p_{1,0|A_x,B_y} + p_{0,1|A_x,B_y}, \tag{1.94}$$

we can also define the correlator in terms of these probabilities such as

$$E(A_x, B_y) \equiv p_{a=b|A_x,B_y} - p_{a\neq b|A_x,B_y} \tag{1.95}$$

Thus, we have

$$\beta_{CHSH} = E(A_0, B_0) + E(A_0, B_1) + E(A_1, B_0) - E(A_1, B_1). \tag{1.96}$$

Defining the operators:

$$A_x = \Pi^0_{A_X} - \Pi^1_{A_X}, \tag{1.97}$$

$$B_y = \Pi^0_{B_y} - \Pi^1_{B_y}, \tag{1.98}$$

where $\left\{\Pi^0_{A_X}, \Pi^1_{A_X}\right\}$ are elements of the **POVM** (projective measurements which

will be defined in the **Chapter 2**) of the measurement A_x. Consider $\left\{\Pi^0_{B_y}, \Pi^1_{B_y}\right\}$ elements of the **POVM** of the measurement B_y. Being $\|\mathbf{.}\|$the norm defined as the singular value of an operator and knowing the $\sum \Pi^0_{A_X} = 1$, $\Pi^0_{A_X} \geq 0$, one obtains that $\|\mathbf{A_x}\| \leq 1$. The same conditions are valid for the B part. Therefore, we can relate these observables to the **CHSH** inequality, such as

$$\mathcal{B}_{\mathbf{CHSH}} \equiv \mathbf{A_0} \otimes \mathbf{B_0} + \mathbf{A_0} \otimes \mathbf{B_1} + \mathbf{A_1} \otimes \mathbf{B_0} - \mathbf{A_1} \otimes \mathbf{B_1}, \tag{1.99}$$

thus, we have

$$\langle \mathcal{B}_{\mathbf{CHSH}} \rangle = \beta_{CHSH}. \tag{1.100}$$

Knowing the $\langle \mathcal{B}_{\mathbf{CHSH}} \rangle$, we can check if the correlations generated by the quantum mechanics are local, i.e. obeys $|\beta_{CHSH}| \leq 2$.

Proof:

Being CHSH expression given by:

$$CHSH = A_0B_0 + A_0B_1 + A_1B_0 - A_1B_1, \tag{1.101}$$

where A_i and B_j are variables that can take the value $+1$ and -1. Now, let's compute its maximum absolute value:

$$max_{Ai=\pm1,Bj=\pm1}|CHSH| \tag{1.102}$$

Rewriting the CHSH expression as follows:

$$max|A_0(B_0 + B_1) + A_1(B_0 - B_1)| \tag{1.103}$$

Now, since B_0 and B_1 are $+1$ or -1, you have two possibilities:

1. $B_0 = B_1 = B$ and then $max|CHSH| = 2|A_0B| = 2$, because they are signs;
2. $B_0 = -B_1 = B$ and then $max|CHSH| = 2|A_1B| = 2$, because they are signs.

Therefore $|CHSH| \leq 2$. Next, consider as an example that the quantum mechanics violates the restrictions imposed by non-locality. Suppose that Alice and Bob share

the entangled state:

$$|\psi\rangle = \frac{1}{\sqrt{2}}\left(|01\rangle - |10\rangle\right), \tag{1.104}$$

and they can perform the measurements of the observables

$$A_0 = \sigma_z, \qquad A_1 = \sigma_x; \tag{1.105}$$

$$B_0 = \frac{1}{\sqrt{2}}\left(\sigma_z + \sigma_x\right), \qquad B_1 = \frac{1}{\sqrt{2}}\left(\sigma_z - \sigma_x\right). \tag{1.106}$$

Thus, calculating the expectation value of $\mathcal{B}_{CHSH}$ for the state of the Eq. (1.104), the violation of the **CHSH** inequality can be expressed by

$$\begin{aligned}\langle\psi|\,\mathcal{B}_{\mathbf{CHSH}}\,|\psi\rangle &= \langle\psi|\,\mathbf{A_0}\otimes\mathbf{B_0} + \mathbf{A_0}\otimes\mathbf{B_1} + \mathbf{A_1}\otimes\mathbf{B_0} - \mathbf{A_1}\otimes\mathbf{B_1}\,|\psi\rangle \\ &= -2\sqrt{2}.\end{aligned} \tag{1.107}$$

Here we will not enter into more details about the foundations of the non-locality. However, it is worth mentioning a famous result obtained by Boris Tsirelson, which establishes a maximum value for the violation of CHSH inequality for quantum mechanics.

Theorem 1: $\|\mathcal{B}_{\mathbf{CHSH}}\| \leq 2\sqrt{2}$.

Proof:

$$\begin{aligned}\left(\mathcal{B}_{\mathbf{CHSH}}\right)^2 &= \left(\mathbf{A_0}\otimes\mathbf{B_0} + \mathbf{A_0}\otimes\mathbf{B_1} + \mathbf{A_1}\otimes\mathbf{B_0} - \mathbf{A_1}\otimes\mathbf{B_1}\right)^2 \\ &\leq 4\cdot\mathbf{1} - [A_0, A_1]\otimes[B_0, B_1],\end{aligned} \tag{1.108}$$

where $[X, Y] = XY - YX$ is the commutator. Given the arbitrary operators X and Y we have

$$\|[X, Y]\| = \|XY - YX\| \leq 2\,\|X\|\,\|Y\|, \tag{1.109}$$

$$\|[X \otimes Y]\| = \|X\| \, \|Y\| \,,$$

$$\|X^2\| = \|X\|^2 \,.$$

Therefore, from Eq. (1.108), we have

$$\begin{aligned} \|\mathcal{B}_{\mathbf{CHSH}}\|^2 &\leq 4 + 4 \, \|\mathbf{A_0}\| \, \|\mathbf{A_1}\| \, \|\mathbf{B_0}\| \, \|\mathbf{B_1}\| \,, \\ &\leq 8, \\ &\leq 2\sqrt{2}. \end{aligned} \tag{1.110}$$

In conclusion, according to quantum mechanics, the value of β_{CHSH} is limited by $\beta_{CHSH} \leq 2\sqrt{2}$, this result is also known as the **Tsirelson bound**.

With this inequality in mind, one can wondering:

Is the entanglement the unique condition to have non-local correlations?

Entanglement it is necessary condition for non-locality, but is not sufficient. There exist entangled states for which the correlations admit a description by hidden local variable models. But, this kind of investigation is not the topic of this thesis.

1.2.11.1. Separable states

Consider a separable state of a system composed by n parts, such as

$$\rho = \sum_i p_i \rho_1^i \otimes \rho_2^i \otimes \cdots \otimes \rho_n^i, \qquad p_i \geq 0, \quad \sum_i p_i = 1. \tag{1.111}$$

For all local measurements $\{\Pi_{A_{X1}} \otimes \Pi_{A_{X2}} \otimes \cdots \otimes \Pi_{A_{Xn}}\}$ performed in this state, the correlations obtained can be described as

$$\begin{aligned} p\left(a_1, \cdots, a_n | A_{x1}, \cdots, A_{xn}\right) &= tr\left[\rho \left(\Pi_{A_{X1}}^{a1} \otimes \Pi_{A_{X2}}^{a2} \otimes \cdots \otimes \Pi_{A_{Xn}}^{an}\right)\right], \\ &= tr\left[\left(\sum_i p_i \rho_1^i \otimes \rho_2^i \otimes \cdots \otimes \rho_n^i\right) \left(\Pi_{A_{X1}}^{a1} \otimes \Pi_{A_{X2}}^{a2} \otimes \cdots \otimes \Pi_{A_{Xn}}^{an}\right)\right], \\ &= \sum_i p_i tr\left(\rho_1^i \Pi_{A_{X1}}^{a1}\right) tr\left(\rho_1^i \Pi_{A_{X2}}^{a2}\right) \cdots tr\left(\rho_n^i \Pi_{A_{Xn}}^{an}\right), \end{aligned} \tag{1.112}$$

$$= \sum_i p_i p^i_{a_1|A_{x1}} p^i_{a_2|A_{x2}\ldots} p^i_{a_n|A_{xn}},$$

which consists in a classically correlated probability distribution, which can be associated with hidden local variable theory. In conclusion, all separable states give to local correlations.

1.2.11.2. Bipartite entanglement

It was showed that all pure bipartite entanglement violate some Bell inequalities, result which has been generalized by Popescu and Rohrlich [120] for n entangled particles.

Theorem 2 (Two-qubit case): All bipartite pure entangled states violates the CHSH inequality for some choice of observables A_0, A_1, B_0, B_1.

Proof:

A two-qubit pure state can be described in its Schmidt decomposition in the form:

$$|\psi\rangle = \mu_1 |0\rangle |0\rangle + \mu_2 |1\rangle |1\rangle , \tag{1.113}$$

where μ_1, μ_2 are real positive numbers being $\mu_1^2 + \mu_2^2 = 1$. Consider $\{|0\rangle, |1\rangle\}$ the bases of the H_A and H_B that can represent different directions of the spin in each system. Assuming that a state is entangled $\mu_1, \mu_2 > 0$, for this bipartite system, the observables can be described by

$$A_0 = \overrightarrow{a}_0.\overrightarrow{\sigma}, \qquad A_1 = \overrightarrow{a}_1.\overrightarrow{\sigma}, \qquad B_0 = \overrightarrow{b}_0.\overrightarrow{\sigma}, \qquad B_1 = \overrightarrow{b}_1.\overrightarrow{\sigma}, \tag{1.114}$$

where the axis are chosen in the way that $\{|0\rangle, |1\rangle\}$ are eigenvectors of σ_z for both parts (A,B), and $\overrightarrow{a}_0$, $\overrightarrow{a}_1$, $\overrightarrow{b}_0$, $\overrightarrow{b}_1$ are unit vectors in $\mathbb{R}^3$. To demonstrate this theorem, we need to choose these set of vectors in a way that the CHSH be violated. Thus, consider the Eq. (1.99), for our choice of observables, we have

$$\langle \mathcal{B}_{CHSH} \rangle = \left\langle \overrightarrow{a}_0.\overrightarrow{\sigma} \otimes \overrightarrow{b}_0.\overrightarrow{\sigma} \right\rangle + \left\langle \overrightarrow{a}_0.\overrightarrow{\sigma} \otimes \overrightarrow{b}_1.\overrightarrow{\sigma} \right\rangle + \tag{1.115}$$

$$+ \left\langle \overrightarrow{a}_1.\overrightarrow{\sigma} \otimes \overrightarrow{b}_0.\overrightarrow{\sigma} \right\rangle - \left\langle \overrightarrow{a}_1.\overrightarrow{\sigma} \otimes \overrightarrow{b}_1.\overrightarrow{\sigma} \right\rangle , \tag{1.116}$$

considering the unitary vectors as

$$\overrightarrow{a}_0 = (0, 0, 1)\,, \tag{1.117}$$

$$\overrightarrow{a}_1 = (1, 0, 1)\,, \tag{1.118}$$

$$\overrightarrow{b}_0 = (\sin\omega, 0, \cos\omega)\,, \tag{1.119}$$

$$\overrightarrow{b}_1 = \left(\sin\omega^{'}, 0, \cos\omega^{'}\right). \tag{1.120}$$

Thus, the expectation value of each term for a given state is

$$\left\langle \overrightarrow{a}.\overrightarrow{\sigma} \otimes \overrightarrow{b}.\overrightarrow{\sigma} \right\rangle_{\psi} = a_z b_z + 2\lambda_1\lambda_2\left(a_x b_x - a_y b_y\right), \tag{1.121}$$

Replacing the vectors in the equation above, we have

$$\langle \mathcal{B}_{CHSH} \rangle_{\psi} = \cos\omega - \cos\omega^{'} + 2\mu_1\mu_2\left(\sin\omega + \sin\omega^{'}\right), \tag{1.122}$$

choosing

$$\cos\omega = -\cos\omega^{'} = \frac{1}{\sqrt{1 + 4\left(\mu_1\mu_2\right)^2}} \tag{1.123}$$

$$\sin\omega = \sin\omega^{'} = \frac{2\mu_1\mu_2}{\sqrt{1 + 4\left(\mu_1\mu_2\right)^2}} \tag{1.124}$$

Consequently for these measurements, we have

$$\langle \mathcal{B}_{CHSH} \rangle_{\psi} = 2\sqrt{1 + 4\left(\mu_1 \mu_2\right)^2} > 2 \qquad if \qquad \mu_1 \neq \mu_2 \neq 0. \tag{1.125}$$

In summary, for some sets of measurements, all two-qubit pure states, there are correlations that realistic local theories cannot simulate. It is essential to highlight that the measures are chosen to violate the CHSH inequality. They depend on ψ through its basis and Schmidt coefficients. Thus, for evaluating the correlations between different states, a different set of observables needs to be measured. Generalizing these results, we can say:

All bipartite pure entangled state has non-local correlations for a specific set of measurements.

1.2.12. Density matrices and entanglement

Usually, in quantum theory, accessing the full physically relevant information of a given physical quantum state is not a trivial task since only probabilities are accessible to computation. One can further ask how to extract meaningful information from a subpart of a quantum system when its full physical information is out of reach? To perform such a task, the density operator ρ gives a proper mathematical quantity, which derives from the combined postulates of quantum mechanics and statistical mechanics.

As an illustration of the construction of density matrix as a product of these two branches of physics, one can outline the use of probability distribution. For example, we consider the case where the initial state of a system is not known, and we need to use a probability distribution as an initial state.

We learned in classical statistics mechanics that the probability distribution is useful to construct a partial description of a certain system. The density matrix plays a similar role in quantum statistical mechanics in this scenario. In general, the density matrices very often function as pre-probabilities that can be used to generate averages of the different observables. In some cases, the quantum wave function $|\psi\rangle$ need not denote the physical properties of a quantum system $[\psi]$.

In other words, it can be used as a mathematical function, e.g., to calculate probability amplitudes. Thus, in most cases, the density matrices are used as per-probability sense it will provide useful information about the system.

However, we should not think of that as a true physical property of a quantum system because it does not represent a "quantum reality". Therefore, referring to a density operator as a "state" of the system can be misleading in some cases. Although in classical statistical mechanics, it is common to refer to probability distribution as the "state" of the system, even if the distributions are not describing a physical property.

In our work, we use the density matrices because they play the role of state vectors. To access the entanglement structure, we need this "figure of merit", the density operator, to encode the available information about our state $|\psi\rangle$. Depending on if we use the full density matrix or the reduced density matrix, we can have different ways to analyze the entanglement of the Hamiltonian.

Regarding the properties of our most important tool to quantify the entanglement, we should consider some important details. First, the density matrix is a positive operator whose spectrum of eigenenergies is non-negative and whose trace is 1. Being $A > 0$ is a positive operator, its trace is greater than 0, and one can define a density matrix by the following expression:

$$\rho = \frac{A}{tr(A)}. \tag{1.126}$$

The eigenvalues of a density matrix ρ must be between 0 and 1. If one of the eigenvalues is 1, the other must be 0, and for the projector $\rho = \rho^2$ all these conditions define a pure state. Otherwise, if we have at least two nonzero eigenvalues, the density matrix is called a mixed state.

Mixed states can mainly model usual experimental studies. To conclude this brief description of the density matrix, we summarize some mathematical properties of this projector. The general representation of ρ can be defined as

$$\rho = \sum_i p_i \left|\psi_i\right\rangle \left\langle\psi_i\right|, \tag{1.127}$$

where p_i is the probability that the system of $|\psi_i\rangle$ state with $\sum_i p_i = 1$, where the eigenstates must be orthogonal and its decomposition is not unique. Finally, we have the basic assumptions regarding this operator

- $\rho^2 = \rho$ projector;
- $\rho^\dagger = \rho$ hermicity;
- $tr(\rho) = 1$ normalization;
- $\rho \geq 0$ positivity.

1.2.12.1. Pure and mixed state

A pure quantum state defines as a vector $|\psi_i\rangle$ in Hilbert space and density matrix for such a state is

$$\rho = |\psi_i\rangle \langle\psi_i| , \tag{1.128}$$

and

$$tr(\rho^2) = 1. \tag{1.129}$$

A mixed quantum state define as a probabilistic mixture of a pure state:

$$\rho = \sum_i p_i \rho_i = \sum_i p_i |\psi_i\rangle \langle\psi_i| , \tag{1.130}$$

and

$$tr(\rho^2) < 1. \tag{1.131}$$

The purity of a normalized quantum state is defined as:

$$\gamma = tr\left(\rho^2\right). \tag{1.132}$$

The purity provides the information on how much a state is mixed. The purity satisfies the relation:

$$\frac{1}{d} \leq \gamma \leq 1, \tag{1.133}$$

where d is the dimension of the Hilbert space upon which the state is defined. The upper bound is given by $tr(\rho) = 1$ and $tr(\rho^2) \leq tr(\rho)$. If ρ is a projection which describe a pure state we have the known relation $tr(\rho^2) = tr(\rho) = 1$. The lower bound is obtained by the completely mixed state, represented by matrix $\frac{I_d}{d}$.

Considering the Bloch sphere, pure states are represented by a point on the sphere's surface, whereas an interior point represents mixed states. Therefore, the purity of a state can be interpreted as its spatial proximity to the surface of the sphere.

If we have a density matrix, *how can we visualize it to know if it describes a mixed or a pure state?*

Consists in a coherent superposition of states $|\uparrow\rangle$,$|\downarrow\rangle$. In this case the off-diagonal elements that are responsible of coherence do exist and contain the phase information of the system. Example:

$$\rho_{pure} = \frac{1}{2}\begin{pmatrix} 1 & 1 \\ 1 & 1 \end{pmatrix}. \tag{1.134}$$

Consists in a incoherent superposition between the vectors of the basis. In this case, the off-diagonal elements are zero, thus the phase information is lost. Example:

$$\rho_{mixed} = \frac{1}{2}\begin{pmatrix} 1 & 0 \\ 0 & 1 \end{pmatrix}. \tag{1.135}$$

Where we have $\rho^2_{mixed} \neq \rho_{mixed}$.

As we already reinforce in this text, the physical prediction about a certain system depends on the density matrix. We cannot distinguish the different processes that result in a certain mixed state. It is possible to understand that different statistical mixture compositions carry the same incomplete information.

Therefore, we can introduce the concept of entropy for these quantum states. Thus, entropy is a measure of the degree of uncertainty of a quantum system. We have only partial information about a quantum system in a mixed system. The **entropy** measures how much is missing from the maximal information.

1.2.13. Quantifying the entanglement for bipartite systems

This section is based on the Whootters's seminal work Ref. (([122])), which introduced the concurrence as quantified of bipartite entanglement. Considering the simplest case, where we have a pure state, we get the concurrence from this:

$$C(\phi) = \left|\left\langle \Psi|\widetilde{\Psi}\right\rangle\right|; \tag{1.136}$$

Where $\left|\tilde{\Psi}\right\rangle$ is:

$$\left|\widetilde{\Psi}\right\rangle = (\sigma_{\mathbf{1y}} \otimes \sigma_{\mathbf{2y}}) \left|\Psi^*\right\rangle; \tag{1.137}$$

and the bit-flip operator that is described by kronecker product :

$$I = (\sigma_{1y} \otimes \sigma_{2y}) \Rightarrow \begin{pmatrix} 0 & 0 & 0 & -1 \\ 0 & 0 & 1 & 0 \\ 0 & 1 & 0 & 0 \\ -1 & 0 & 0 & 0 \end{pmatrix}. \tag{1.138}$$

This is a bit-flip operator which acts on quantum state as a two-qubit gate, in other words it is a inverter operator. This means that it rotates in 180^{o} the quantum state in the Bloch sphere. Let us visualize this through the map bellow, considering $|\Psi\rangle$ a quantum system:

$$|\Psi\rangle = \alpha\,|00\rangle + \beta\,|01\rangle + \gamma\,|10\rangle + \delta\,|11\rangle; \tag{1.139}$$

then,

$$|\Psi^*\rangle = \alpha^*\,|00\rangle + \beta^*\,|01\rangle + \gamma^*\,|10\rangle + \delta^*\,|11\rangle. \tag{1.140}$$

Appliyng this "inversor" to a quantum state with amplitudes conjugated, we get:

$$\left|\widetilde{\Psi}\right\rangle = (\sigma_{1y} \otimes \sigma_{2y}) \left|\Psi^*\right\rangle \Longrightarrow \begin{pmatrix} 0 & 0 & 0 & -1 \\ 0 & 0 & 1 & 0 \\ 0 & 1 & 0 & 0 \\ -1 & 0 & 0 & 0 \end{pmatrix} \begin{pmatrix} \alpha^* \\ \beta^* \\ \gamma^* \\ \delta^* \end{pmatrix} \Longrightarrow \tag{1.141}$$

$$\Longrightarrow -\delta^* \left|00\right\rangle + \gamma^* \left|01\right\rangle + \beta^* \left|10\right\rangle - \alpha^* \left|11\right\rangle .$$

Thus, we can think in a map for the "Inversor" operator as:

$$\left|00\right\rangle \rightarrow - \left|11\right\rangle \tag{1.142}$$

$$\left|01\right\rangle \rightarrow \left|10\right\rangle \tag{1.143}$$

$$\left|10\right\rangle \rightarrow \left|01\right\rangle \tag{1.144}$$

$$\left|11\right\rangle \rightarrow - \left|00\right\rangle \tag{1.145}$$

Returning to Concurrence formula for **pure state** (simplest case), we have:

$$C(\phi) = \left|\left\langle \Psi | \widetilde{\Psi} \right\rangle\right| \Longrightarrow |-\alpha^*\delta^* + \beta^*\gamma^* + \gamma^*\beta^* - \delta^*\alpha^*| \Rightarrow 2|-\alpha^*\delta^* + \beta^*\gamma^*| \tag{1.146}$$

Clearly, if $\alpha, \beta, \gamma, \delta$ are real, we have the module of the distance between $\alpha\delta$ and $\beta\gamma$

$$C(\phi) = |-2\alpha\delta + 2\beta\gamma|; \tag{1.147}$$

When, we have a separable state, this condition is required:

$$\alpha\delta = \beta\gamma \Longrightarrow C(\phi) = 0 \tag{1.148}$$

The concurrence can be calculated even for mixed states of a bipartite system. This quantifier's equivalent and more general definition can be constructed for mixed qubits following the procedure developed in Ref. [123, 124]. Initially, we can consider a pair of qubits of a pure state. We define a "magic basis" consisting of the following states (they are the Bell states with a determined phase):

$$|e_1\rangle = \frac{1}{2}\left(|\uparrow\uparrow\rangle + |\downarrow\downarrow\rangle\right) \tag{1.149}$$

$$|e_2\rangle = \frac{i}{2}\left(|\uparrow\uparrow\rangle - |\downarrow\downarrow\rangle\right) \tag{1.150}$$

$$|e_3\rangle = \frac{i}{2}\left(|\uparrow\downarrow\rangle + |\downarrow\uparrow\rangle\right) \tag{1.151}$$

$$|e_4\rangle = \frac{1}{2}\left(|\uparrow\downarrow\rangle - |\downarrow\uparrow\rangle\right) \tag{1.152}$$

When a pure state $|\psi\rangle$ can be described in this particular basis, as $|\psi\rangle = \sum_i \alpha_i |e_i\rangle$, its entanglement can be obtained in terms of its α_i components. Where C is defined by:

$$C\left(\psi\right) = \left|\sum_i \alpha_i^2\right| \tag{1.153}$$

Thus, we can look for a pure-state ensemble with minimum average entanglement for a given mixed state, our plan will be to look for a set of states that all have the same entanglement or concurrence. Thus, the "magic basis" has the properties:

1. The set of states which the density matrices are real when described in magic

basis is the same of the set of the mixtures of Bell state generalized.

2. The set of the unitary transformations are real when expressed in the magic basis and consist the same set the act independently over 2 qubits.

The Concurrence and Entropy of formation is described from R matrix, which is a function defined by:

$$R(\rho) = \sqrt{\sqrt{\rho}\rho^{*}\sqrt{\rho}} \tag{1.154}$$

Where ρ^{*} is a complex conjugated of ρ when described in the magic basis of following way $\rho^{*} = \sum_{ij} |e_i\rangle \langle e_j| \rho |e_i\rangle \langle e_j|$. The concurrence in general is not a measure that provides a clear physical meaning. But, with this construction from the magic basis we can get some physical interpretation. If we take the trace of the R function, we have a measure of "degree of equality" between ρ and ρ^{*}that assumes the value in the range of 0 to 1. In other words, the R function returns a measure about how close is ρ to generalized Bell mixture.

It worth pointing out that the eigenvalues of the R function are invariant under local unitary transformations of the separated qubits; this fact makes these eigenvalues particularly eligible for being part of a formula to quantify entanglement, because the entanglement is invariant under that kind of transformation (see Ref. [125]).

A simple example about the invariance of the entangled states can be described as follows. Initially, let us considering four Bell states are maximally entangled states. They correspond to the triplet and singlet states, thus:

$$\left|\varphi^{+}\right\rangle = \left(|00\rangle + |11\rangle\right)/2; \qquad \left|\varphi^{-}\right\rangle = \left(|00\rangle - |11\rangle\right)/2 \tag{1.155}$$

$$\left|\psi^{+}\right\rangle = \left(|01\rangle + |10\rangle\right)/2; \qquad \left|\psi^{+}\right\rangle = \left(|01\rangle - |10\rangle\right)/2 \tag{1.156}$$

By local operation we can go from one Bell state to another just acting under one qubit like this:

$$\sigma_x \left|\varphi^{+}\right\rangle = \left|\psi^{+}\right\rangle. \tag{1.157}$$

We can see a general case for a bipartite system, where we don't have a pure state. Thus, we can start by considering a density matrix $\rho_{1,2}$ that is needed to build the operator "R" should have the same dimensionality as the original density matrix. We want to repeat in Eq. (1.147) generalized for the case where we have our quantum system described by a density matrix.

With this, we need to apply the inverse operator (bit -flip) to the left and the right of the density matrix and take the square of this operator obtained to keep the dimensionality of the physics system, thus:

$$R = \sqrt{\rho_{1,2}(\sigma_{1y} \otimes \sigma_{2y})\rho^*_{1,2}(\sigma_{1y} \otimes \sigma_{2y})}. \tag{1.158}$$

Where, the inversion operation can be described by

$$\tilde{\rho} = (\sigma_{1y} \otimes \sigma_{2y})\rho^*_{1,2}(\sigma_{1y} \otimes \sigma_{2y}). \tag{1.159}$$

This inversor operator is equivalent to describing our density matrix on a magic basis. With this, we have a density matrix "R", which undergoes a transformation on the Bloch sphere, similarly to the case of computing the Von Neuman Entropy. We need to diagonalize the reduced density matrix and use the eigenvalues to express the entanglement entropy.

Here, we need to follow a similar approach. Reminding that both Von Neuman entropy as Concurrence are bipartite quantities to measure the entanglement in certain regions of Hilbert space.

Thus, the "R" matrix diagonalized (4x4) will have four nonzero system-dependent eigenvalues, so we have to solve a minimization problem. We know that the measure of entanglement adapts the Shannon Entropy in classical information theory. The measure needs to range from 0 (separable state) to 1 (maximally entanglement state).

Thus, mathematically we need to minimize the eigenvalues obtained through the diagonalization of the "R" operator. At the same time, from a physical perspective, we will have to scrutinize the properties of some average of the concurrence, an important study when we have a Hamiltonian that depends on parameters as in condensed matter systems. Therefore, the most important formulation of the concurrence is summarized as

$$C(\phi) = max\{0, \tilde{\lambda}_1 - \tilde{\lambda_2} - \tilde{\lambda_3} - \tilde{\lambda_4}\}, \tag{1.160}$$

where these eigenvalues are in descending order of the matrix product.

1.3. Results I: entanglement in Rashba SOC graphene

Hamiltonian and entanglement of eigenstates

We consider a continuum model of graphene with Rashba SOC, which is induced by a perpendicular electric field or a substrate. The Hamiltonian is

$$\begin{aligned}\hat{\mathcal{H}} &= \hbar v_{\mathrm{F}} \left(\tau \hat{\sigma}_x k_x + \hat{\sigma}_y k_y\right) \otimes \hat{s}_0 \\ &\quad + \lambda_{\mathrm{R}} \left(\tau \hat{\sigma}_x \otimes \hat{s}_y - \hat{\sigma}_y \otimes \hat{s}_x\right), \end{aligned} \tag{1.161}$$

where v_{F} is the Fermi velocity, $\tau = \pm 1$ is the valley index, $\hbar \boldsymbol{k}$ is the electron momentum, λ_{R} is the Rashba SOC strength, and $\hat{s}$ ($\hat{\sigma}$) are the Pauli matrices for the spin (pseudospin) degree of freedom. The eigenenergies of $\hat{\mathcal{H}}$ are $\varepsilon_{\pm}^{\mathrm{e,h}} = \nu \varepsilon_{\pm}$, where $\nu = \pm 1$ for electrons/holes, $\varepsilon_{\pm} = \sqrt{\varepsilon^2 + \lambda_{\mathrm{R}}^2} \pm \lambda_{\mathrm{R}}$, and $\varepsilon = \hbar v_{\mathrm{F}} |\boldsymbol{k}|$. A typical bandstructure is shown in the left inset of Fig. 1.13, with the conduction and valence bands split by $2\lambda_{\mathrm{R}}$.

We limit ourselves to a single valley ($\tau = 1$) and express the Hamiltonian in the basis $\{|A\uparrow\rangle, |B\uparrow\rangle, |A\downarrow\rangle, |B\downarrow\rangle\}$. The first index refers to the pseudospin and the second index refers to the spin, with $\uparrow$ ($\downarrow$) denoting spin pointing along $+z$ ($-z$), perpendicular to the graphene plane. Like the spin, the pseudospin can point in an arbitrary direction on the Bloch sphere, given the proper distribution of the wave function between the A and B sublattices. For example, the state

$$\frac{1}{\sqrt{2}} \begin{bmatrix} 1 & 1 & 0 & 0 \end{bmatrix}^T = \frac{1}{\sqrt{2}} \left(|A\rangle + |B\rangle\right) \otimes |\uparrow\rangle \tag{1.162}$$

has pseudospin pointing along $+x$ and spin along $+z$, while

$$\frac{1}{2} \begin{bmatrix} 1 & -i & -1 & i \end{bmatrix}^T = \frac{1}{\sqrt{2}} \left(|A\rangle - i\,|B\rangle\right) \otimes \frac{1}{\sqrt{2}} \left(|\uparrow\rangle - |\downarrow\rangle\right) \tag{1.163}$$

has pseudospin along $-y$ and spin along $-x$. In this basis the eigenstates of the

Hamiltonian are

$$\left|\phi_{\pm}^{\mathrm{e,h}}\right\rangle = \frac{1}{\sqrt{N_{\pm}}}\left[\begin{array}{cccc} \mathrm{e}^{-\mathrm{i}\theta} & \nu\gamma_{\pm} & \pm i\gamma_{\pm} & \pm\nu i\mathrm{e}^{\mathrm{i}\theta} \end{array}\right]^{T}, \tag{1.164}$$

where $\theta = \arctan(k_y/k_x)$ is the direction of electron momentum, $\gamma_{\pm} = \varepsilon_{\pm}/\varepsilon$, and $N_{\pm} = 2(1+\gamma_{\pm}^2)$.

To quantify entanglement between the spin and pseudospin, we use the concurrence C_ψ of a given state $|\psi\rangle$ [122]. The concurrence has a 1-to-1 relationship with the von Neumann entropy, equals 0 for completely separable states, and equals 1 for maximally entangled states.

This entanglement measure was originally defined for mixed two-qubit systems, and has been extended to systems of many qubits [126]. Here we study pure states of the form $|\psi\rangle = \left[\begin{array}{cccc} a & b & c & d \end{array}\right]^{T}$, where the two qubits are the spin and pseudospin of the electron. In this case the concurrence is $C_\psi = 2|ad-bc|$. Before we present the concurrence regarding the four bands of Rashba SOC monolayer graphene, we must compare it with the spectrum of energy of these bands (see Fig. 1.11). We can check that at Dirac points. We have the minimum of energy, such as

In the following figure 1.12 , we have the degenerate behaviour of the concurrence for the four-band system described by Rashba SOC graphene.

The expression that describe the behaviour of concurrence in the simpelst case is expressed by

$$C_{\phi_{\pm}^{\mathrm{e,h}}} = \lambda_{\mathrm{R}}/\sqrt{\varepsilon^2+\lambda_{\mathrm{R}}^2}. \tag{1.165}$$

The eigenstates of the graphene-Rashba system are thus maximally entangled near the charge neutrality point, such as ($C_\phi \to 1$ as $\varepsilon \to 0$), and the entanglement decays as $1/\varepsilon$ at finite doping. This is shown in Fig. 1.13 for different values of $\lambda_{\mathrm{R}} = n\lambda$, with $\lambda = 37.5$ eV typical of graphene on SiO_2 or hBN [127]. The total spin and pseudospin of the eigenstates, $|\boldsymbol{s}| = |\boldsymbol{\sigma}| = \varepsilon/\sqrt{\varepsilon^2+\lambda_{\mathrm{R}}^2}$, are shown in the right inset. Both disappear as $\varepsilon \to 0$, a result of their becoming maximally entangled.

Entanglement dynamics

We now examine the entanglement of an arbitrary electron injected into graphene. This electron will be in an initial state $|\psi\rangle = \left[\begin{array}{cccc} a & b & c & d \end{array}\right]^{T}$ and will evolve in time as $|\psi(t)\rangle = \hat{U}(t)\,|\psi\rangle$, where $\hat{U}(t) = \sum_j \exp(-\mathrm{i}\varepsilon_j t/\hbar)\,|\phi_j\rangle\,\langle\phi_j|$ is the time evolution

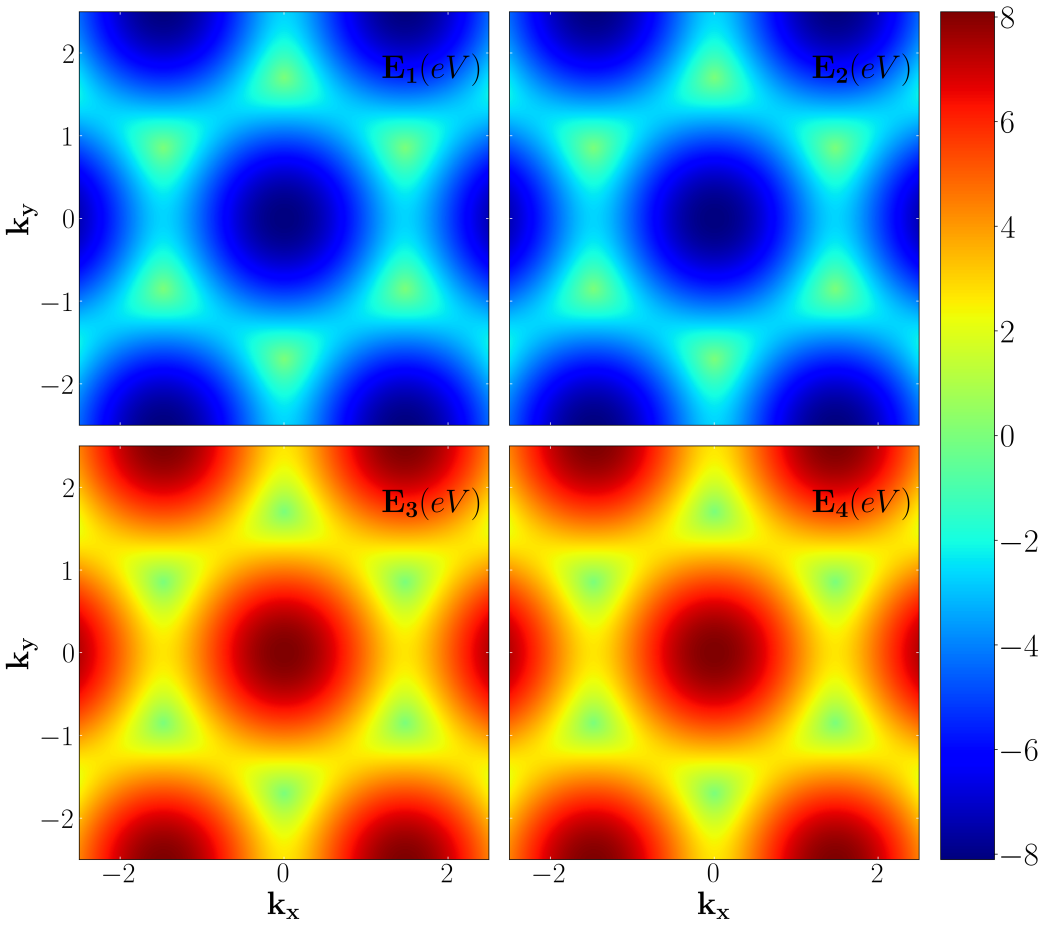

Figure 1.11.: *Energy spectrum for the four band Rashba SOC graphene monolayer.*

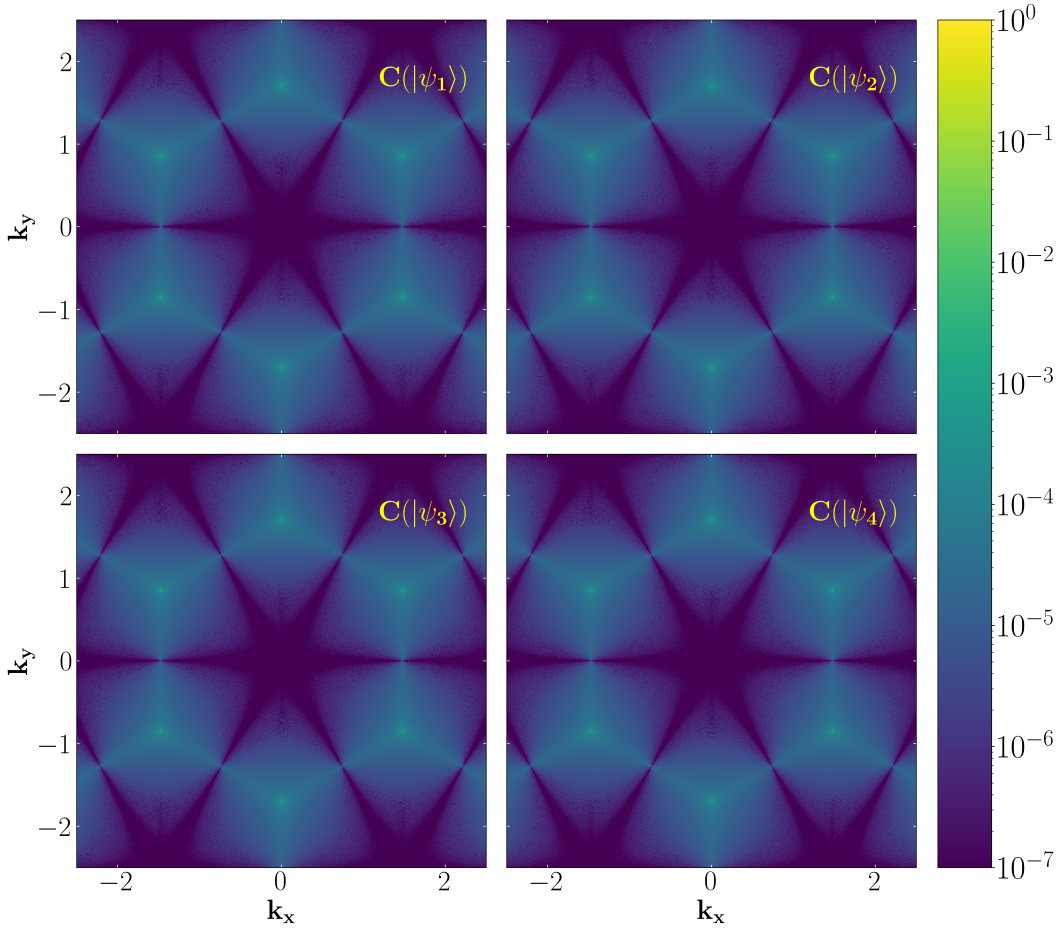

Figure 1.12.: *Concurrence computed for the four-band graphene with Rashba SOC. As we see, in this case we have same amount of entanglement in each of the four bands.*

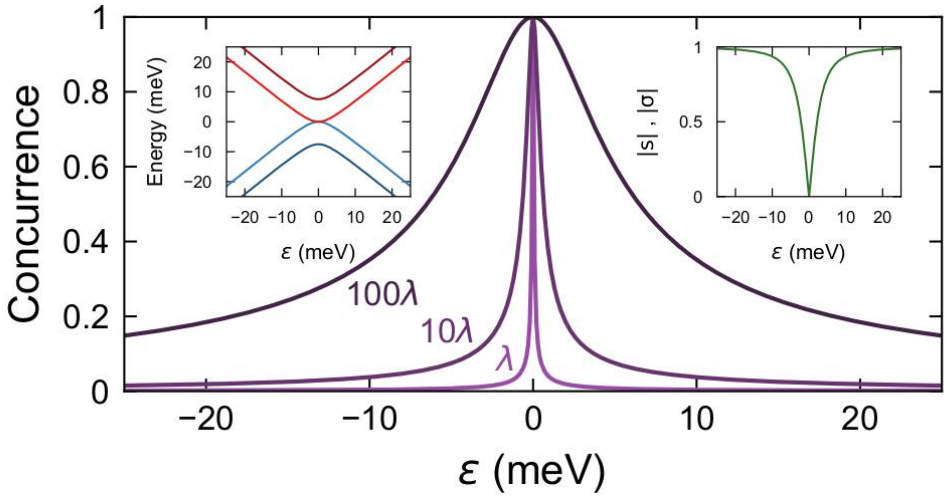

Figure 1.13.: *Concurrence of the eigenstates of the graphene-Rashba system near the charge neutrality point for different strengths of Rashba SOC. The left inset shows a typical band structure and the right inset shows the magnitude of the spin and pseudospin of the eigenstates. This figure was reprinted from Ref. [128], copyright (2020) by American Physical Society.*

operator, with ε_j and $|\phi_j\rangle$ the eigenenergies and eigenstates of $\hat{\mathcal{H}}$, described above. The concurrence of this state will thus evolve in time as $C_\psi(t) = 2|a(t)d(t) - b(t)c(t)|$.

We first highlight the entanglement dynamics of some specific initial states. Without loss of generality, we assume transport along the x-axis such that $\theta = 0$. Four states are considered :

$$\left|\psi_x^{\uparrow}\right\rangle = \frac{1}{\sqrt{2}}\begin{bmatrix} 1 & 1 & 0 & 0 \end{bmatrix}^T, \tag{1.166}$$

with pseudospin pointing along $+x$, parallel to the transport direction, and spin along $+z$;

$$\left|\psi_y^{\uparrow}\right\rangle = \frac{1}{\sqrt{2}}\begin{bmatrix} 1 & i & 0 & 0 \end{bmatrix}^T, \tag{1.167}$$

with pseudospin along $+y$, *perpendicular* to the transport direction, and spin along $+z$;

$$\left|\psi_{\text{Bell}}^{1}\right\rangle = \frac{1}{\sqrt{2}}\begin{bmatrix} 1 & 0 & 0 & 1 \end{bmatrix}^T, \tag{1.168}$$

a Bell state with maximal spin-pseudospin entanglement; and

$$\left|\psi^2_{\text{Bell}}\right\rangle = \frac{1}{\sqrt{2}}\begin{bmatrix} 0 & 1 & 1 & 0 \end{bmatrix}^T, \tag{1.169}$$

another Bell state with maximal entanglement. The entanglement dynamics of these states are shown in Fig. 1.14 at three different energies $\varepsilon = 0$, λ_{R}, and $10\lambda_{\text{R}}$, with $\lambda_{\text{R}} = 37.5$ eV, depicted in the top three panels.

We first analyze the concurrence dynamics at the charge neutrality point, $\varepsilon = 0$. The Bell state $|\psi^1_{\text{Bell}}\rangle$ maintains perfect entanglement while $|\psi^2_{\text{Bell}}\rangle$ oscillates between perfect and zero entanglement. Interestingly, $\left|\psi^{\uparrow}_{x,y}\right\rangle$ both develop nonzero entanglement despite being initially un-entangled, periodically reaching a maximum concurrence of 0.5. These behaviors can be understood by examining the eigenenergies and eigenstates of $\hat{\mathcal{H}}$ at $\varepsilon = 0$,

$$\begin{aligned}
\left|\phi^{\text{e,h}}_{+}\right\rangle &= \frac{1}{\sqrt{2}}\begin{bmatrix} 0 & \nu & i & 0 \end{bmatrix}^T, \text{ with } \varepsilon^{\text{e,h}}_{+} = \pm 2\lambda_{\text{R}}, \\
\left|\phi^{\text{e,h}}_{-}\right\rangle &= \frac{1}{\sqrt{2}}\begin{bmatrix} 1 & 0 & 0 & -i\nu \end{bmatrix}^T, \text{ with } \varepsilon^{\text{e,h}}_{-} = 0.
\end{aligned} \tag{1.170}$$

The eigenstates are maximally entangled, but their linear combinations can yield different behavior. The first Bell state can be written as

$$\left|\psi^1_{\text{Bell}}\right\rangle = \left(\frac{1-\text{i}}{\sqrt{2}}\right)\left|\phi^{\text{e}}_{-}\right\rangle + \frac{1+\text{i}}{\sqrt{2}}\left|\phi^{h}_{-}\right\rangle. \tag{1.171}$$

These eigenstates are degenerate ($\varepsilon^{\text{e,h}}_{-} = 0$) and $|\psi^1_{\text{Bell}}\rangle$ thus remains static with its initial $C_{\psi^1_{\text{Bell}}} = 1$. Meanwhile, the second Bell state can be written as

$$\left|\psi^2_{\text{Bell}}\right\rangle = \frac{1-\text{i}}{\sqrt{2}}\left|\phi^{\text{e}}_{+}\right\rangle + \frac{1+\text{i}}{\sqrt{2}}\left|\phi^{\text{h}}_{+}\right\rangle. \tag{1.172}$$

These eigenstates are separated in energy by $\varepsilon^{\text{e}}_{+} - \varepsilon^{\text{h}}_{+} = 4\lambda_{\text{R}}$, and $|\psi^2_{\text{Bell}}\rangle$ oscillates with $C_{\psi^2_{\text{Bell}}}(t) = |\cos(4\lambda_{\text{R}}t/\hbar)|$. The separable states can be written as

$$\left|\psi^{\uparrow}_{x}\right\rangle = \frac{1}{2}\left(\left|\phi^{\text{e}}_{+}\right\rangle - \left|\phi^{\text{h}}_{+}\right\rangle\right) + \frac{1}{2}\left(\left|\phi^{\text{e}}_{-}\right\rangle + \left|\phi^{\text{h}}_{-}\right\rangle\right), \tag{1.173}$$

and

$$\left|\psi_y^{\uparrow}\right\rangle = \frac{\mathrm{i}}{2}\left(\left|\phi_+^{\mathrm{e}}\right\rangle - \left|\phi_+^{\mathrm{h}}\right\rangle\right) + \frac{1}{2}\left(\left|\phi_-^{\mathrm{e}}\right\rangle + \left|\phi_-^{\mathrm{h}}\right\rangle\right). \tag{1.174}$$

The first term contributes an oscillatory component while the second term is static. The static component has zero concurrence

$$\left|\phi_-^{\mathrm{e}}\right\rangle + \left|\phi_-^{\mathrm{h}}\right\rangle \propto \begin{bmatrix} 1 & 0 & 0 & 0 \end{bmatrix}^T, \tag{1.175}$$

limiting the maximum concurrence that is reached, with $C_{\psi_{x,y}^{\uparrow}}(t) = \frac{1}{2}|\sin(4\lambda_{\mathrm{R}}t/\hbar)|$.

General expressions

To obtain the Concurrence considering as initial state a general state-ket $|\psi\rangle = \begin{bmatrix} a, & b, & c, & d \end{bmatrix}^T$, the general expression for this quantified was obtained using Mathematica as:

$$\begin{aligned}
C(t) \approxeq \tfrac{2}{\epsilon_0^2+\lambda_R^2} \Big| &\Big(\sin\left(\tfrac{\omega_R t}{2}\right)\Big(c\left(\sqrt{\epsilon_0^2+\lambda_R^2}\right)\cos\left(\tfrac{(\omega_+ +\omega_-)}{4}t\right) + (-id\epsilon_0 - b\lambda_R)\sin\left(\tfrac{(\omega_+ +\omega_-)}{4}t\right)\Big) + \\
&+\cos\left(\tfrac{\omega_R t}{2}\right)\Big(b\left(\sqrt{\epsilon_0^2+\lambda_R^2}\right)\cos\left(\tfrac{(\omega_+ +\omega_-)}{4}t\right) + (-ia\epsilon_0 + c\lambda_R)\sin\left(\tfrac{(\omega_+ +\omega_-)}{4}t\right)\Big)\Big)\cdot \\
&\cdot\Big(\cos\left(\tfrac{\omega_R t}{2}\right)\Big(c\left(\sqrt{\epsilon_0^2+\lambda_R^2}\right)\cos\left(\tfrac{(\omega_+ +\omega_-)}{4}t\right) + (-id\epsilon_0 - b\lambda_R)\sin\left(\tfrac{(\omega_+ +\omega_-)}{4}t\right)\Big) - \\
&-\sin\left(\tfrac{\omega_R t}{2}\right)\Big(b\left(\sqrt{\epsilon_0^2+\lambda_R^2}\right)\cos\left(\tfrac{(\omega_+ +\omega_-)}{4}t\right) + (-ia\epsilon_0 + c\lambda_R)\sin\left(\tfrac{(\omega_+ +\omega_-)}{4}t\right)\Big)\Big) - \\
&-\Big(\sin\left(\tfrac{\omega_R t}{2}\right)\Big(d\left(\sqrt{\epsilon_0^2+\lambda_R^2}\right)\cos\left(\tfrac{(\omega_+ +\omega_-)}{4}t\right) + (-ic\epsilon_0 + a\lambda_R)\sin\left(\tfrac{(\omega_+ +\omega_-)}{4}t\right)\Big) + \\
&+\cos\left(\tfrac{\omega_R t}{2}\right)\Big(a\left(\sqrt{\epsilon_0^2+\lambda_R^2}\right)\cos\left(\tfrac{(\omega_+ +\omega_-)}{4}t\right) + (-ib\epsilon_0 - d\lambda_R)\sin\left(\tfrac{(\omega_+ +\omega_-)}{4}t\right)\Big)\Big)\cdot \\
&\cdot\Big(\cos\left(\tfrac{\omega_R t}{2}\right)\Big(d\left(\sqrt{\epsilon_0^2+\lambda_R^2}\right)\cos\left(\tfrac{(\omega_+ +\omega_-)}{4}t\right) + (-ic\epsilon_0 + a\lambda_R)\sin\left(\tfrac{(\omega_+ +\omega_-)}{4}t\right)\Big) + \\
&+\sin\left(\tfrac{\omega_R t}{2}\right)\Big(-a\left(\sqrt{\epsilon_0^2+\lambda_R^2}\right)\cos\left(\tfrac{(\omega_+ +\omega_-)}{4}t\right) + (ib\epsilon_0 + d\lambda_R)\sin\left(\tfrac{(\omega_+ +\omega_-)}{4}t\right)\Big)\Big)\Big|.
\end{aligned}$$

where,

$$\omega_R = \frac{2\lambda_R}{\hbar},$$

$$\omega_+ = \frac{2\left(\sqrt{\varepsilon^2+\lambda_R^2}+\lambda_R\right)}{\hbar},$$

$$\omega_- = \frac{2\left(\sqrt{\varepsilon^2 + \lambda_R^2} - \lambda_R\right)}{\hbar}.$$

Note, as this expression already is simplified if we choose as initial state a random state, the result is not exact, what is natural because is a simplified expression. But, in case we use a initial Haar random pure state (see Ref. [129]), this expression match perfectly.

Low-energy limit

In the low-energy limit, $\lim_{\epsilon\to 0} C\,(t)$, the general expression simplifies to

$$C\,(t) = \left|(2ad - 2bc\cos\left(\frac{4\lambda_R t}{\hbar}\right) + \left(b^2 - c^2\right)\sin\left(\frac{4\lambda_R t}{\hbar}\right)\right|$$

Thus, for the all initial states that we can initialize the dynamic, our concurrence will be in terms of cosine or sine function or constant function.

Next we analyze the concurrence dynamics when approaching the high-energy limit (third row in Fig. 1.14). Here the concurrence of both Bell states oscillates as

$$C_{\psi^{1,2}_{\text{Bell}}}(t) \approx |\cos(2\lambda_{\text{R}} t/\hbar)|. \tag{1.176}$$

Meanwhile, the concurrence of $\left|\psi_x^{\uparrow}\right\rangle$ is small, approaching zero as $\varepsilon \to \infty$. In contrast, the concurrence of $\left|\psi_y^{\uparrow}\right\rangle$ is $C_{\psi_y^{\uparrow}}(t) \approx |\sin(2\lambda_{\text{R}} t/\hbar)|$, and periodically reaches *maximal* entanglement.

Remarkably, in graphene with Rashba SOC, an electron that initially has no intra-particle entanglement can become maximally entangled, and has the same average entanglement as the maximally-entangled Bell states.

To understand the origin of this, we now look at the problem from the perspective of spin and pseudospin dynamics. In the graphene-Rashba system, the spin and pseudospin will precess around effective magnetic and pseudomagnetic fields. By examining the Hamiltonian in Eq. (1.161) and considering transport along x, these effective fields are [35]

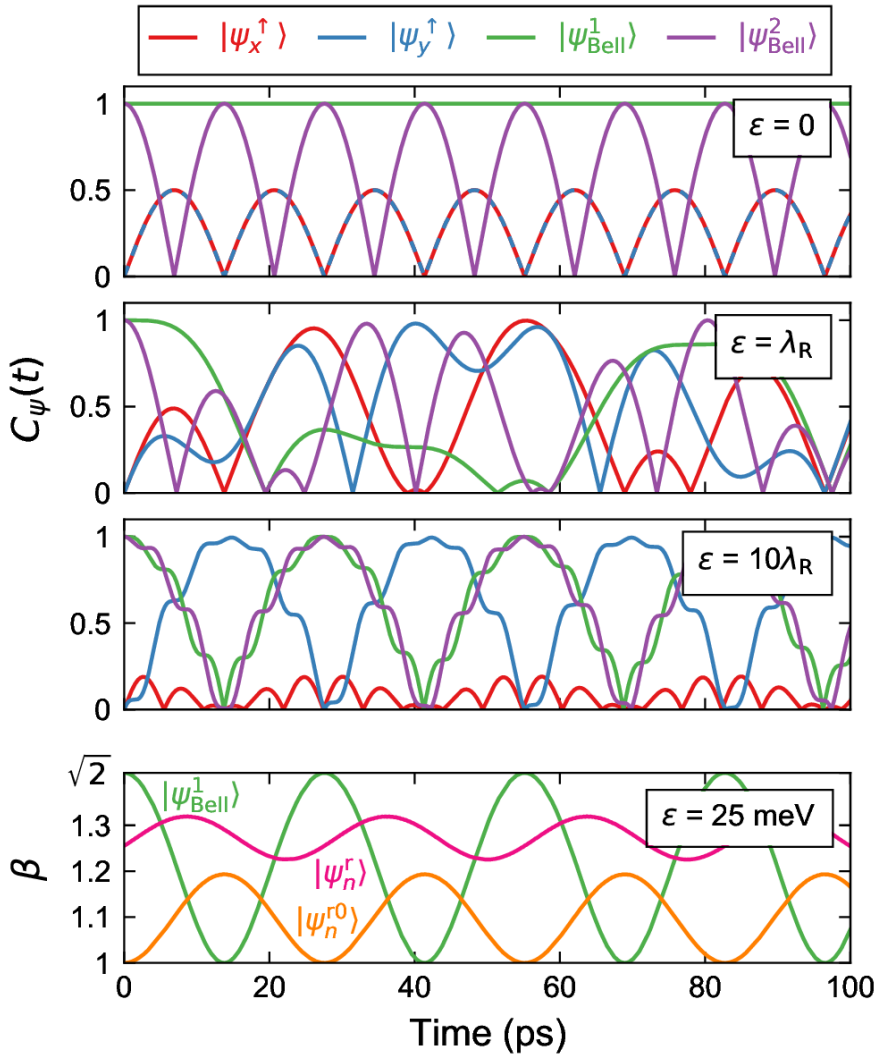

Figure 1.14.: *Entanglement dynamics in the graphene-Rashba system. The top three panels show the concurrence dynamics of the initial states* $\left|\psi_{x,y}^{\uparrow}\right\rangle$ *and* $\left|\psi_{Bell}^{1,2}\right\rangle$ *at energies* $\varepsilon = 0$, λ_R, *and* $10\lambda_R$, *with* $\lambda_R = 37.5$ *eV. The bottom panel shows the time-dependent violation of the CHSH inequality for* $|\psi_{Bell}^{1}\rangle$, *one instance of* $|\psi_n^{r}\rangle$, *and one instance of* $|\psi_n^{r0}\rangle$ *at* $\varepsilon = 25$ *meV. This figure was reprinted from Ref. [128], copyright (2020) by American Physical Society.*

$$
\begin{aligned}
\boldsymbol{B}_{\boldsymbol{s}}^{\text{eff}}(t) &= \lambda_{\text{R}}\left(-\langle\hat{\sigma}_y\rangle(t)\,,\,\langle\hat{\sigma}_x\rangle(t)\,,\,0\right), \\
\boldsymbol{B}_{\boldsymbol{\sigma}}^{\text{eff}}(t) &= \lambda_{\text{R}}\left(\langle\hat{s}_y\rangle(t)\,,\,-\langle\hat{s}_x\rangle(t)\,,\,0\right) \\
&\quad + \varepsilon\left(1\,,\,0\,,\,0\right),
\end{aligned}
\tag{1.177}
$$

where $\langle\hat{o}\rangle(t) \equiv \langle\psi(t)|\,\hat{o}\,|\psi(t)\rangle$. In the presence of Rashba SOC, the spin and pseudospin precess around one another with a frequency $\omega_{\text{R}} = 2\lambda_{\text{R}}/\hbar$. The pseudospin also precesses around a component of $\boldsymbol{B}_{\boldsymbol{\sigma}}^{\text{eff}}$ that is parallel to the momentum and has magnitude ε. In the high-energy limit ($\varepsilon \gg \lambda_{\text{R}}$), this term dominates the pseudomagnetic field.

Thus, when the initial pseudospin points along the momentum direction, as for $\left|\psi_x^{\uparrow},\right\rangle$ the pseudospin remains fixed along x and only the spin precesses, in the x-z plane. The spin and pseudospin thus remain well-defined and separable at all times, and the entanglement is negligible.

On the other hand, when the initial pseudospin is *perpendicular* to the momentum direction, as for $\left|\psi_y^{\uparrow}\right\rangle$, the pseudospin precesses rapidly in the y-z plane with frequency $\omega_{\varepsilon} = 2\varepsilon/\hbar$. This then enables mutual precession between spin and pseudospin driven by Rashba SOC, and the development of entanglement on the time scale ω_{R}^{-1}. In this way, a separable state whose pseudospin is not parallel to the direction of transport will develop finite intra-particle entanglement.

At intermediate energies where neither ε nor λ_{R} are dominant, more complex dynamics can emerge. This can be seen in second row of Fig. 1.14, where $\varepsilon = \lambda_{\text{R}}$. Here, multiple precession processes all coexist with similar weight and frequency, giving rise to more complex dynamics.

We finally note that this behavior may be connected to the concept of quantum synchronization. Recent work has found that synchronization between pairs of spins certifies the presence of entanglement [130], which resembles the situation at $\varepsilon = 0$, while the absence of synchronization does not preclude the development of entanglement, as we see in the high-energy limit.

Time-averaged entanglement

Figure 1.14 shows that the entanglement can vary significantly with energy while exhibiting complex dynamics. To quantify the overall degree of entanglement of a given state at a given energy, we consider the time-averaged concurrence $\langle C_{\psi}(t)\rangle$. This is shown in Fig. 1.15, with panel (a) corresponding to the initial states $\left|\psi_{x,y}^{\uparrow}\right\rangle$ and panel (b) to $\left|\psi_{\text{Bell}}^{1,2}\right\rangle$. For each state there are three curves, corresponding to

$\lambda_R = \lambda$, 10λ, and 100λ.

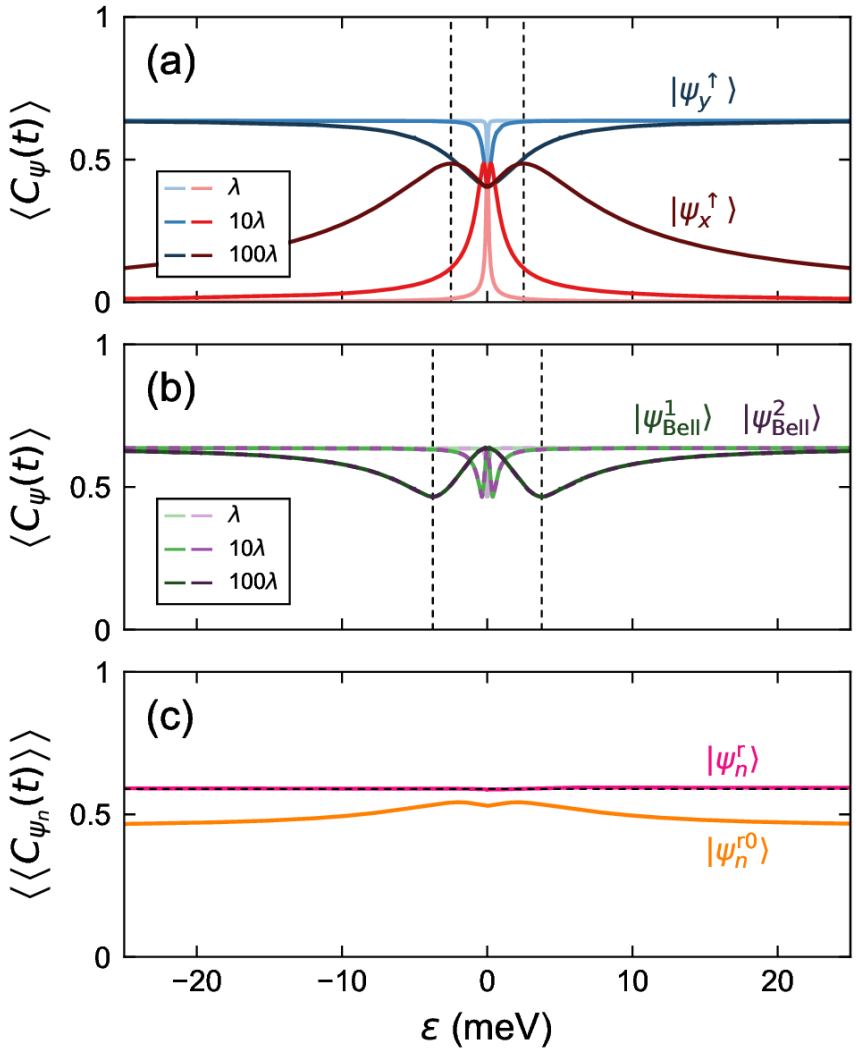

Figure 1.15.: *Time-averaged concurrence as a function of energy for the initial states (a) $|\psi^\uparrow_{x,y}\rangle$ and (b) $|\psi^{1,2}_{Bell}\rangle$. For each state there are three curves, corresponding to Rashba **SOC** strengths of $\lambda_R = \lambda$, 10λ, and 100λ, with $\lambda = 37.5$ eV. Panel (c) shows the time- and state-averaged concurrence, averaged over 1000 initial states $|\psi^r_n\rangle$ and $|\psi^{r0}_n\rangle$. The dashed line shows the average concurrence of the initial states $|\psi^r_n\rangle$ at $t = 0$. This figure was reprinted from Ref. [128], copyright (2020) by American Physical Society.*

At low energies, the average concurrences of $|\psi^\uparrow_{x,y}\rangle$ exhibit a local minimum, increasing away from $\varepsilon = 0$ as more complex dynamics come into play, as seen by comparing the top two panels of Fig. 1.14. At higher energies the average concurrence of $|\psi^\uparrow_y\rangle$ continues to grow, approaching $\langle C_\psi(t)\rangle_{\max} = \langle|\sin(\omega_R t)|\rangle = 2/\pi$. Meanwhile, for $|\psi^\uparrow_x\rangle$ the pseudomagnetic field dominates at higher energies, fixing the pseudospin and leading to a $1/\varepsilon$ decay of $\langle C_\psi(t)\rangle$.

This crossover occurs at $|\varepsilon| = (2/3)\lambda_{\mathrm{R}}$, marked by the vertical dashed lines in panel (a). In Fig. 1.15(b), both Bell states have the same energy dependence (except exactly at $\varepsilon = 0$, see below). Around $\varepsilon = 0$, $\langle C_\psi(t)\rangle$ approaches $2/\pi$ and decays with increasing energy. This can be seen in the top two rows of Fig. 1.14, where the complex spin-pseudospin dynamics at finite ε lead to an average reduction of the concurrence from its maximal behavior. The minimal average concurrence of the Bell states is reached at $|\varepsilon| = \lambda_{\mathrm{R}}$, shown by the vertical dashed lines. Above this energy, the Bell states converge back to $\langle C_\psi(t)\rangle_{\max} = \langle|\cos(\omega_{\mathrm{R}}t)|\rangle = 2/\pi$.

Here we note that $|\psi^1_{\mathrm{Bell}}\rangle$ has a constant $C_\psi = 1$ at $\varepsilon = 0$ (top row of Fig. 1.14). However, this occurs only exactly at $\varepsilon = 0$, and we have left this data point out of Fig. 1.15. For any $\varepsilon \neq 0$, the spin-pseudospin dynamics limit the average concurrence to $\langle C_\psi(t)\rangle < 2/\pi$. We also note that the Rashba SOC strength has no impact on the magnitude of $\langle C_\psi(t)\rangle$; its only effect is to rescale the energy dependence, as shown by the different curves in Fig. 1.15(a,b).

Entanglement dynamics for initially random states

We have studied four specific states and found they all exhibit dynamic spin-pseudospin entanglement. Particularly interesting is that the initially separable state $|\psi^\uparrow_y\rangle$ exhibits as much time-averaged intra-particle entanglement as the maximally-entangled Bell states.

This suggests that in order to generate intra-particle entanglement in graphene, it is not necessary to prepare entangled states. Instead, injecting appropriate "normal" states is sufficient. However, injecting an initial state with well-defined spin and pseudospin is also challenging.

The spin can be controlled to some degree with ferromagnetic contacts, but precise control of the pseudospin, determined by the weight and phase of the wave function on each sublattice, is more difficult. Given these issues, it is useful to consider a simpler situation, where a bulk metal contact injects an electrical current into graphene.

This current will consist of electrons with random initial states, which raises the question: what is the entanglement of an arbitrary state in graphene?

This can be quantified by averaging over many random initial states $|\psi_n\rangle$, such

that

$$\langle\langle C_{\psi_n}(t)\rangle\rangle \equiv \frac{1}{N}\sum_{n=1}^{N}\langle C_{\psi_n}(t)\rangle \tag{1.178}$$

is the average intra-particle entanglement in graphene. We consider two sets of random initial states,

$$\begin{aligned}
|\psi_n^{\mathrm{r}}\rangle &= \begin{bmatrix} a_n & b_n & c_n & d_n \end{bmatrix}^T, \\
|\psi_n^{\mathrm{r0}}\rangle &= \left\{\cos(\theta_n^{\mathrm{p}}/2)\,|A\rangle + \sin(\theta_n^{\mathrm{p}}/2)\mathrm{e}^{\mathrm{i}\phi_n^{\mathrm{p}}}\,|B\rangle\right\} \\
&\quad \otimes \left\{\cos(\theta_n^{\mathrm{s}}/2)\,|\uparrow\rangle + \sin(\theta_n^{\mathrm{s}}/2)\mathrm{e}^{\mathrm{i}\phi_n^{\mathrm{s}}}\,|\downarrow\rangle\right\}.
\end{aligned} \tag{1.179}$$

Each element of $|\psi_n^{\mathrm{r}}\rangle$ is a random complex number chosen from the normal distribution. This generates states that are equivalent to the action of a random unitary matrix on some reference state, which are uniform over the four-dimensional Hilbert space [131], with average initial concurrence $\langle C_{\psi_n^{\mathrm{r}}}(0)\rangle \approx 0.59$.

Meanwhile, $|\psi_n^{\mathrm{r0}}\rangle$ is a separable state, with $(\theta_n^{\mathrm{p}}, \phi_n^{\mathrm{p}})$ and $(\theta_n^{\mathrm{s}}, \phi_n^{\mathrm{s}})$ random spherical angles defining the orientations of the pseudospin and spin on the Bloch sphere. The set $\{|\psi_n^{\mathrm{r0}}\rangle\}$ thus represents all two-qubit states with zero initial entanglement.

The averages over these initial states are shown in Fig. 1.15(c). For all possible initial states, the average concurrence is independent of energy and equal to its initial value, $\langle\langle C_{\psi_n^{\mathrm{r}}}(t)\rangle\rangle = \langle C_{\psi_n^{\mathrm{r}}}(0)\rangle \approx 0.59$, shown by the magenta and the dashed black lines. Meanwhile, the average over unentangled initial states has an energy dependence similar to $\langle C_{\psi_x^{\uparrow}}(t)\rangle$ in Fig. 1.15(a), but with a slower decay. Importantly, $\langle\langle C_{\psi_n^{\mathrm{r0}}}(t)\rangle\rangle$ remains large over the entire energy range, around 0.5.

This indicates that large intra-particle entanglement is a general feature of graphene in the presence of spin-orbit coupling, even for states that are initially separable in spin and pseudospin.

Time-dependent Bell inequality violation

As shown above, intra-particle entanglement between spin and pseudospin is generally large in graphene with Rashba SOC. We have used intra-particle concurrence to quantify entanglement, but experimentally this is not directly measurable. Rather, entanglement is demonstrated through a violation of a Bell inequality [4, 5]. For pure

states there is a direct connection between the concurrence and maximal violation of the Clauser-Horne-Shimony-Holt (**CHSH**) variant of Bell's inequality [132], given by $\beta = \sqrt{1 + C_\psi^2}$ [133].

Thus, because the concurrence of a particular electron is time-dependent, its violation of the **CHSH** inequality also varies in time. We show this explicitly in Fig. 1.14 (Bottom panel), where we plot the time dependence of β for $|\psi^1_{\rm Bell}\rangle$, one instance of $|\psi^{\rm r}_n\rangle$, and one instance of $|\psi^{\rm r0}_n\rangle$ at $\varepsilon = 25$ meV. In all cases, β oscillates with frequency $\omega_{\rm R}$, highlighting the point that the Bell inequality violation is a dynamic and periodic quantity in the graphene-Rashba system.

1.4. Results II: entanglement in graphene/TMDC's

The full Hamiltonian corresponding to the continuous model for Graphene/TMDC (see Section 1.2.9) cannot be solve analytically.

This Hamiltonian above we cannot solve analytically. Thus, we will work with the approximation **graphene - valley - Zeeman - Rashba SOC**. The low energy approximation, restricted to an unique valley $\tau = 1$ or $\tau = 1$, leads to the following Hamiltonian:

$$H_{eff_{(\tau\mathbf{K}+\mathbf{k})}} = \hbar\nu_F(\tau\sigma_x k_x + \sigma_y k_y)\otimes 1_s + \lambda_R(\tau(\sigma_x\otimes s_y) - \sigma_y\otimes s_x) + \lambda_{VZ}\tau(1_s\otimes s_z), \quad (1.180)$$

or equivalently for $\tau = 1$ valley,

$$H_{eff_{((+1)\mathbf{K}+\mathbf{k})}} = \begin{pmatrix} \lambda_{VZ} & 0 & (k_x - ik_y)\hbar\nu_F & 0 \\ 0 & -\lambda_{VZ} & 2i\lambda_R & (k_x - ik_y)\hbar\nu_F \\ (k_x + ik_y)\hbar\nu_F & -2i\lambda_R & \lambda_{VZ} & 0 \\ 0 & (k_x + ik_y)\hbar\nu_F & 0 & -\lambda_{VZ} \end{pmatrix}, \quad (1.181)$$

with the energy spectrum

$$E_1 = -\sqrt{(\hbar\nu_F)^2\left(k_x^2 + k_y^2\right) + 2\lambda_R^2 + \lambda_{VZ}^2 - 2\sqrt{\lambda_R^4 + \left(k_x^2 + k_y^2\right)(\hbar\nu_F)^2\left(\lambda_R^2 + \lambda_{VZ}^2\right)}}, \quad (1.182)$$

$$E_2 = \sqrt{(\hbar\nu_F)^2\left(k_x^2+k_y^2\right)+2\lambda_R^2+\lambda_{VZ}^2-2\sqrt{\lambda_R^4+\left(k_x^2+k_y^2\right)(\hbar\nu_F)^2\left(\lambda_R^2+\lambda_{VZ}^2\right)}}, \quad (1.183)$$

$$E_3 = -\sqrt{(\hbar\nu_F)^2\left(k_x^2+k_y^2\right)+2\lambda_R^2+\lambda_{VZ}^2+2\sqrt{\lambda_R^4+\left(k_x^2+k_y^2\right)(\hbar\nu_F)^2\left(\lambda_R^2+\lambda_{VZ}^2\right)}}, \quad (1.184)$$

$$E_4 = \sqrt{(\hbar\nu_F)^2\left(k_x^2+k_y^2\right)+2\lambda_R^2+\lambda_{VZ}^2+2\sqrt{\lambda_R^4+\left(k_x^2+k_y^2\right)(\hbar\nu_F)^2\left(\lambda_R^2+\lambda_{VZ}^2\right)}}. \quad (1.185)$$

All parameters considered in our simulations for graphene/TMDC's are given in the Table 1.1 below

TMDC	t (eV)	Δ (meV)	λ_I^A (meV)	λ_I^B (meV)	λ_R (meV)	λ_{PIA}^A (meV)	λ_{PIA}^B (meV)
MoS_2	2.668	0.52	-0.23	0.28	0.13	-1.22	-2.23
$MoSe_2$	2.526	0.44	-0.19	0.16	0.26	2.46	3.52
WS_2	2.657	1.31	-1.02	1.21	0.36	-0.98	-3.81
WSe_2	2.507	0.54	-1.22	1.16	0.56	-2.69	-2.54

Table 1.1.: *Relevant parameters for graphene on different TMDCs. These values are taken from Ref. [113] and along this section we are called them "standard parameters" which means that we are including all orbitals and SOC terms presented here.*

In Fig. 1.16, we present the maximum entanglement contained in one of the four bands for each graphene/TMDC system here considered, using the parameters presented in Table 1.1.

As we see, in Fig. 1.16, all cases of graphene/TMDC's appear to show maximal entanglement around the K/K' points of the FBZ. However, a close look shows differences between the case. We also will play with some SOC terms and we will summarize some conclusions from this.

In all cases studied for us and considered here, the entanglement quantities from standard parameters presented in the table of parameters, are not affected by the

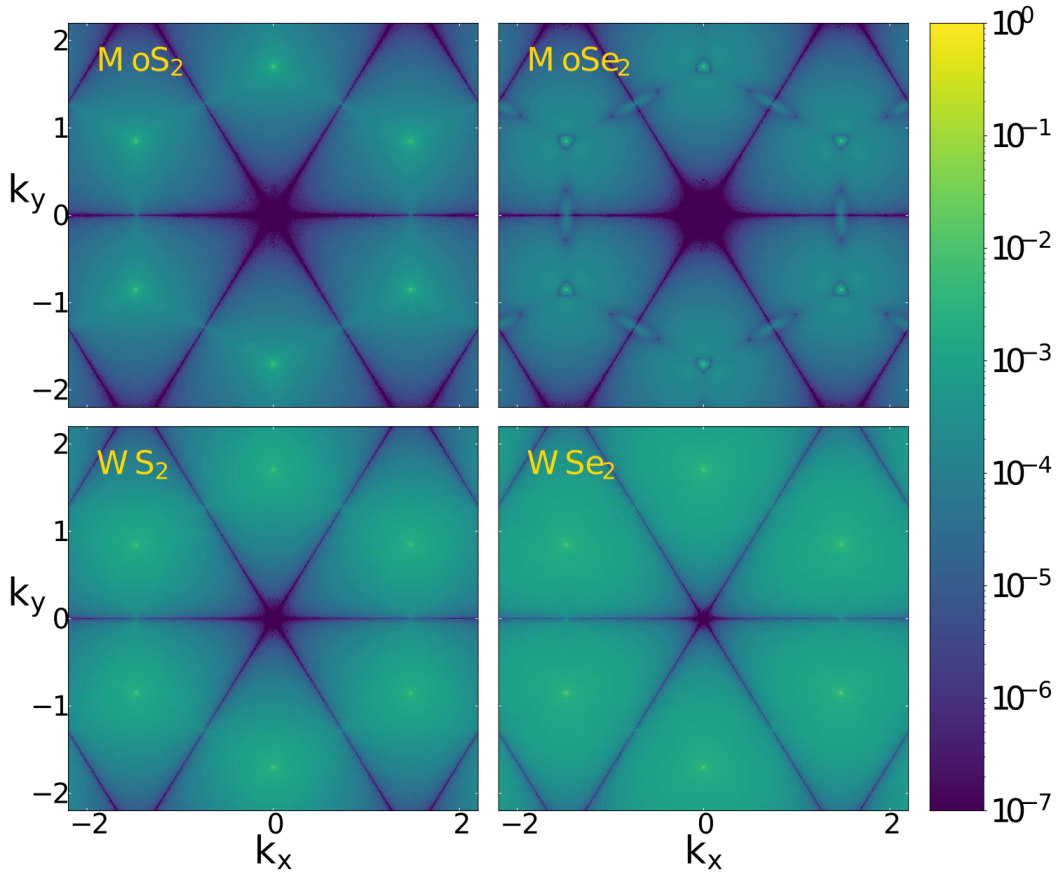

Figure 1.16.: *Concurrence for Graphene/TMDC's platform considering the concurrence* $C\left(|\psi_1\rangle\right)$ *for each system considered.*

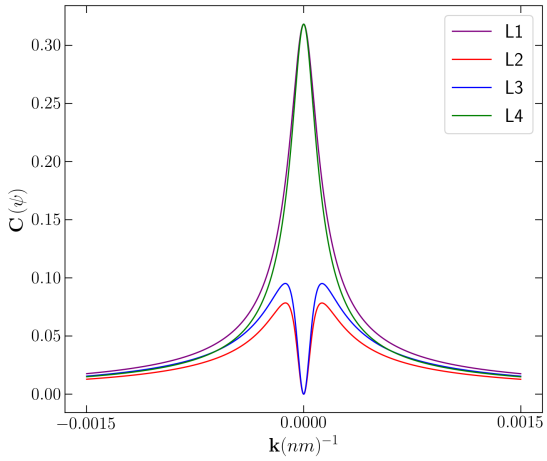

Figure 1.17.: *Zoom at Dirac point of each value of concurrence for the four band in graphene/$MoS_2$for standard parameters.*

condition of valley-Zeeman approximation, but another condition where we consider $\lambda_I^A = \lambda_I^B$, and $\lambda_{PIA}^A = \lambda_{PIA}^B$, we have a significant change in the concurrences values for each band. We can check this in the following tables of data.

Next, we will present some outcomes regarding the intra-particle entanglement for Graphene/TMDC platforms, and in the end, we will summarize what we learned about these systems.

a) Standard parameters considering all terms presented in Table 1.1:

Concurrence	K_-	K_+
$C\left(\lvert\psi_1\rangle\right)$	0.32	0.32
$C\left(\lvert\psi_2\rangle\right)$	0.01	0.01
$C\left(\lvert\psi_3\rangle\right)$	0.01	0.01
$C\left(\lvert\psi_4\rangle\right)$	0.32	0.32

Table 1.2.: *Graphene/MoS_2 standard parameters. Concurrence at the two nonequivalent Dirac points for each of the four eigenstates, where can be present in some degree a entanglement between spin-and pseudospin.*

b) Second condition $\lambda_I^A = \lambda_I^B$, and $\lambda_{PIA}^A = \lambda_{PIA}^B$:

Concurrence	K_-	K_+
$C\left(\|\psi_1\rangle\right)$	0.45	0.45
$C\left(\|\psi_2\rangle\right)$	0.10	0.10
$C\left(\|\psi_3\rangle\right)$	0.45	0.45
$C\left(\|\psi_4\rangle\right)$	0.10	0.10

Table 1.3.: *Graphene/MoS_2 second condition. Concurrence at the two nonequivalent Dirac points for each of the four eigenstates, where can be present in some degree a entanglement between spin-and pseudospin.*

a) Standard parameters considering all terms presented in Table 1.1:

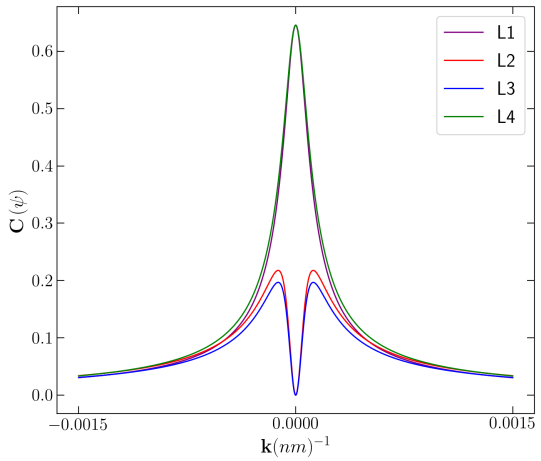

Figure 1.18.: *Zoom at Dirac point of each value of concurrence for the four band graphene/$MoSe_2$for standard parameters.*

Concurrence	K_-	K_+
$C\left(\|\psi_1\rangle\right)$	0.65	0.65
$C\left(\|\psi_2\rangle\right)$	0.01	0.01
$C\left(\|\psi_3\rangle\right)$	0.01	0.01
$C\left(\|\psi_4\rangle\right)$	0.65	0.65

Table 1.4.: *Graphene/$MoSe_2$ standard parameters. Concurrence at the two nonequivalent Dirac points for each of the four eigenstates, where can be present in some degree a entanglement between spin-and pseudospin.*

b) Second condition $\lambda_I^A = \lambda_I^B$, and $\lambda_{PIA}^A = \lambda_{PIA}^B$:

Concurrence	K_-	K_+
$C\left(\|\psi_1\rangle\right)$	0.78	0.78
$C\left(\|\psi_2\rangle\right)$	0.10	0.10
$C\left(\|\psi_3\rangle\right)$	0.78	0.78
$C\left(\|\psi_4\rangle\right)$	0.13	0.13

Table 1.5.: *Graphene/$MoSe_2$ second condition. Concurrence vs. k-path, where is point outed the two inequivalent Dirac points where can be present in some degree a entanglement between spin-and pseudospin.*

a) Standard parameters considering all terms presented in Table 1.1:

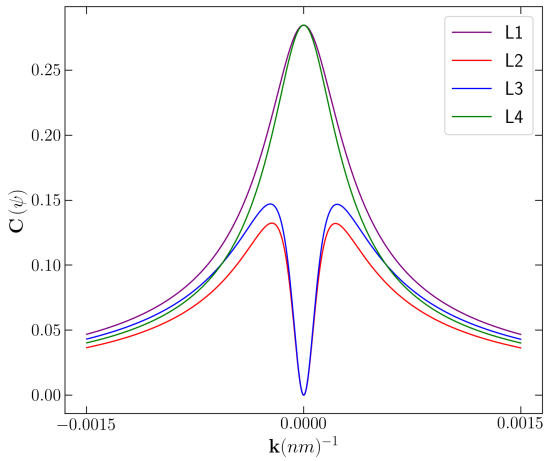

Figure 1.19.: *Zoom at Dirac point of each value of concurrence for the four band graphene/$WS_2$for standard parameters.*

Concurrence	K_-	K_+
$C\left(\|\psi_1\rangle\right)$	0.27	0.27
$C\left(\|\psi_2\rangle\right)$	0.16	0.16
$C\left(\|\psi_3\rangle\right)$	0.16	0.16
$C\left(\|\psi_4\rangle\right)$	0.27	0.27

Table 1.6.: *Graphene/WS_2 standard parameters. Concurrence at the two nonequivalent Dirac points for each of the four eigenstates, where can be present in some degree a entanglement between spin-and pseudospin.*

b) Second condition $\lambda_I^A = \lambda_I^B$, and $\lambda_{PIA}^A = \lambda_{PIA}^B$:

Concurrence	K_-	K_+
$C\left(\|\psi_1\rangle\right)$	0.49	0.49
$C\left(\|\psi_2\rangle\right)$	0.20	0.20
$C\left(\|\psi_3\rangle\right)$	0.49	0.49
$C\left(\|\psi_4\rangle\right)$	0.10	0.10

Table 1.7.: *Graphene/WS_2 second condition. Concurrence at the two nonequivalent Dirac points for each of the four eigenstates, where can be present in some degree a entanglement between spin-and pseudospin.*

a) Standard parameters considering all terms presented in Table 1.1:

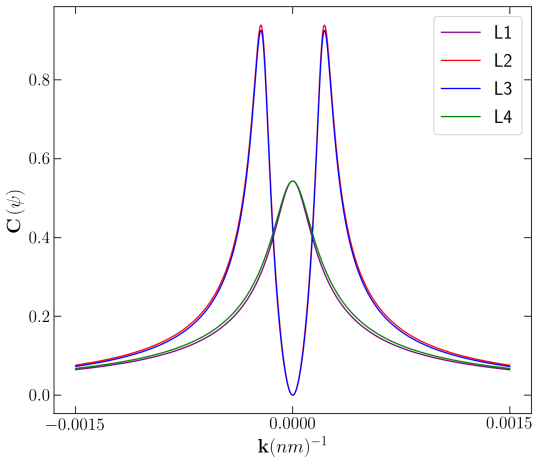

Figure 1.20.: *Zoom at Dirac point of each value of concurrence for the four band graphene/$WSe_2$for standard parameters.*

Concurrence	K_-	K_+
$C\left(\|\psi_1\rangle\right)$	0.88	0.88
$C\left(\|\psi_2\rangle\right)$	0.88	0.88
$C\left(\|\psi_3\rangle\right)$	0.58	0.58
$C\left(\|\psi_4\rangle\right)$	0.58	0.58

Table 1.8.: *Graphene/WSe_2 standard parameters. Concurrence at the two nonequivalent Dirac points for each of the four eigenstates, where can be present in some degree a entanglement between spin-and pseudospin.*

b) Second condition $\lambda_I^A = \lambda_I^B$, and $\lambda_{PIA}^A = \lambda_{PIA}^B$:

Concurrence	K_-	K_+
$C(\|\psi_1\rangle)$	0.88	0.88
$C(\|\psi_2\rangle)$	0.88	0.88
$C(\|\psi_3\rangle)$	0.58	0.58
$C(\|\psi_4\rangle)$	0.18	0.18

Table 1.9.: *Graphene/WSe_2 second condition. Concurrence at the two nonequivalent Dirac points for each of the four eigenstates, where can be present in some degree a entanglement between spin-and pseudospin.*

Analyzing the data available for the concurrence for each band structure of the graphene/tmdc's platforms, we can conclude:

- By setting $\lambda_I^A = \lambda_I^B$, we turning off valley - Zeeman, and this results in a change of the concurrence values.
- For standard values of valley-Zeeman presented in the first table of this section, we can conclude that the amount of entanglement in these systems are graphene/WSe_2 >graphene/$MoSe_2$ > graphene/MoS_2 > graphene/WS_2.
- Considering the second condition where we have $\lambda_I^A = \lambda_I^B$, and $\lambda_{PIA}^A = \lambda_{PIA}^B$, the amount of entanglement increase in all the cases,as presented in the data in the respective tables above, thus, graphene/WSe_2 >graphene/$MoSe_2$ >graphene/WS_2 > graphene/MoS_2 .
- The previous sentence implies that valley-Zeeman (**VZ**) tends to suppress the overall concurrence of the eigenstates. It suggest that only Rashba **SOC** is responsible for maximize the concurrence, but not **VZ**.
- In general, we also can generate a reasonable amount from entanglement if we inject an Haar pure initial state to any of these systems studied in this section. With this, we have similar results that we obtained in the section 1.3 regarding the generation of entanglement from an non-entangled initial state.

1.5. Discussions

In this chapter, we have presented the main results which are publishes regarding the origin and formation of spin-pseudospin intra-particle entanglement in graphene

clean, see section 1.3. Also we presented some other outcomes in the section 1.4, considering graphene on a substract, we can have the same good results regarding the generation of Bell pairs without a initial entangled state, when we are considering the dynamics of entanglement.

We have shown in our work (see Ref. [128]) that:

1. Intra-particle entanglement in graphene is a complex dynamic quantity, governed by the mutual precession of spin and pseudospin.

2. For an arbitrary initial state the average entanglement is large, with a concurrence of 0.5–0.6 that corresponds to a 10–16% maximal violation of the CHSH inequality.

3. Spin-pseudospin dynamics enable the generation of entanglement in electrons that are initially separable. This suggests that intra-particle entanglement in graphene may be robust to disorder and dephasing; after an entanglement-destroying interaction, spin and pseudospin dynamics will lead to re-generation of the intra-particle entanglement of a particular electron.

4. Going beyond the single-particle picture, these results may also have important implications for inter-particle entanglement between pairs of electrons in graphene. For example, it was shown that the dynamics of intra-particle entanglement can have a significant impact on inter-particle entanglement, including transfer from one type of entanglement to another [26]. Such behavior is also expected to occur in the graphene-Rashba system, and is an interesting path for future exploration.

5. In graphene/TMDC's systems, there are some SOC terms that suppressing the entanglement.

Part II.

Local measurements in finite lattices

2. Local quantum overlapping tomography (LQOT)

*Most of the content of this chapter is presented in the collaborative paper: "**Local quantum overlapping tomography**", available as preprint: 2112.03924 [quant-ph], by Bruna G. M. Araújo, Márcio M. Taddei, Daniel Cavalcanti and Antonio Acín, and **"Adiabatic quantum algorithm for artificial graphene",** available as preprint: 2204.03013 [quant-ph], by Axel Pérez-Obiol, Adrián Pérez-Salinas, Sergio Sánchez-Ramírez, Bruna G. M. Araújo, Artur Garcia-Saez.*

2.1. Introduction

There have been great advances in the construction of quantum devices, with systems composed of tens of individually addressable qubits [134, 135, 136, 137, 138], more than a hundred bosonic modes [139, 140], or intermediate-scale systems of up to thousands of entangled qubits [141, 142], with further advances clearly on the way. These are based on several different physical systems, such as trapped-ion spins, superconductors or photons. These developments bring to the fore the problem of efficiently measuring a quantum system. A full description of a system of size n requires an amount of parameters exponential in n, and likewise full quantum state tomography requires an exponential amount of resources (e.g. measurement settings, outcomes), a feat that has been achieved so far for a maximum of 10 qubits [143].

Several approaches have been presented to circumvent the problem and reconstruct the quantum state with fewer measurements, hence fewer produced copies of the state to be measured. Some assume an *a priori* structure of the measured states, such as classes including matrix-product states [144, 145], or require certain structures for efficient measurement [146, 147, 148]. The "shadow tomography" technique [149, 150] is not at its most efficient when reconstructing quantum states, and additionally requires a quantum memory to store several copies of the state and act collectively on them [151], or else its advantage is lost [152].

A less ambitious, but possibly more realistic approach is to focus not on the entire quantum state but on some of its properties of interest. A natural example is that where one is interested in estimating its k-body reduced density matrices (k-RDMs). It is not uncommon for there to be interest in k-body operators, e.g. to detect the entanglement [153, 154] or Bell non-locality [155] of the many-body state from the expectation values of 2-body operators. A direct approach consists of measuring each k-RDM independently. Therefore, qubits or fermions come from various quantum systems that cover *interacting electronic spins, quantize fluxes, spatial modes, and quantum chemistry electronic systems.* We can start our definition of the main topic of this chapter with this simple question:

How can we extract the information from these systems and organize the data about the entanglement?

Thus, starting from an unknown state formed by n-qubits or n-fermions, we must do many measurements that grow with the system's size to characterize them via quantum tomography fully. This exponential growth becomes the quantum tomography for many-body states non-feasible in practical terms, even for simple techniques in terms of complexity. We have a massive gap between the production of entangled states in controlled conditions and our capability to characterize entanglement quantitatively. One way to try to mitigate this issue is to address individually the qubits or fermions of a system taking advantage of the parallelism.

Let's start with our discussion about qubits. Initially, we need to measure all k-qubits contained in a system of n-qubits, being $n > k$. If we have access to these reduced matrices by chance, we could characterize the entanglement of our n-qubit system. Supposing that we have $\begin{pmatrix} n \\ k \end{pmatrix}$ where $k \ll n$ we have that $\begin{pmatrix} n \\ k \end{pmatrix} \sim n^k$, and $e^{O(k)}$ measurements, thus, are required approximately $e^{O(k)}n^k$ measurements to obtain all k-qubit reduced matrices. This way, even if we consider a two-point correlation function with a relatively small number of qubits, we will need hundreds of measurements, which is not practical. This estimation ignores the parallelism resource. If we measure these non-overlapping qubits in parallel, the number of measurements is reduced by the n/k rate. However, the measurement scaling is still high, so we will use the strategy to estimate the reduced matrices of the overlapping qubits. Therefore, we must obtain an efficient strategy to perform partial quantum tomography. Thus, combining the parallelism and highly overlapping qubits gives a technique for performing partial quantum tomography called ***"quantum***

overlapping tomography" (**QOT**). Which will be the central merit figure in this chapter.

Using QOT principles, we can organize the data via 1D partition, which is a bit less efficient and by 2-D partition, properly building harsh functions for n and k. The QOT protocol for free qubits only requires measuring each entity in parallel and on a distinct basis denominated X, Y, or Z, which form a product of measurements. The measurements could be post-processed to reconstruct all k-qubit reduced matrices required to get the local physical observable [156, 157]. Target obtaining every k-RDM of an n-partite system. However, there are often cases where specific subsets are especially relevant and others less so. The most typical example is when there is a spatial distribution (e.g., a lattice) with local interactions expected to play an important role: RDMs containing neighboring subsystems are much more critical than those having faraway ones.

The main goal of this chapter is *to provide efficient strategies to measure these reduced states by means of products of local measurements*, as in overlapping tomography. Our first result is to show that this form of *local overlapping tomography* produces a much more dramatic reduction in complexity: while the naive approach in which full tomography is performed for all reduced states of interest requires a number of measurements that grows with the number of reduced states, and hence with the system size, an efficient parallelization can do away with the system-size dependence. After presenting this general result, we provide finer measurement strategies for finite-dimensional and fermionic systems in well-known lattice geometries.

This chapter is structured as follows:

- In **Sec. 2.2**, we present existing results and set the notation.
- In **Sec. 2.3** we present our main results, first in the form of a general argument valid for systems of arbitrary finite dimension, then for qubits (**Subsec. 2.3.1**) and lastly for fermions (**Subsec. 2.3.2**).
- In **Sec. 2.4** we present an application of the methodologies studied in this chapter as a building block of an algorithm to simulate a model of artificial graphene.
- In **Sec. 2.5** we make our concluding remarks and future prospects.

2.2. Preliminaries

2.2.1. Introduction to quantum measurements

The scope of this section is to explain how measurement processes are described in quantum theory. Thus, we need to point out that there are two kinds of measurements that would be useful to understand the main results, they are:

1. **P*rojective measurements:*** described by a orthogonal basis $|u_1\rangle, \cdots, |u_d\rangle \epsilon \mathbb{C}^d$ which correspond to the measurement outcomes. When the measurement is performed on a pure state $|\psi\rangle \epsilon \mathbb{C}^d$, outcome $i \epsilon [d]$ is obtained with probability $|\langle u_i| \psi\rangle|^2$, and $|\psi\rangle$ collapses to the state $|u_i\rangle$. If the inital state is mixed described by $\rho \epsilon \mathcal{B}(^d)$, them outcome i is observed with probability $\langle u_i| \rho |u_i\rangle$ and state ρ collapses to $|u_i\rangle \langle u_i|$. Give us a set of orthogonal projectors matrices $\Pi_i, \cdots, \Pi_m \epsilon \mathcal{B}(^d)$ which obey the "completeness condition" $\Pi_1 + \cdots + \Pi_m = I$. If a measurement is performed on a pure state $|\psi\rangle$, outcome $i \epsilon [m]$ is observed with probability $\langle\psi| \Pi_i |\psi\rangle$, in which case $|\psi\rangle$ collapses to

$$\frac{\Pi_i |\psi\rangle}{|\Pi_i |\psi\rangle|}, \tag{2.1}$$

where $|\Pi_i |\psi\rangle|$ denotes the norm of the state $\Pi_i |\psi\rangle$. If we consider the same process on a mixed state ρ, outcome $i \epsilon [m]$ is observed with probability $\mathrm{tr}(\Pi_i \rho)$, in which case ρ collapses to

$$\frac{\Pi_i \rho \Pi_i}{tr\left(\Pi_i \rho\right)}, \tag{2.2}$$

2. ***General quantum measurements are described by positive-operator value measures (POVM),*** defined by a set of positive matrices $E_1, \cdots, E_m$ such that $E_1 + \cdots + E_m = I$. In the pure state case $|\psi\rangle$, outcome $i \epsilon [m]$ is observed with probability $tr\left(E_i |\psi\rangle \langle\psi|\right)$. For the case of the mixed state ρ, the probability of observation is $tr\left(E_i |\psi\rangle \langle\psi|\right)$. Projective measurements are a subset of general measurements in which **POVM** elements are defined by projectors, $E_i = \Pi_i$.

A pragmatic example of POVM is **a symmetric, informationally complete, positive operator-value measure (SIC-POVMs).** If a **POVM** has d^2 operators which span the space of self-adjoint operators $\mathcal{L}(H)$, it is said to be informationally

complete POVM (IC - POVM). IC-POVMs consisting of at least d^2 minimal elements. A set of d^2 rank-1 projectors, such as

$$\Pi = \left\{\Pi_i \mid i \quad \epsilon \quad \left\{1, \cdots, d^2\right\} \wedge \Pi_i^2 = \Pi_i\right\}, \tag{2.3}$$

which has inner product

$$tr\left(\Pi_i \Pi_j\right) = \frac{d\delta_{ij} + 1}{d+1}, \tag{2.4}$$

defines a minimal **IC-POVM**

$$F = \left\{F_i \mid i \quad \epsilon \quad \left\{1, \cdots, d^2\right\} \wedge F_i = \frac{1}{d}\Pi_i \wedge \Pi_i \quad \epsilon \quad \Pi\right\}, \tag{2.5}$$

called a **SIC-POVM**.

- Definition: For a system of N particles, there are three main classes of measurements with increasing complexity:

1. ***Non-adaptative measurements:*** We apply local measurements on each particle at once, the resulting measurement operators being the tensor product of the measurement operators on each particle.

2. ***Adaptative measurement:***The measurements still act at a single-particle level, but measurements on the different particles are implemented in a sequential way, so that measurements on particle i may depend on the results of previous measurements implemented on particle $1, \ldots, i-1$.

3. ***Entangled measurement:*** We make a single joint (possibly entangled) measurement on all particles. It covers all previous cases.

We can also have hybrid situations. For instance, you measure half of the particles with local measurements (non-adaptative), and, depending on the results (adaptative), you perform a joint measurement (entangled) on the remaining half. In any case, the most general situation is given by definition 3 and cover all possible cases. That means that entangled measurements generalize adaptative measurements, which generalize non-adaptative measurements, in which one grows in complexity. *For our methodology of local overlapping tomography, we are considering* ***non-adaptative measurements***.

2.2.2. Concentration of measure

2.2.2.1. A general phenomenon

We can start illustrating the concept of concentration of measure through the most straightforward example from probability theory: coin tossing. Consider a fair coin. If we toss it once, the result is entirely unpredictable. It can be "tails" or "heads," each with 1/2 probability. If you throw the same fair coin a thousand times, the number of heads is "sharply predictable," probably around 500 for each face of the coin.

Although there are many possible outcomes, those that can be observed are restricted to a small range set. This phenomenon shows up in vast forms in nature and is responsible for us having a successful prediction about our physical world. As we know in quantum mechanics, the dynamics of the particles follows probabilistic laws.

Due to the great importance of this phenomenon for modern probability theory, a considerable part of this field is devoted to its study. The laws of large numbers and the central limit theorem are well-known examples.

On the other hand, our motivation is to study the problem: Suppose we have a random variable X with mean $E[X]$. Usually, we want to know how close X is to its mean $E[X]$ with accurate probability. The results regarding this simple question are called concentration inequalities.

We need uniform bounds that a set of random variables are close to their mean and with a high probability value. In other words, we want to understand under what conditions the random variable X has large deviations from the mean unlikely.

Besides the simple example of coin tossing, this phenomenon is quite common in our physical world, including in the object of interest of this chapter. Here, we can enumerate some reasons why classical results are unsuitable to describe these kinds of phenomena aforementioned that would be useful for our problem.

- Usually probability theory consider the asymptotic limit, but for infinite systems, and in most cases in nature, we need to consider ***finite systems***.

- Knowing that classical probability theory has a qualitative approach deal with the problems considering a convergence limit but does not provide its rate. Thus, for our class of problems, we need to treat them quantitatively, providing a rate of convergences or even very good bounds.

In the following subsection, we will formalize the primary tool describing the concentration of measure for our system.

2.2.2.2. Relevant bounds

Chernoff-Hoeffding bound

This tool is a simple and powerful technique frequently used to establish bounds in the probability functions whose sum of the random variables is considered bounded. Usually, this happens when we are dealing with a considerable amount of data.

Thus, the easier way to tackle this is by reducing it in the sets via a random process. In other words, we must execute many repeated simple estimations of the entire data. We can obtain an accurate and small representation of this large amount of data through this simple estimation. Thus, the main goal in using this tool is to know how many of these estimations are required for a given accuracy [158, 159].

Theorem 1: Suppose we have a set r of independent random variables $\{X_1, \cdots, X_r\}$, with $a_i \leqslant X_i \leq b_i$, being $\Delta_i = b_i - a_i$, we consider $M = \sum_{i=0}^{r} X_i$.

For any $\alpha \quad \epsilon \quad (0, 1/2)$, we have:

$$P_r\left[|M - E\left[M\right]| > \alpha\right] \leq 2\exp\left(\frac{-2\alpha^2}{\sum_{i=1}^{r} \Delta_i^2}\right). \tag{2.6}$$

Thus, we need to connect this to the concept of the union bound.

Union bound

As showed in Fig. 2.1, consider $n = 2$ events. We have

$$\begin{aligned} \mathbb{P}\left(A \cup B\right) &= \mathbb{P}\left(A\right) + \mathbb{P}\left(B\right) - \mathbb{P}\left(A \cap B\right), \\ &\leq \mathbb{P}\left(A\right) + \mathbb{P}\left(B\right), \end{aligned} \tag{2.7}$$

because $\mathbb{P}\left(A \cap B\right) \geq 0$. By inductive hypothesis, we suppose it is true that for n random events $X_1, \cdots, X_n$,

$$\mathbb{P}\left(X_1 \cup \cdots \cup X_n\right) \leq \sum_{i=1}^{n} \mathbb{P}\left(X_i\right) \tag{2.8}$$

For $n+1$, we have:

$$\begin{aligned}\mathbb{P}\left(X_1 \cup \cdots \cup X_n \cup X_{n+1}\right) &= \mathbb{P}\left(\left(X_1 \cup \cdots \cup X_n\right) \cup X_{n+1}\right) \\ &= \mathbb{P}\left(X_1 \cup \cdots \cup X_n\right) + \mathbb{P}\left(X_{n+1}\right) \\ &\leq \sum_{i=1}^{n} \mathbb{P}\left(X_i\right) + \mathbb{P}\left(X_{n+1}\right) \\ &= \sum_{i=1}^{n+1} \mathbb{P}\left(X_i\right).\end{aligned} \tag{2.9}$$

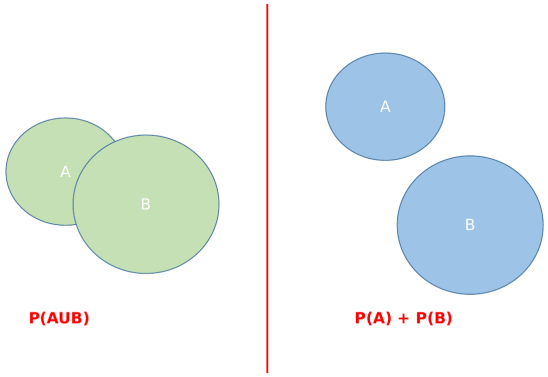

Figure 2.1.: *Events A and B, expression of the union bound.*

With this induction proof, we have a bound that applied to union of various events can provide a robust tool for many applications whenever the individual probability is smaller to the probabilities of the number of events. Applying basic rules of probability theory, we can rewrite the expression for union bound in the Eq. (2.8) for the case that the probability of the intersection of the events does not occurs, thus, we have

$$1 - \mathbb{P}\left(\bigcap_{i=1}^{n} X_i\right) \leq \sum_{i=1}^{n} \mathbb{P}\left(X_i\right). \tag{2.10}$$

2.2.2.3. Number of repetitions

Here we prove some relations on the number of repetitions M needed for statistical purposes based on the Chernoff-Hoefding bound, as in [156]. Consider that M

measurements are made, and that each measurement has ± 1 as possible outcomes. Then the Chernoff-Hoefding bound states that the probability of error obeys

$$P(\text{error}_i > \varepsilon) \leqslant 2e^{-M\varepsilon^2/2} \ , \tag{2.11}$$

where error_i is defined as the difference in modulus between the expectation value of the i-th variable and its estimate (arithmetic mean of M measured values). In other words, it states that the probability of error greater than ε is exponentially suppressed. The union bound can then be used to bound the probability of high error in any of the variables:

$$P(\text{error}_i > \varepsilon \text{ for any } i) \leqslant \sum_i 2e^{-M\varepsilon^2/2} \ , \tag{2.12}$$

where the sum in i runs over all measured variables.

2.2.3. Quantum State tomography

This section describes the quantum state tomography (**QST**) protocol based on the standard experimental approach where the protocols require the product of measurements where each qubit is measured independently. To start to discuss **QST**, we will focus our discussion on a single qubit state and with a simple question:

How can we experimentally characterize a quantum state ρ?

Following what we have discussed about the concentration of measurements and the bounds, it is evident that with a single copy of a quantum state ρ is impossible to have reliable information about a state because no quantum measurement can distinguish two different non-orthogonal states such as $|1\rangle$ and $(|0\rangle + |1\rangle)/\sqrt{2}$ with certainty. But, if we have many copies of ρ, we can build enough statistics. In other words, we need to repeat a quantum experiment many times to estimate the state ρ.

In this scenario, consider we have many copies of a single quantum state, knowing that $tr\,(O\rho)$ can be interpreted by the average of an observable O, and being σ_i^α describing a Pauli operator on the i-th site, $i = 1, ..., N$ and $\alpha = 0, 1, 2, 3$ where $\sigma^0 = \mathbf{1}$, $\sigma^1 = \sigma^x$,$\sigma^2 = \sigma^y$ and $\sigma^3 = \sigma^z$, at the moment we are considering only one

site. We can expand the representation of the single state as

$$\rho = \frac{tr\left(\mathbf{1}\rho\right)\mathbf{1} + tr\left(\sigma^{x}\rho\right)\sigma^{x} + tr\left(\sigma^{y}\rho\right)\sigma^{y} + tr\left(\sigma^{z}\rho\right)\sigma^{z}}{2}. \tag{2.13}$$

Now, to estimate the expectation value $tr\left(\sigma^{x}\rho\right)$ of the σ^{x} observable, we measure it M times, obtaining the outcomes $x_1, x_2, \cdots, x_m$, the empirical average of σ^{x} is given by

$$tr\left(\sigma^{x}\rho\right) \approx \frac{1}{M}\sum_{i=1}^{N} x_i, \tag{2.14}$$

with standard deviation $\Delta\left(x\right)/\sqrt{M}$. Therefore, we can estimate the quantities $tr\left(\sigma^{y}\rho\right)$, $tr\left(\sigma^{z}\rho\right)$ in similar way with high degree of confidence in the large number limit. We can generalize this protocol to N qubits, using that any n-qubit state can be written as

$$\rho^{'} = \sum_{i_1,\ldots,i_k=0}^{3} tr\left\{\left(\sigma_1^{i_1}\otimes\ldots\otimes\sigma_n^{i_n}\right)\rho^{'}\right\}\sigma_1^{i_1}\otimes\ldots\otimes\sigma_n^{i_n}, \tag{2.15}$$

For full quantum tomography, we need to estimate $M\left(4^{N}-1\right)$ expectation values for obtaining an N qubits density matrix. For partial quantum state tomography, where we consider a k-qubits subset contained in the N qubits set, we need to measure $3^{k}M$ product of measurements to obtain a k-qubits reduced density matrix.

2.2.4. Overlapping quantum tomography

The goal of this section is to introduce overlapping quantum tomography, a measurement strategy to estimate the k - RDM of many - body quantum systems. To enhance our motivation, we can start with the question:

Why do we need to get k-RDMs?

In many physical systems k-RDMs contain enough information for reconstructing relevant physical quantities. For instance, in quantum chemistry, fermionic k-RDM allow one to estimate the *energy, change density and energy gradients observables of electronic systems.* For example, the qubit k- RDMs are suitable for obtaining information about *spatial correlations* in magnetic systems.

If we restrict our considerations to measurements consisting of products of single-particle projective measurements for their experimental feasibility, this already produces a significant reduction of measurements compared to full tomography: the latter requires $\mathcal{O}(e^n)$ measurements, while each k-RDM requires $\mathcal{O}(e^k)$ measurements, hence the complete set of k-RDMs, $\mathcal{O}(e^k \binom{n}{k}) \sim \mathcal{O}(n^k/k^k)$ measurements.

However, existing techniques [160, 157, 161, 156, 162, 163, 164, 165] based on parallelization can reduce that amount substantially. These techniques make use of the fact that from single N-body measurements one can extract different parameters relevant for the computation of more than one k-RDM. The simplest example is given by the situation in which a single measurement, say X, is implemented on all particles, from which all two-body $< X_i X_j >$ and one-body $< X_i >$ can be obtained. These measurement strategies are sometimes known as overlapping tomography. For a system of n qubits, the technique in [157] uses at most $\mathcal{O}(e^k \log^{k-1} n)$ measurements to obtain all k-RDMs, and the one in [161] obtains a constant-factor reduction of the latter for $k = 2$; in [156] it is shown that $e^{\mathcal{O}(k)} \log n$ unique measurements suffice; from [162] it follows that $\mathcal{O}(3^k) \log n$ *total* measurements suffice.

For systems of fermions, the $\binom{2n}{2k}$ operators needed can be measured [157, 163] with $\mathcal{O}(n^2)$ measurements if $k = 2$, and for any k there are schemes [164] with $\mathcal{O}(n^k)$ or, even better, $\mathcal{O}(\binom{n}{k})$ measurements [165]. It is noticeable that restrictions to parallelism from fermionic anticommutation relations negatively impact the reduction of complexity. To the best of our understanding, none of these results is known to be tight.

2.2.4.1. Qubits

If ρ is an n-qubit state, any state obtained by taking the partial trace with respect to a set of $n - k$ qubits is a k-RDM of ρ. It is possible to reconstruct such k-RDMs from the expectation values of products of Pauli matrices. Consider as an example the k-RDM of the first k qubits, ${}_{[n]\setminus[k]}(\rho)$, where we define $[j] := \{0, 1, \cdots, j-1\}$. The set of expectation values of the form $\langle \sigma_{a_0}^{(0)} \otimes \cdots \otimes \sigma_{a_j}^{(j)} \otimes \cdots \otimes \sigma_{a_{k-1}}^{(k-1)} \rangle$ clearly suffices to characterize this k-RDM if $\sigma_{a_j}^{(j)}$ can be either the identity or one of the Pauli matrices σ_x, σ_y, σ_z of the j-th qubit.

However, this can be simplified by the fact that the algorithms in question are based on making local measurements with access to each local outcome. In this setting, any measurement that includes an identity can be simulated by taking the suitable marginal of a measurement with a Pauli matrix in its place.

For a system of n qubits, several works have tackled the issue of obtaining all $\binom{n}{k}$ existing k-RDMs with as few different measurements as possible through

parallelization. For 2-RDM, Refs. [156, 157, 161] have obtained $\langle \sigma_a^{(i)} \otimes \sigma_b^{(j)} \rangle$ for all pairs of qubits (i, j) and a, b covering all combinations of σ_x, σ_y, σ_z. Refs. [157] and [156] present schemes with $N = 3 + 6\lceil \log_2 n \rceil$ measurements based on partitioning and a family of hash functions $(n, 2)$, respectively; [161] reduces that scaling to $N = 3 + 6\lceil \log_3 n \rceil$.

The first two allow for generalizations to $k > 2$: [157] presents a scheme based on recursive partitioning with $N = \mathcal{O}(3^k \log_2^{k-1} n)$ measurements; [156] reduces the problem to finding hash functions (n, k), yielding $N = e^{\mathcal{O}(k)} \log_2 n$ measurements (see Section 2.2.5 for a further result).

All these results target the obtention of all k-RDMs, regardless of any structure. As mentioned, we follow here a different approach, where the RDMs of interest are those of neighboring sites on a lattice. Many relevant systems, such as ion traps [141, 166], quantum-dot lattices [167], semiconductor lattices [168], among others, work based on local interactions with neighbors (first or beyond), and would benefit from a measurement scheme focused on them.

2.2.4.2. Fermions

In addition to qubits, we also tackle the efficient measurement of systems composed of fermions. Fermionic systems present a much greater challenge than qubits. Because of their anticommutation relations, operators on different lattice sites may no longer commute, hence one cannot rely on tensor-product relations to ensure jointly measurability, as in qubits.

In a fermionic system of n modes with m particles ($n \geqslant m$), the k-RDM is given by tracing out $(m - k)$ particles, ${}_{[m-k]}(\rho)$, with the difference that any set of $(m - k)$ particles is equivalent, due to symmetry. Each mode i has an annihilation (a_i) and a creation $(a_i^\dagger)$ operator, and to obtain ${}_{[m-k]}(\rho)$ it suffices [169] to obtain the expectation values of operators composed of k creation and k annihilation operators.

For the 1-RDM, for instance, the values of $\langle a_i^\dagger a_j \rangle$ for all modes i, j suffice. It will be convenient, however, to work with Majorana operators [170, 171, 172], which offer an equivalent description of fermionic systems,

$$\gamma_{2j} := a_j^\dagger + a_j \ , \qquad \gamma_{2j+1} := i(a_j^\dagger - a_j) \ . \tag{2.16}$$

Majorana operators (Majoranas, for short) are Hermitian with ± 1 eigenvalues and have an important role in the (partial) equivalence between fermions and qubits [173, 170, 174]. The k-RDM of a given system requires all expectation values

$\langle \gamma_p \gamma_q \cdots \gamma_r \gamma_s \rangle$ composed of $2k$ Majoranas, e.g. $\langle \gamma_p \gamma_q \rangle$ for all p, q for the 1-RDM.

Of utmost relevance for parallelization is that different Majoranas all anticommute, a marked difference to qubits. Once again, the existing literature tackles the obtention of all $\langle \gamma_p \gamma_q \cdots \gamma_r \gamma_s \rangle$ for a given value k.

By appropriately pairing Majoranas, Ref. [157] obtains the so-called "cliques" composed of commuting multiple-Majorana operators. As all operators in a clique are Hermitian and commute, they can be determined by a single measurement, hence only one measurement is required per clique.

There are established routines to perform such measurements, typically with fermion-to-qubit mappings [164, 165].

For the 1-RDM, the authors of [157] present a scheme to cover all needed Majorana operators with $2n - 1$ commuting cliques ($N = 2n - 1$) and for the 2-RDM, with $(10/3)n^2 + \mathcal{O}(n)$ commuting cliques.

A general lower bound of $N = \binom{2n}{2k} / \binom{n}{k}$ on the needed number of cliques (hence, of measurements) is also shown in [157]; for the 1-RDM it is saturated by their scheme, $\binom{2n}{2} / \binom{n}{1} = 2n - 1$, whereas for the 2-RDM the bound is below their scheme by a prefactor in the leading-order term, $\binom{2n}{4} / \binom{n}{2} = (4/3)n^2 + \mathcal{O}(n)$.

In contrast, here we consider fermions in a lattice [175, 176, 168, 167, 177]; to each lattice site j belong two Majorana operators, as in Eq. (2.16). Given the spatial structure of the lattice, we tackle measurements of neighbors only, e.g. terms such as $\langle \gamma_i \gamma_j \rangle$ where γ_i, γ_j belong to neighbor sites.

Even though this is not sufficient to fully obtain a k-RDM, there is a great interest in efficiently obtaining such expectation values, which are relevant to survey quantities that hinge on groups of close neighbors, like coupling energies. Naturally, by focusing on a smaller subset of modes, the scaling of the number of measurements drastically reduces.

In table 2.1, we resume the main existing results on partial tomography together with the corresponding reference.

Method	Particles		k - subset		Nº of particles	Scaling	
	Qubits	Fermions	Qubits	Fermions		Qubits	Fermions
Pairwise networks	True	False	k=2	False	N	$3+6\lceil\log_3(N)\rceil$	x
QOT via Hash functions	True	False	k=2	False	N	$3+6\lceil\log_2(N)\rceil$	x
			k*			$\sim e^{O(k)}\log_2^2(N)$	
QOT via 1-D partition	True	True	k	k=1	N	$3+6\lceil\log_2(N)\rceil$	$2N-1$
				k=2		$\mathcal{O}\left(3^k\log_2^{k-1}N\right)$	$\sim\frac{10}{3}N^2$
Fermionic PT via classical shadow	False	True	False	k	N>>k	x	$\mathcal{O}\left(N^k\right)$

Table 2.1.: *Some efficient methods for partial quantum tomography.* ***First row:*** *partial quantum tomography for qubits based in pairwise networks see Ref. [161].* ***Second row:*** *quantum overlapping tomography (partial quantum tomography) based in Hash function for qubits. Explicit construction for k= 2 and for any k* was estimated the scaling but not explicitly obtained a quantum tomography. See Ref. [156] .* ***Third row:*** *quantum overlapping tomography explicity contruction for any k, N qubits and for 1 and 2- fermionic RDMs via 1D partition. More details in the Ref. [157].* ***Fourth row:*** *fermionic partial tomography via classical shadow for k and N fermions, being N very large. While the three first methods are deterministic this uses randomized measurement schemes. See Ref. [165].*

2.2.5. Total number of repetitions

The results summarized above concern the count N of unique measurements, e.g. the count of on how many different Pauli bases one must measure. The actual number of measurement rounds is NM, M being the number of repetitions needed for accurate statistics. The full k-RDM considered in [156] requires measuring 4^k-1 variables of each of the $\binom{n}{k}$ sets of k qubits, or $(4^k-1)\binom{n}{k}$ variables total. So for the full k-RDM,

$$P(\text{error}_i > \varepsilon \text{ for any } i) \leqslant 2(4^k-1)\binom{n}{k}e^{-M\varepsilon^2/2}\ , \tag{2.17}$$

where error_i is defined as the difference in modulus between the expectation value of the i-th variable and its estimate (arithmetic mean of M measured values). For that

probability to be smaller than a small value δ we can set

$$M \sim \frac{2}{\varepsilon^2}\left(k \log n + \log \frac{1}{\delta}\right) \quad \text{(full } k\text{-RDM)}. \tag{2.18}$$

In our case, we do not measure all $\binom{n}{k}$ sets of k qubits, only $\mathcal{O}(n)$ of them. We can then set

$$M \sim \frac{2}{\varepsilon^2}\left(k + \log n + \log \frac{1}{\delta}\right) \quad \text{(neighbors only)}. \tag{2.19}$$

For fermions, there are instead $\binom{2n}{2k}$ variables total in the full k-RDM, and still $\mathcal{O}(n)$ for our local k-RDMs, and the last two equations still stand. Using the **Chernoff-Hoefding bound**, the reasoning from [156] can show that $M \sim \frac{2}{\varepsilon^2}[k \log n + \log(1/\delta)]$ repetitions suffice to measure a full set of k-RDMs such that, with probability at least $1 - \delta$, the error in every local measurement is at most ε. Adapting that calculation to our localized k-RDMs, we see that the number of repetitions M can be set at $M \sim \frac{2}{\varepsilon^2}[k + \log n + \log(1/\delta)]$.

In light of this distinction, the result in [Theorem 3] [162] can be properly appreciated. Applied to a k-RDM, it states that the total number of measurements NM scales as $NM \sim \frac{2}{\varepsilon^2} 3^k \log(3^k \binom{n}{k}) \sim \frac{2}{\varepsilon^2}\mathcal{O}(3^k) \log n$, lower than the literature results mentioned above, for which $NM \sim \log^2 n$ or higher.

For the remainder of this chapter, we will discuss the number N of unique measurements (referred to simply as "measurements"), with the number of repetitions M implicitly assumed.

2.3. Local quantum overlapping tomography: main result

Our main goal is to find descriptions of k-body subsystems with as few measurements as possible. Because we want to obtain practical schemes with experimental feasibility, we only consider measurements corresponding to products of projective local measurements.

This ***excludes entangling measurements***, notably harder to perform, as well as constructions defined by ***SIC-POVMs*** (symmetric, informationally complete positive operator-valued measures), which reduce the number of different measurements at the cost of a markedly higher complexity of the experimental setup [178, 179, 180].

Let us first review some existing results, and with it fix some relevant definitions and notation. In what follows, when considering finite-dimensional systems, we restrict our considerations to qubits, although most of our results can easily be generalised to arbitrary dimension.

As mentioned, we are interested in many-particle systems with a natural notion of locality or distance. The standard way of encapsulating this notion is through lattices, where each particle is located in a node of the lattice.

Therefore, the general question of efficient local overlapping tomography is to, out of an n-site lattice, obtain the RDMs of all sets of k neighboring sites arranged in a given shape (k-sets). As shown in previous results, full k-RDMs require a number N of measurements that grows with system size n.

However, when the target are the k-RDMs of neighboring lattice sites, there are efficient parallelization schemes that significantly reduce N to the point of removing the n-dependence altogether. Let us see how this can happen.

The amount of k-sets is $\mathcal{O}(n)$, as can be seen as follows. Firstly, it cannot be greater than n, since each k-set is defined by its first site ("first" according to any ordering, e.g., top to bottom, left to right, etc); with n sites total, the amount of k-sets can be no more than n. Secondly, there are cases where not every site is the "first site" of a k-set.

This is better seen with an example on the honeycomb lattice (Fig. 2.2) where the k-sets are its hexagons ($k = 6$): taking the topmost site of each hexagon as its "first", we see that half the sites are not the topmost site of any hexagon, and indeed there are only $n/2$ hexagons in this case. However, because of the repeating nature inherent of a lattice, this may only occur with a given fraction of all sites (1/2 in the example), and the $\mathcal{O}(n)$ amount of k-sets holds in general.

A brute-force approach would be to measure these sets independently. Complete information on one k-set requires $\mathcal{O}(e^k)$ measurements, to reach all $\mathcal{O}(n)$ k-sets, $N = \mathcal{O}(ne^k)$ measurements are needed. An appropriate tiling, however, reduces N. Any lattice presents an intrinsic tiling of its sites into minimal cells, but can also be tiled into larger cells each composed of several minimal cells. As such, it is always possible to embed each k-set shape in a cell.

A suitable form of tiling for our measurements is precisely one where each k-set shape fits in one cell, see Fig. 2.3 a). All such k-sets belonging to different cells can be measured simultaneously, consuming $\mathcal{O}(e^k)$ measurements. To cover the k-sets that overlap with the ones in the first measurements, one must displace the cells in the symmetry directions of the lattice, as in Fig. 2.3 b). This procedure will require at most $\mathcal{O}(k^3)$ displacements [see Figs. 2.3c) and 2.3 d); for surface lattices, at most

$\mathcal{O}(k^2)$; for linear ones, at most $\mathcal{O}(k)$], hence a total of $N = \mathcal{O}(k^3 e^k)$ measurements.

In conclusion, an appropriate tiling of the n-lattice allows to reduce the number of measurements to obtain its k-sets from $N = \mathcal{O}(ne^k)$ to at most $N = \mathcal{O}(e^k)$, independent of n. If a fixed number of rotations of the k-set is targeted, this simply incurs in constant-prefactor increase in the number of k-sets and of necessary cells [e.g. if rotations of the shape in Fig. 2.3 a) in 0^{o} 90^{o}, 180^{o}, and 270^{o} are targeted, this prefactor is 4].

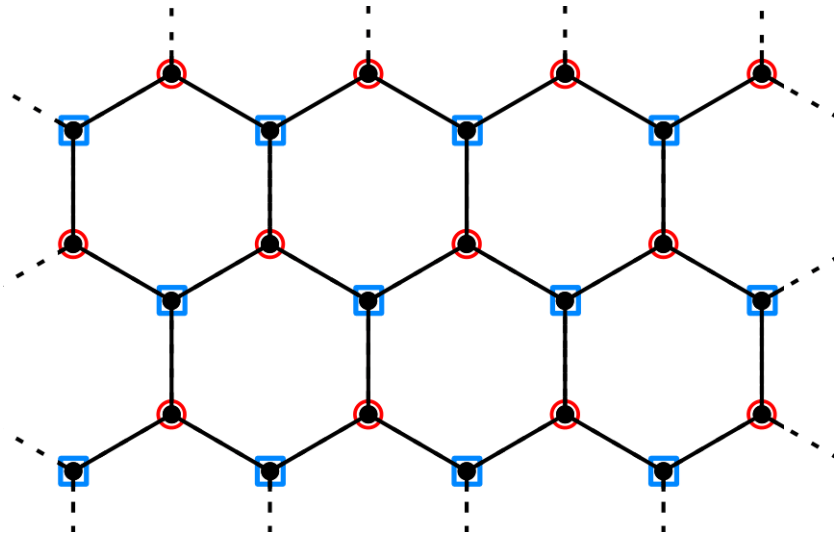

Figure 2.2.: *In an n-site honeycomb lattice there are $n/2$ hexagons, which can be identified by their topmost site (red circles). Half of all lattice sites are not the topmost site of any hexagon (blue squares). This figure was preprinted in Ref. [181].*

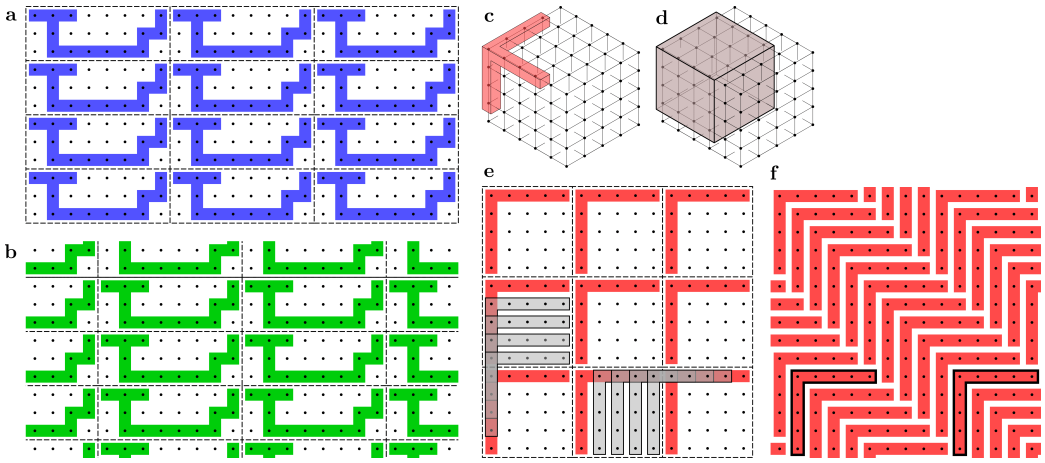

Figure 2.3.: *a) Tiling of an arbitrary shape by embedding in (non-minimal) lattice cells. The cells (dashed lines) are chosen as the smallest that contain the desired k-set (here $k = 13$). b) Example of displacement needed to cover k-sets overlapping with the ones on the original tiling. Here a displacement of 2 down and 4 to the right is shown; in total $8 \times 3 = 24$ displacements are needed [including the original tiling in a)]. At most k displacements in each direction are needed, so at most k^2 total for a planar lattice like above, k^3 for a three-dimensional lattice. c) Example of a k-set shape (here, $k = 10$) requiring $\mathcal{O}(k^3/3)$ displacements in the cubic lattice. d) Illustration of one cell for the scenario of c). e) Tiling of an L-shaped k-set with $k = 9$ by embedding in $\frac{k+1}{2}$-wide square cells. In red, the sets that fit the drawn cells; in gray some of the displaced L-shapes, $\frac{k+1}{2}$ down and $\frac{k+1}{2}$ to the right, a total of $(k+1)^2/4 = 25$ displacements (including the original). f) More efficient tiling of the same L-shapes. In this case only $k = 9$ displacements are necessary in total: a $(k+1)$-th displacement takes the pattern back to itself, as seen best by the black contoured shape on the left being displaced exactly onto the one on the right after $k+1$ steps. This figure was preprinted in Ref. [181].*

Given that the number of repetitions M in our case scales as $M \sim \frac{2}{\varepsilon^2}[k + \log n + \log(1/\delta)]$ (Section 2.2.5), a comparison with the result in [Theorem 3] [162] is in order. That theorem offers an algorithm to estimate the expectation value of m strings of k Pauli operators with $N \sim \mathcal{O}(e^k) \log m$ independent, randomly selected measurements, and without repetitions for statistics (effectively $M = 1$).

Applying it to a k-RDM on n qubits, one has $m = 3^k \binom{n}{k}$, hence $NM \sim \mathcal{O}(e^k) \log n$. We also obtain such scaling of NM, but with one difference: we have a lower number of different measurements $N \sim \mathcal{O}(e^k)$ (system-size independent), and a higher number $M \sim \log n$ of repetitions of those for statistics.

Notice that the form of embedding presented above is not necessarily optimal. Consider the L-shaped k-set in Fig. 2.3 e), with $(k+1)/2$-long arms. The tiling by

embedding described above would require $(k+1)/2$ displacements to the left and $(k+1)/2$ down, totaling $(k+1)^2/4 = \mathcal{O}(k^2)$ displacements of the original tiling.

A more efficient tiling is shown in Fig. 2.3 f), and requires only k displacements total. This tiling procedure demonstrates that the number of measurements in local overlapping tomography is independent of the system size. However, and because of its generality, it is typically sub-optimal for a given lattice. So we now turn to specific scenarios that are usually encountered in existing setups, and show more efficient measurement strategies for each of them.

2.3.1. Local qubit k-RDMs

The simplest case to consider is that of the 2-RDM for first neighbors. We need that, whenever i, j are neighbors, $\langle \sigma_a^{(i)} \otimes \sigma_b^{(j)} \rangle$ cover all combinations of (a, b). This reduces to the problem of vertex coloring of a graph: neighboring sites must be assigned different labels (colors), and from the number c of colors one obtains the number of measurements $N = 3^c$ (since each color has to cycle through x, y, z). Graph theory shows [182, 183] that for a graph of degree Δ (i.e. where a site has at most Δ first neighbors), it is always possible to color it with $\Delta + 1$ colors.

This gives an upper bound of $N \leqslant 3^{\Delta+1}$. Importantly, this graph-theory bound on c can be far from tight [182, eq. (1.2)], hence the same holds for the bound on N; better bounds can be written in terms of minimum degrees [183, Theorem 2.2]. Let us now focus on relevant geometries, in which we can obtain bounds that are tighter and hold beyond $k = 2$.

2.3.1.1. Strings, squares, cubes

We begin by the simplest lattice, a string of n qubits, whose results will serve as a building block for the others. The k-RDM of neighboring sites on a string are recovered from expectation values of the form

$$\langle \sigma_{a_i}^{(i)} \otimes \sigma_{a_{i+1}}^{(i+1)} \otimes \cdots \otimes \sigma_{a_{i+k-1}}^{(i+k-1)} \rangle \ . \tag{2.20}$$

The measurement scheme is defined using a single labeling $\boldsymbol{a}$ that cycles through a k-alphabet, or

$$a_i = i \bmod k \tag{2.21}$$

[see Fig.2.4a)]. It assigns measurements in each label that run independently through x, y, z, totaling $N = 3^k$ measurements. It is straightforward to see that in this scheme any k consecutive qubits have k different labels, and hence are measured in all combinations of the bases.

It is also clear that, for this or any other k-RDM, k is the minimum amount of labels needed: if $k-1$ or less labels were used, any group of k qubits would have coinciding labels, and the qubits assigned the same label would always be measured in the same basis, amounting to an incomplete measurement. Importantly, $N = 3^k$ does not scale with the system size n.

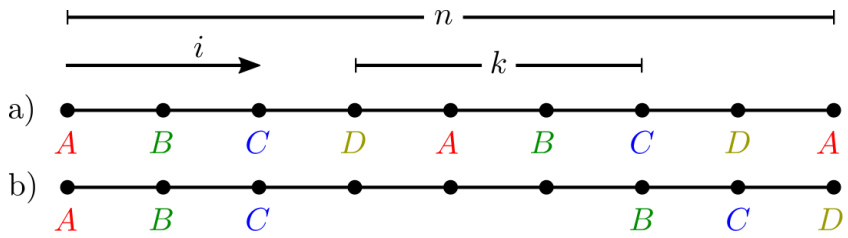

Figure 2.4.: *a) Labelings for string lattice [a)] and ring lattice [a) and b)] for $n = 9$, $k = 4$. For clarity, the numerical labels in the text have been converted to letters with the standard mapping $0 \to A$, $1 \to B$, $\cdots$, and also color-coded. This figure was preprinted in Ref. [181].*

Another one-dimensional lattice is the ring. A ring here is simply a string whose endpoints are considered first neighbors. A ring of qubits requires extra measurements, compared to the open string, when n is not divisible by k. A single extra labeling $\boldsymbol{b}$ is needed (assuming $n \geqslant 2k-2$); it labels the first $k-1$ qubits as before, the last $k-1$ qubits with the last $k-1$ letters of the k-alphabet, and the remaining qubits are not labeled (i.e. not measured). Formally,

$$b_i = \begin{cases} a_i \ , & \text{for } i \in [k-1] \\ a_{i-n} \ , & \text{for } i \in \text{last}_{k-1}[n] \\ \text{no label} & \text{otherwise} \ , \end{cases} \tag{2.22}$$

where $\text{last}_{k-1}[n] := [n] \backslash [n-(k-1)]$ and a_i obeys Eq. (2.21). This labeling is exemplified in Fig. 2.4 b). Notice that it correctly covers any set of k neighbors across the edge. With two labelings, the number of measurements rises to $N = 2 \times 3^k$.

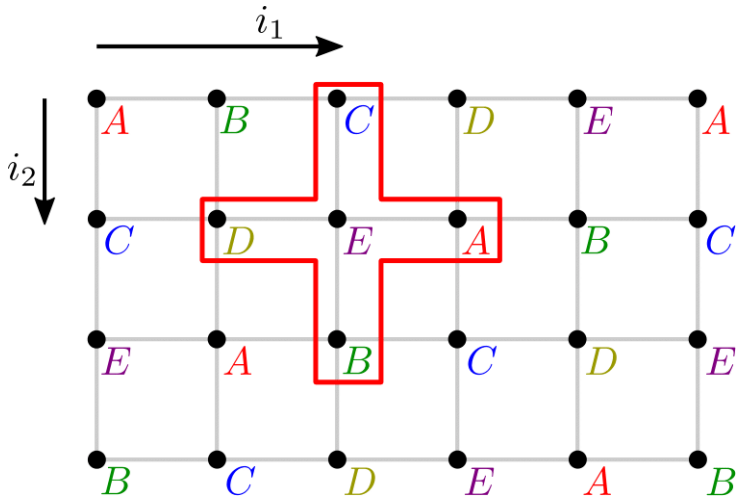

Figure 2.5.: *Labeling to measure star RDM on the planar square lattice, given by Eq. (2.23). For clarity, the numerical labels in the text have been converted to letters with the standard mapping* $0 \to A$, $1 \to B$, $\cdots$, *and color-coded. This figure was preprinted in Ref. [181].*

We now move on to two-dimensional geometries, starting by the square lattice. The first RDM tackled here is the star, composed of one qubit and all its neighbors, a $k = 5$-RDM in this geometry. A single labeling $\boldsymbol{a}$ covers all possibilities with the minimum of $k = 5$ labels. It labels rows cycling through a 5- alphabet like the string above, but adding an offset of 2 for each row (see Fig. 2.5). With lattice sites now denoted by the pair (i_1, i_2), its elements read

$$a_{i_1,i_2} = (i_1 + 2i_2)\ b\ mod\ 5\ . \tag{2.23}$$

Since 5 labels are used, $N = 3^5$ measurements are needed.

An (ℓ_1, ℓ_2)- plaquette is defined as an $(\ell_1 \times \ell_2)$- qubit rectangle aligned to the lattice (see Fig. 2.6). A measurement scheme for the k-RDMs of all (ℓ_1, ℓ_2)-plaquettes (with $k = \ell_1\ell_2$) can be made by composing the previous string scheme. The first row is labeled with an ℓ_1- alphabet as in the string, the second row is labeled with a different ℓ_1- alphabet, and the same goes for the first ℓ_2 rows, each with their different ℓ_1-alphabets. Row labelings repeat cyclically from the $(\ell_2 + 1)$- th row onwards, in a total of $\ell_1\ell_2$ labels (Fig. 2.6). Formally, the labeling reads

$$a_{i_1,i_2} = (i_1 \bmod \ell_1) + \ell_1(i_2 \bmod \ell_2)\ , \tag{2.24}$$

and appropriately covers all (ℓ_1, ℓ_2)- plaquettes with the minimal number $k = \ell_1\ell_2$

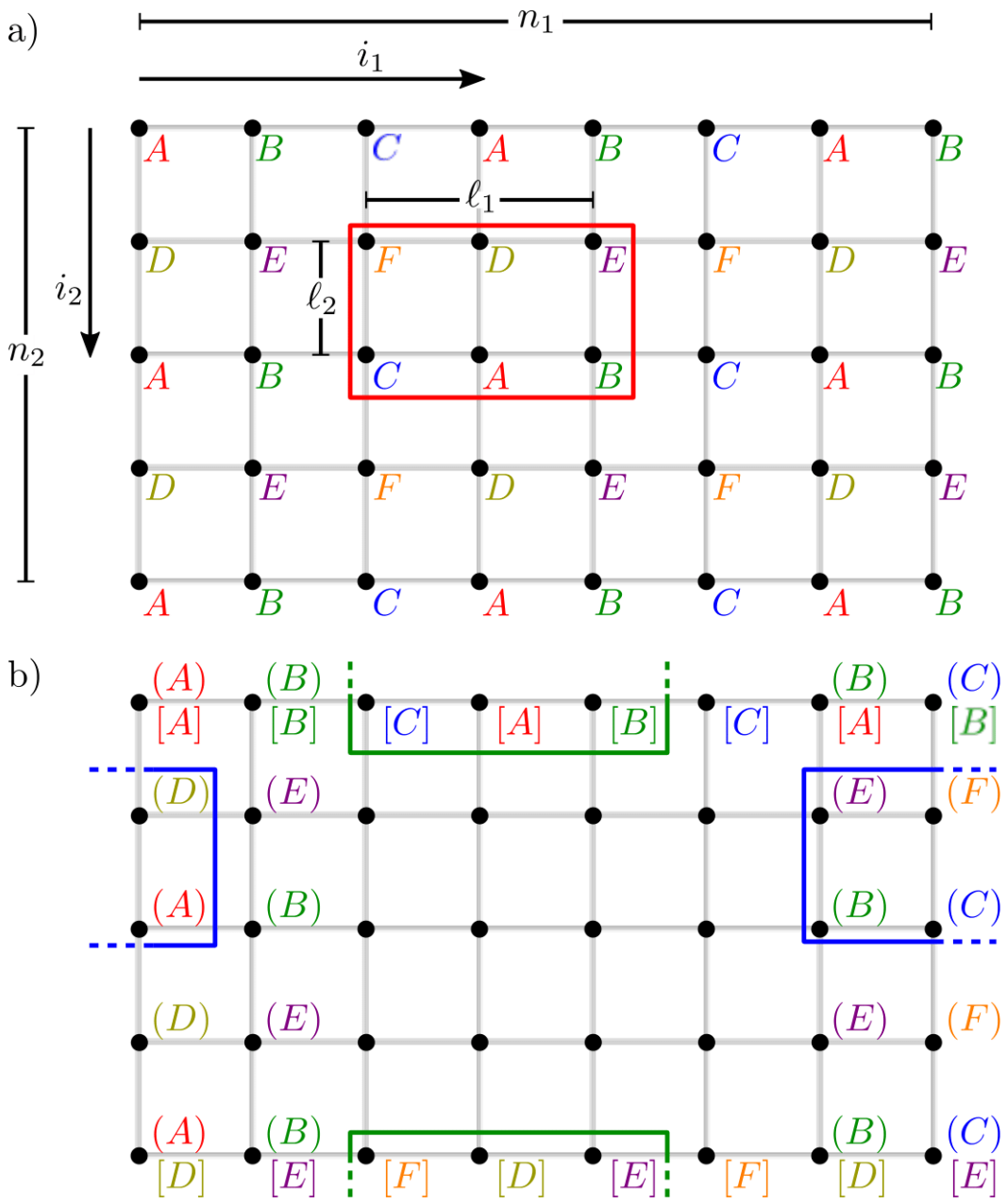

Figure 2.6.: *a) Labeling* $\boldsymbol{a}$ *for* (ℓ_1, ℓ_2)*-plaquettes in the planar square qubit lattice, from Eq. (2.24), with* $(\ell_1, \ell_2) = (3, 2)$*. b) Additional labelings needed for the cylinder and torus geometries, with* $n_1 = 8$*,* $n_2 = 5$*. The cylinder geometry requires* $\boldsymbol{b}$ *from Eq. (2.26) (in parentheses); the torus geometry requires* $\boldsymbol{b}$ *and also* $\boldsymbol{c}$ *from Eq. (2.26) [in square brackets]. Plaquettes crossing each edge are illustrated. For clarity, the numerical labels in the text have been converted to letters with the standard mapping* $0 \to A$*,* $1 \to B$*,* $\cdots$*, and color-coded. This figure was preprinted in Ref. [181].*

of labels, hence $N = 3^k = 3^{\ell_1 \ell_2}$. We call cylinder a square lattice where sites on the last column are first neighbors to same-row sites on the first column. Let the total lattice have dimension $n_1 \times n_2$, where $n = n_1 n_2$. To measure all (ℓ_1, ℓ_2)- plaquettes in the cylinder when $n_2 \bmod \ell_2 \neq 0$, it takes an additional labeling as in the ring case. The additional labeling is $\boldsymbol{b}$, with elements

$$b_{i_1,i_2} = \begin{cases} a_{i_1,i_2} \ , & \text{for } i_1 \in [\ell_1 - 1] \\ a_{i_1 - n_1, i_2} \ , & \text{for } i_1 \in \text{last}_{\ell_1 - 1}[n_1] \\ \text{no label} & \text{otherwise} \ , \end{cases} \tag{2.25}$$

with a_{i_1,i_2} from Eq. (2.24). It labels only the leftmost and rightmost $(\ell_1 - 1)$ columns and, analogously to the ring, covers all (ℓ_1, ℓ_2)- plaquettes across the vertical edges. With two labelings, the number of measurements is $N = 2 \times 3^k$. When the first and last rows of a cylinder are also taken as first neighbors (column-wise), we obtain a torus. If both $n_1 \bmod \ell_1 \neq 0$ and $n_2 \bmod \ell_2 \neq 0$, a third labeling $\boldsymbol{c}$ is needed, analogous to Eq. (2.25), but switching horizontal and vertical directions. With a_{i_1,i_2} from Eq. (2.24), $\boldsymbol{c}$ is given by

$$c_{i_1,i_2} = \begin{cases} a_{i_1,i_2} \ , & \text{for } i_2 \in [\ell_2 - 1] \\ a_{i_1, i_2 - n_2} \ , & \text{for } i_2 \in \text{last}_{\ell_2 - 1}[n_2] \\ \text{no label} & \text{otherwise} \ , \end{cases} \tag{2.26}$$

and labels the topmost and bottommost $(\ell_2 - 1)$ rows. With three labelings, the number of measurements is $N = 3 \times 3^k = 3^{k+1}$. Notably, the torus topology makes a third labeling necessary in general (4.1). In fact, any labeling $\boldsymbol{a}$ of the square lattice can be patched for the cylinder and torus geometries with the strategy above, as long as the maximal dimensions of the desired RDM are $\ell_1 \times \ell_2$. Applying this to the star-RDM labeling --- i.e. substituting Eq. (2.26) in Eqs. (2.36, 2.26) with

$\ell_1 = \ell_2 = 3$ ---, one finds

$$b_{i_1,i_2} = \begin{cases} (i_1 + 2i_2) \bmod 5 \ , & \text{for } i_1 \in [2] \\ (i_1 - n_1 + 2i_2) \bmod 5 \ , & \text{for } i_1 \in \text{last}_2[n_1] \\ \text{no label} & \text{otherwise} \end{cases} \tag{2.27}$$

$$c_{i_1,i_2} = \begin{cases} (i_1 + 2i_2) \bmod 5 \ , & \text{for } i_2 \in [2] \\ (i_1 + 2i_2 - 2n_2) \bmod 5 \ , & \text{for } i_2 \in \text{last}_2[n_2] \\ \text{no label} & \text{otherwise} \end{cases} \tag{2.28}$$

and the number of measurements is $N = 2 \times 3^5$ for the cylinder ($\boldsymbol{a}$ and $\boldsymbol{b}$) and $N = 3 \times 3^5 = 3^6$ for the torus geometry ($\boldsymbol{a}$, $\boldsymbol{b}$ and $\boldsymbol{c}$). We now move on to a three-dimensional, cubic lattice. We begin by the star RDM, which includes a qubit and all its (six) first neighbors. This $k = 7$-RDM can be realized with one labeling $\boldsymbol{a}$ composed of $k = 7$ labels; it labels each plane as in the 2D star configuration (but with a 7-alphabet), with an offset of 3 between successive planes. With each site labeled by (i_1, i_2, i_3), $\boldsymbol{a}$ reads

$$a_{i_1,i_2,i_3} = (i_1 + 2i_2 + 3i_3) \bmod 7 \tag{2.29}$$

and implies $N = 3^7$ measurements.

An (ℓ_1, ℓ_2, ℓ_3)-block is an (ℓ_1, ℓ_2, ℓ_3)-qubit parallelepiped aligned to the lattice. Analogously to the plaquette, all such blocks can be labeled by

$$a_{i_1,i_2,i_3} = (i_1 \bmod \ell_1) + \ell_1(i_2 \bmod \ell_2) + \ell_1\ell_2(i_3 \bmod \ell_3) \ , \tag{2.30}$$

with $N = 3^k = 3^{\ell_1\ell_2\ell_3}$ measurements. If the rightmost face of the cubic lattice is considered first neighbor of the leftmost face, we then have a "thick" ring. With the lattice having dimensions $n_1 \times n_2 \times n_3$, and taking the $i_1 = 0$ face as neighbor to the $i_1 = (n_1 - 1)$ face, this thick ring has a cross section of dimension $n_2 \times n_3$ qubits. As in the original one-dimensional ring, this geometry requires one additional labeling, given by

$$b_{i_1,i_2} = \begin{cases} a_{i_1,i_2,i_3} \ , & \text{for } i_1 \in [\ell_1 - 1] \\ a_{i_1-n_1,i_2,i_3} \ , & \text{for } i_1 \in \text{last}_{\ell_1-1}[n_1] \\ \text{no label} & \text{otherwise} \ , \end{cases} \tag{2.31}$$

Geometry	Labelings	N (No. of measmts)	Eqs.
String	1	3^k	(2.21)
Ring (1D)	2	2×3^k	(2.21),(2.22)
Star (plane)	1	3^5	(2.23)
(ℓ_1, ℓ_2)-plaquette	1	$3^k = 3^{\ell_1 \ell_2}$	(2.24)
Cylinder	2×(planar)	2×(planar)	(2.24),(2.25)
Torus	3×(planar)	3×(planar)	(2.24),(2.25),(2.26)
Star (cubic)	1	3^7	(2.29)
(ℓ_1, ℓ_2, ℓ_3)-block	1	$3^k = 3^{\ell_1 \ell_2 \ell_3}$	(2.30)
Thick ring (3D)	2×(cubic)	2×(cubic)	(2.30),(2.31)

Table 2.2.: *Summary of the number of labelings and unique measurements for k-RDMs on the geometries considered in Subsection 2.3.1.1. For comparison, previous methods in the literature require at least $N \sim e^{\mathcal{O}(k)} \log n$ different measurements. The values of the cyclic geometries (ring, cylinder, torus, thick ring) are upper bounds, saturated when the dimensions of the lattice are not divisible by those of the RDM. This table was preprinted in Ref. [181].*

totaling $2 \times 3^{\ell_1 \ell_2 \ell_3}$ measurements. As was done for the cylinder and torus in the two-dimensional lattice, one can consider the other faces of the three-dimensional lattice to be first neighbors, and the additional labelings follow analogously. We summarize the results of this Subsection in Table 2.2.

2.3.1.2. Triangle and honeycomb

In this Subsection we treat different geometries, namely the triangle and the honeycomb lattices.

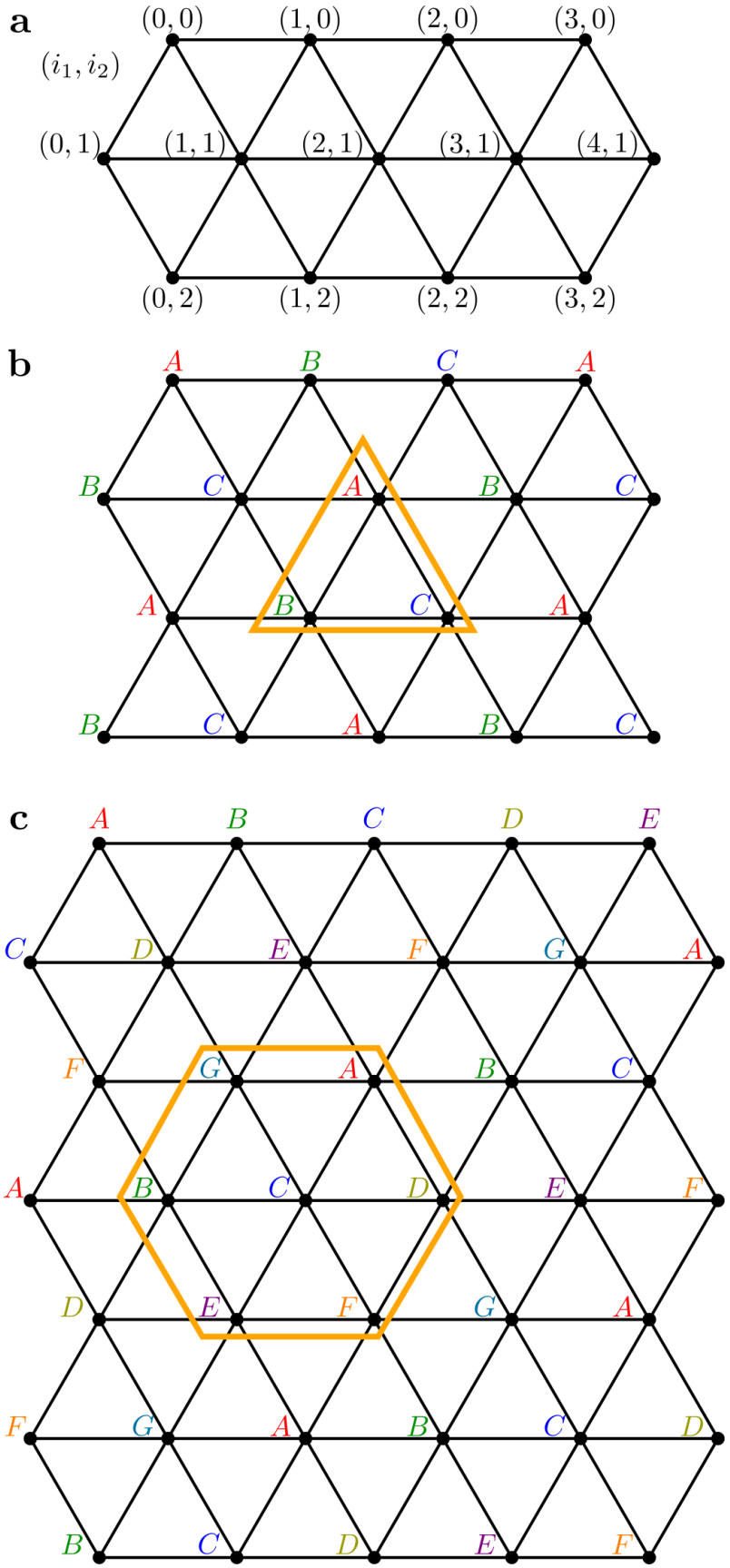

Figure 2.7.: *Labeling of the triangle lattice. a) Numbering scheme used in Eqs. 2.32, 2.33. b) Three-label scheme for the (triangular) plaquette. c) Seven-label scheme for the star RDM (qubit and its neighbors). This figure was preprinted in Ref. [181].*

For the triangle geometry, we begin with a labeling scheme that covers triangle RDMs. With three labels, it is also the minimal scheme for 2-RDMs. With the numbering defined in Fig. 2.7a), this labeling reads

$$a_{i_1,i_2} = (i_2 \bmod 2 + i_1) \bmod 3 \tag{2.32}$$

and is illustrated in Fig.2.7 b). Additionally, we present a scheme for the star RDM on this geometry, composed of a qubit and all its six neighbors (hence a 7-RDM):

$$a_{i_1,i_2} = \begin{cases} (i_1 - i_2) \bmod 7 \ , & \text{for } i_2 \text{ even} \\ (i_1 - i_2 + 3) \bmod 7 \ , & \text{for } i_2 \text{ odd} \end{cases} \tag{2.33}$$

which is illustrated in Fig.2.7c).

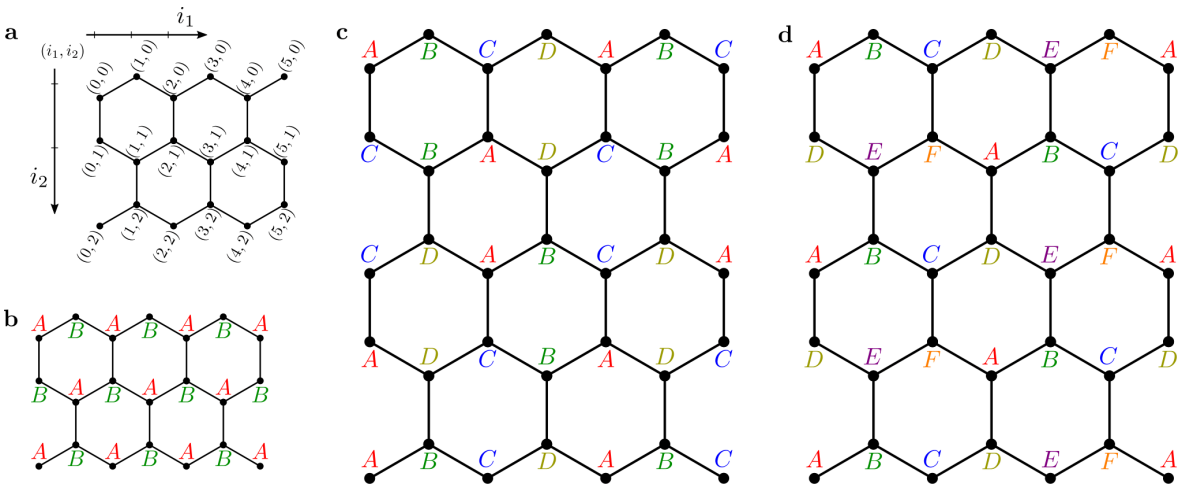

Figure 2.8.: *Labeling of the honeycomb lattice for different RDMs. a) Explicit illustration of the numbering used in Eqs. (2.34, 2.35, 2.36). b) Two-label scheme for first-neighbor 2-RDMs, Eq. (2.34). c) Four-label scheme, suitable for 3-RDMs and any 4-RDM where the four qubits are contiguous, but not in the same hexagon, given by Eq. (2.35). d) Six-label scheme, suitable for 4-,5-, 6-RDMs where all qubits of the RDM belong to same hexagon, given by Eq. (2.36). For clarity, the numerical labels in the text have been converted to letters with the standard mapping $0 \to A$, $1 \to B$, $\cdots$, and color-coded. This figure was preprinted in Ref. [181].*

We now deal with qubits on a honeycomb lattice. A first-neighbor 2-RDM can be achieved with two labels, simply assigning neighbors different labels. With the

numbering exemplified in Fig. 2.8a), this labeling reads

$$a_{i_1,i_2} = i_1 + i_2 \bmod 2 \ , \tag{2.34}$$

and is shown in Fig. 2.8b). Now we show a labeling that is useful for different sets of neighbors. It contains 4 different labels, as seen in Fig. 2.8c), and covers any 3-RDM, as well as any 4-RDM where the four qubits do not all belong to same hexagon. This includes the star configuration (a qubit and its three neighbors), as well as 4 qubits along the rows, among others:

$$a_{i_1,i_2} = \begin{cases} (-1)^{i_2}\ i_1 & \text{for } i_2 \bmod 4 = 0,3 \ , \\ (-1)^{i_2}\ i_1 + 2 & \text{for } i_2 \bmod 4 = 1,2 \ , \end{cases} \tag{2.35}$$

equivalently, $a_{i_1,i_2} = \left((-1)^{i_2} i_1 + 2\left\lfloor \frac{(i_2+1) \bmod 4}{2} \right\rfloor\right) \bmod 4$. It is perhaps clearer to describe this labeling with the following algorithm: for the first row, assign labels sequentially ($a_{i_1,0} = i_1 \bmod 4$). For the remaining sites, assign them the same color as the site diametrically opposite to it in any given hexagon, as in Fig. 2.8 c). This is evidently the minimal labeling for the 4-RDMs, and is also the minimal for the 3-RDMs, which cannot be covered with 3 labels only.

Lastly, we present a final labeling for the honeycomb, composed of 6 labels. It covers hexagon RDMs (containing all qubits in a hexagon), as well as 4-RDMs and 5-RDMs with all qubits in the same hexagon. It is depicted in Fig. 2.8 d) and is given by

$$a_{i_1,i_2} = [3(i_2 \bmod 2) + i_1] \bmod 6 \ . \tag{2.36}$$

Interestingly, this labeling also covers (non-optimally) all previously mentioned honeycomb RDMs.

We summarize the results of this Section in Table 2.3.

2.3.2. Local fermionic k- RDMs

For fermions in a lattice, k - RDMs provide information on arbitrarily distant lattice sites, which is not the purpose of this work. We are interested in $\langle \gamma_{i_0} \gamma_{i_1} \cdots \gamma_{i_{2k-1}} \rangle$, where all γ_i belong to a subset of lattice sites. We call these expectation values, then, elements of a *lattice-restricted matrix* of size k, or k- LRM, for short. An entire

No. of qubits	Labels	N (No. of measmts)	Eq.
Triangle			
3 (plaquette)	3	3^3	(2.32)
7 (star RDM)	7	3^7	(2.33)
Honeycomb			
2	2	3^2	(2.34)
3, or 4 not in same hexagon	4	3^4	(2.35)
up to 6 in single hexagon	6	3^6	(2.36)

Table 2.3.: *Summary of the number of labels and unique measurements for neighbor k-RDMs on the sets and geometries considered in Subsection 2.3.1.2. For comparison, previous methods in the literature require at least $N \sim e^{\mathcal{O}(k)} \log n$ different measurements. This table was preprinted in Ref. [181].*

k-LRM will contain such expectation values for all lattice subsets of a certain class, e.g. all neighboring pairs of lattice sites. A k-LRM contains less information than a k-RDM, unless the subset is taken to be the entire lattice, for which the k-LRM coincides with the k-RDM.

Additionally, for fermions one cannot simply rely on the tensor-product structure of operators acting on different sites to ensure commutativity (hence joint measurability). As such, measuring a given element no longer assumes access to individual measurements on each site.

Different Majoranas always anticommute, and they can be compounded to form commuting operators — e.g. two pairs of Majoranas commute as long as all four Majoranas involved are different. We call j-Majorana string a product $\gamma_p \cdots \gamma_q$ of j Majoranas, and the overlap of two Majorana strings is the set of Majoranas the two have in common. In general, two Majorana strings commute when the length of their overlap has the same parity as the product of their lengths.

1 - LRMs:

The 1-LRMs for neighbor fermions on a lattice present a simplified structure: since two different pairs of Majorana operators can only overlap in a single γ_i, any overlapping pairs anticommute and are incompatible. The 1-LRM then reduces to the problem of covering all relevant pairs of Majoranas without using any overlap. Interestingly, the problem reduces to that of edge-coloring a graph [184, 185]: how to color the edges of a graph such that any two edges that share a vertex have different colors.

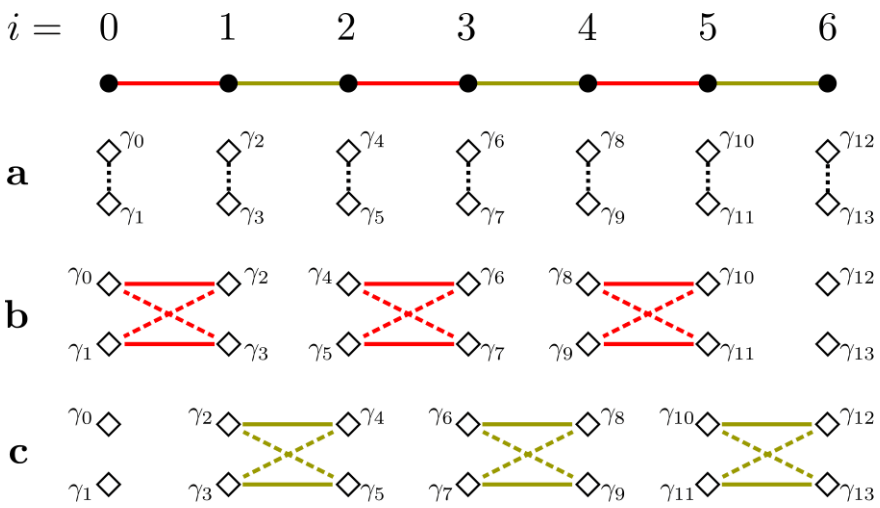

Figure 2.9.: *Fermionic 1-LRMs, edge-coloring of a graph and Vizing's theorem. Each lattice site (black circle) has* $\Delta = 2$ *neighbors and the graph can be colored with only* $c = 2$ *colors. The scheme shows the* $N = 2c + 1 = 5$ *measurements needed on the Majorana operators (white losanges). a) Same-site measurement; b) two measurements made on the red (dark) edges, the first for equal-parity* γ_j *(solid lines) and the second for opposite-parity* γ_j *(dashed lines); c) two measurements on the tan (light) edges, analogous to b). This figure was preprinted in Ref. [181].*

To see this, consider that a graph G defines the lattice, with each fermion site being a vertex and an edge connecting first neighbors. To each site i correspond two Majoranas γ_{2i}, γ_{2i+1}. Since the pairs $\gamma_{2i}\gamma_{2i+1}$ for different values of i all commute, they can all be measured at once in a first measurement [same-site measurement, see Fig. 2.9 a)].

If an edge connects vertices i and j, the pairs composed of the elements in $\{\gamma_{2i}, \gamma_{2i+1}, \gamma_{2j}, \gamma_{2j+1}\}$ must be measured. This requires two measurements (besides the same-site one): first the equal-parity measurement $\{\gamma_{2i}\gamma_{2j}, \gamma_{2i+1}\gamma_{2j+1}\}$ [Fig. 2.9 b)], and second the opposite-parity measurement $\{\gamma_{2i}\gamma_{2j+1}, \gamma_{2i+1}\gamma_{2j}\}$ [Fig. 2.9 c)]. To measure the entire LRM one could, in principle, make two measurements for each edge of G, but the total amount of measurements would be unnecessarily high.

A more efficient approach is to make as many of those measurements in parallel as possible. The restrictions to parallelization are that edges connected to the same vertex cannot be measured at the same step: if (i, j) and (i, j') are edges of G, their measurements cannot be made in parallel for they would overlap in γ_{2i} or γ_{2i+1}. This restriction is precisely described by the edge-coloring of G. To each color correspond two measurements, on top of the same-site one. For a total of c colors, this scheme takes $N = 2c + 1$ measurements (see Fig. 2.9). Importantly, Vizing's theorem [184, 185] bounds the amount of colors needed to edge-color a given graph: for a

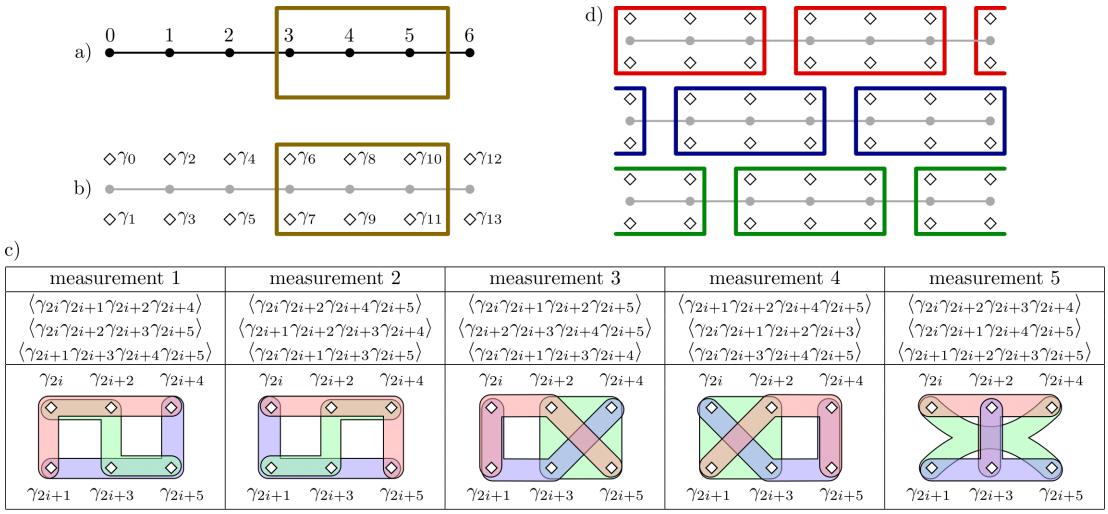

Figure 2.10.: *Measurements of a three-lattice-site tile of a Fermionic 2-LRM. Illustration of the string lattice [black circles, in a)] and of the Majorana operators, two per lattice site [white losanges, in b)]. In c), the five measurements to be performed in each tile are shown, each obtains three (compatible) elements of the 2-LRM. In d), tiling for the string lattice with three displacements total. This figure was preprinted in Ref. [181].*

graph of degree Δ, the amount of colors needed is either $c = \Delta$ or $c = \Delta + 1$. As such, this scheme makes use of, at most, $N = 2\Delta + 3$ measurements.

Finally, this scheme can be extended to 1-LRMs that include next-to-nearest neighbors. One need only create an auxiliary graph G' that has all vertices and edges of the original graph G, plus edges that connect next-to-nearest neighbors. Edge-coloring of G' indicates a suitable measurement scheme that requires at most $N = 2\Delta' + 3$ measurements, where Δ' is the degree of G'.

2 - LRMs:

The 2-LRM for pairs of first neighbors presents, surprisingly, an even simpler structure. For any neighboring pair of lattice sites (i, j), the first-neighbor 2-LRM has a single element $\langle \gamma_{2i}\gamma_{2i+1}\gamma_{2j}\gamma_{2j+1} \rangle$. For any other pair (i', j') of lattice sites, the overlap is either of two or zero Majoranas, so all such elements commute. Hence all pertinent Majorana strings are jointly measurable, i.e. a single measurement $N = 1$ can be made to provide the 2-LRM for pairs of first neighbors.

Let us now go beyond first neighbors in specific geometries, beginning with the string lattice. For the 2-LRM for three contiguous sites in the string lattice, i, $i + 1$, $i + 2$, we will use a tiling strategy. Each tile will be composed of three sites [six Majoranas; see Fig. 2.10 a) and b)]. Five measurements, with three LRM elements each, suffice to cover a tile; these are shown in Fig. 2.10 c). A total of

three displacements of the original tiling is needed [see Fig. 2.11 d)], which leads to $N = 15$ measurements total.

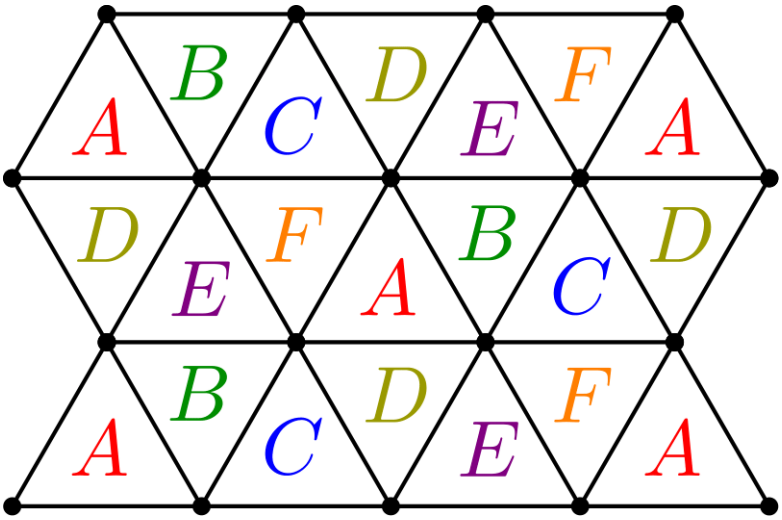

Figure 2.11.: *Illustration of the tiling for triangle 2-RLM. For a given letter, e.g. A, each tile comprises the three lattice sites of the triangles assigned that letter. In each tile, measurements made as in Fig. 2.10c), with all same-letter tiles measured simultaneously. Six tilings, one for each letter, are needed. This figure was preprinted in Ref. [181].*

In fact, these measurements remain useful for three-site 2-LRMs of any geometry. Consider, e.g., the triangular lattice from Fig. 2.11 and in it the fermionic 2-LRM for sites arranged in a triangle. The lattice needs to be tiled into triangles, and for each triangle, the five measurements in Fig.2.10 are used (with a simple change of geometry). The tiling must be such that tiles do not overlap, and a total of six displacements are needed, as shown in Fig.2.11. This leads to $N = 30$ measurements total for this 2-RLM.

2.4. Application

2.4.1. Motivation and posing the problem

Quantum computing is a celebrated emergent technology witnessing a surge of new developments both in theoretical and experimental sides during recent years [186, 187]. It has been used to address particular classical problems [188, 189, 190], or more recently general optimization [191, 192, 193, 194, 195] or Machine Learning [196, 197, 198, 199, 200, 201, 202]. However, quantum computing is particularly well suited for simulating quantum properties of nature [203, 204, 205], while doing so in classical computers is extremely inefficient [206]. Some examples include quantum

chemistry [207, 208, 209, 210, 211], condensed matter systems [212, 213], or analysis of quantum data [214, 215]. Despite this advantage, current capabilities of quantum hardware are still far from simulating systems of practical interest.

Adiabatic evolution processes are among the strategies that can be followed to perform computations on quantum devices. Adiabatic evolution, based on the adiabatic theorem [216], is implementable both in quantum-annealing and quantum gate-based [217] hardware. In the adiabatic process, a time-dependent Hamiltonian interpolates from an initial well-controlled Hamiltonian to a final one encoding the problem of interest. Starting from the initial ground state, the system is gradually evolved according to the time-dependent Hamiltonian. For gapped systems and a slow enough transition, the final state approximates to the ground state of the problem Hamiltonian.

An interesting problem to solve with quantum computing is the simulation and analysis of materials down to the atomic level. In particular, single layer crystalline solids allow to study interesting physical phenomena without the computational burden of full 3D material simulations. Among these, graphene stands out as a novel material with exciting mechanical, thermal, optical, and electronic properties [218], including superconductivity [219]. Graphene is composed of a bidimensional lattice of carbon atoms displayed in a honeycomb structure. Its isolation and characterization in 2004 [220], together with its demonstrated technological potential [221], has motivated the design and production of artificial graphene (**AG**) [222], that is, more general two-dimensional fermionic platforms that maintain the hexagonal structure. **AG** systems preserve the main electronic properties of graphene, owing to the preserved hexagonal symmetry of the lattice, while representing much more tunable platforms that permit to model imaginative electronic interactions or explore new phases of matter. A simple yet successful model to capture the electronic features of material lattices, including **AG**, is the Fermi-Hubbard model [223]. This model considers hopping, Coulomb and spin-orbit interactions among the free-moving electrons in the lattice.

There already exist a number of approaches to solve this problem. It can be solved with high accuracy with exact diagonalization methods, although the exponential scaling of the Hilbert space makes this approach practically useless for already relatively small lattices. Other classical methods such as **DMRG** [224, 225] find an approximation to the ground state of a given system using variational approaches and composing smaller systems into a larger one. They can only be applied on classical machines since non-unitary operations are performed. Thus, the calculation is subject to a dimensionality curse in the description of the quantum state, and a

trade-off between available accuracy and size arises. In the quantum side, variational methods are also explored [226]. Optimizing such problems is in general difficult and requires much classical computational power.

In this work, we develop an algorithm for gate-based quantum computers that simulates an adiabatic evolution and outputs the ground state of the free-moving electrons in AG. The algorithm is composed of four steps. First, the problem is mapped from the fermionic operators to a qubit-based implementation suitable for quantum computers. The standard Jordan-Wigner map is used for this purpose. Second, an initial state to start the adiabatic process is generated. This can be done efficiently under some requirements [227]. Third, the adiabatic evolution is conducted. The recipe is based on that of a square lattice [226], properly adapted and extended to match the present problem. Finally, a tailored measurement strategy is described to measure all terms in the **AG** Hamiltonian while minimizing the number of circuit executions.

The algorithm here presented is efficient since its scaling in number of qubits and operations increases linearly with the size of the lattice, both for the preparation of the initial state and for each step of the adiabatic evolution. The techniques disscussed in this chapter find a direct application in the construction of the measurement in the algorithm. The number of measurements is constant as the system size increases. This scaling contrasts with the classical simulation of the same problem, where only the storing of the electronic wavefunction is exponential in the size of the system. In addition, note that no classical computational power is needed apart from processing data.

The quantum algorithm is tested using classical machines, including the supercomputer MareNostrum 4, hosted at BSC [228], in the case of large systems. The simulations are carried out using an exact statevector (**SV**) representation, provided by the `Qibo` framework [229], and a Matrix Product State (**MPS**) one. The latter is obtained by translating the quantum circuit to an **MPS** by the library `quimb` [230], and then contracted using local truncation using the library `RosNet` [231]. Using exact simulation, the largest simulatable system is four hexagons in a 2×2 lattice, with 32 qubits. In the **MPS** case, four hexagons in a 1×4 lattice, represented by 36 qubits, are achieved with high fidelities. The limits of these results are imposed by hardware.

2.4.2. Fermi-Hubbard model graphene

The present example is based on the Fermi-Hubbard model [223] as applied to a graphene lattice with Rashba spin-orbit coupling (**SOC**) term which was one of the

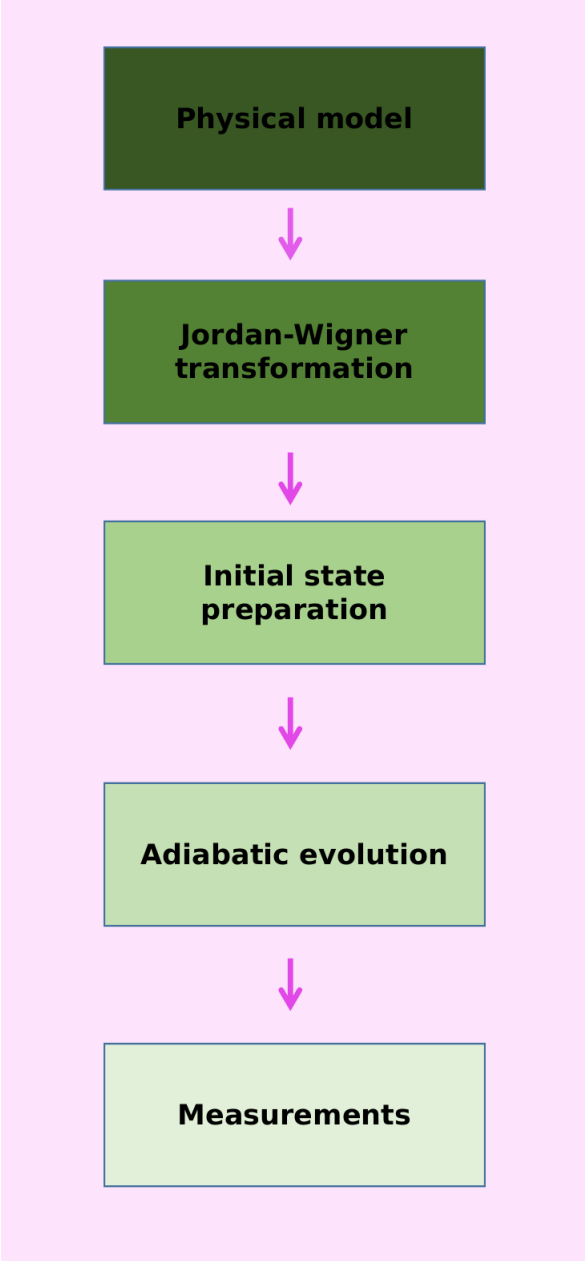

Figure 2.12.: *General "recipe" for an adiabatic quantum algorithm.*

main object of studying in the first chapter of this thesis manuscript. The Fermi-Hubbard model is widely used in condensed matter as a reasonable approximation to fermionic systems [227]. It approximates the long-range Coulomb interactions among electrons in a crystal with local interactions in each lattice site. It includes a kinetic term modeling the hopping of electrons among first neighbors, and we also include the spin-orbit Rashba term, allowing electrons to hop while also switching the spin. The Hamiltonian of such model is defined as

$$\begin{aligned} H_{FH} = & -t \sum_{\langle ij \rangle, \sigma} a^{\dagger}_{i,\sigma} a_{j,\sigma} + U \sum_{i} a^{\dagger}_{i,\uparrow} a_{i,\uparrow} a^{\dagger}_{i,\downarrow} a_{i,\downarrow} \\ & + \frac{2i}{3} \lambda_R \sum_{\langle ij \rangle, \sigma, \sigma'} a^{\dagger}_{i,\sigma'} a_{j,\sigma} [(\vec{\sigma} \times \vec{d}_{ij})_z]_{\sigma,\sigma'}, \end{aligned} \tag{2.37}$$

and for simplicity we define the hopping, Coulomb and spin-orbit Hamiltonians respectively as

$$H_H = -t \sum_{\langle ij \rangle, \sigma} a^{\dagger}_{i,\sigma} a_{j,\sigma}, \tag{2.38}$$

$$H_C = U \sum_{i} a^{\dagger}_{i,\uparrow} a_{i,\uparrow} a^{\dagger}_{i,\downarrow} a_{i,\downarrow}, \tag{2.39}$$

$$H_{SO} = \frac{2i}{3} \lambda_R \sum_{\langle ij \rangle, \sigma, \sigma'} a^{\dagger}_{i,\sigma'} a_{j,\sigma} [(\vec{\sigma} \times \vec{d}_{ij})_z]_{\sigma,\sigma'}. \tag{2.40}$$

t, U, λ_R are respectively the hopping, Coulomb and spin-orbit couplings. Operators $a_{i,\sigma}$ and $a^{\dagger}_{i,\sigma}$ annihilate and create an electron in site i with spin σ. Sums over $\langle ij \rangle$ in the case of hopping and spin-orbit terms take into consideration only the contributions between sites (i, j) connected by a single edge in the graphene lattice, which we consider to have regular, non-periodic boundary conditions. $\vec{\sigma}$ and $\vec{d}_{ij}$ in the spin-orbit term are the vector of Pauli matrices and the (unitary) vector between sites i and j in the lattice. Any length of $\vec{d}_{ij}$ can be absorbed in a simple re-scaling of λ_R .

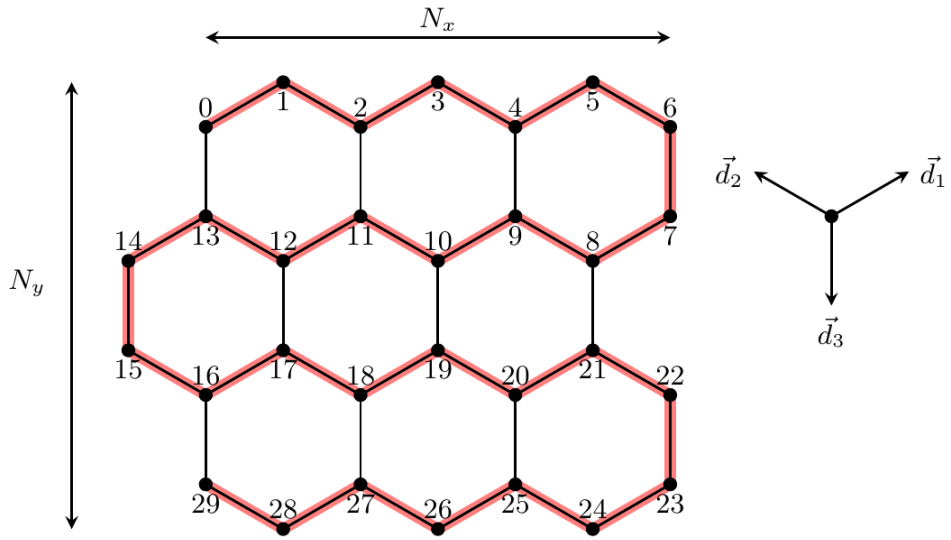

Figure 2.13.: *Graphene lattice used in this work, defined by the number of hexagons in each dimension* (N_x, N_y)*. Sites are numbered following the red shadow. The regular hexagons are composed of the unitary vectors connecting sites* $\vec{d}_i$*, on the right side, defined in Eq. (2.41). This figure was taken from Ref. [232].*

The graphene lattice here considered is depicted in Fig. 2.13, with each site corresponding to two orbitals, one for spin up $\uparrow$, and another for spin down, $\downarrow$. The lattice follows a standard honeycomb structure where the number of hexagons on directions x and y is always maintained.

All hexagons are regular, with all sites equally spaced, and oriented in a zig-zag configuration. The vectors connecting sites are easily found as

$$\begin{aligned} \vec{d}_1 &= \frac{\sqrt{3}}{2}\hat{e}_x + \frac{1}{2}\hat{e}_y \\ \vec{d}_2 &= -\frac{\sqrt{3}}{2}\hat{e}_x + \frac{1}{2}\hat{e}_y, \\ \vec{d}_1 &= -\hat{e}_y, \end{aligned} \tag{2.41}$$

where $\hat{e_j}$ is the unit vector in direction j.

2.4.3. Jordan-Wigner mapping

The first step in the algorithm is to map the sites and orbitals in the Fermi-Hubbard model to qubits in a quantum computer. The correspondence between orbitals and qubits traces the snake-like pattern shadowed in red in Fig. 2.13, with two qubit

numbers for each site, since each orbital can be occupied by an electron with spin ↑ or ↓. The particular relation between spins and qubit numbers depends on the row of the lattice. We follow the numbering from Fig. 2.13, and label rows and columns of qubits from top to bottom and left to right, starting with zero. Thus, in even rows of sites, the spins ↑ have an even label, while ↓ have an odd one. In odd rows, the label is inverted.

$$s_{\text{even rows}} \rightarrow 2s, 2s+1 = \{\uparrow, \downarrow\} \tag{2.42}$$

$$s_{\text{odd rows}} \rightarrow 2s, 2s+1 = \{\downarrow, \uparrow\} \tag{2.43}$$

For example, in the lattice of Fig. 2.13, spins ↑ and ↓ of site number six, correspond to labels 12 and 13, while the same spins for site number seven are mapped to qubit numbers 15 and 14.

Each combination of site and spin is then mapped to qubits via the Jordan-Wigner mapping [233]. According to this mapping, the creation and annihilation operators are transformed via

$$a_j^\dagger = \prod_{k=0}^{j-1} \sigma_k^{(z)} \frac{1}{2}(\sigma_j^{(x)} + i\sigma_j^{(y)}) \tag{2.44}$$

$$a_j = \prod_{k=0}^{j-1} \sigma_k^{(z)} \frac{1}{2}(\sigma_j^{(x)} - i\sigma_j^{(y)}) \tag{2.45}$$

$$\tag{2.46}$$

where the chain of operators $\prod_{k=0}^{j-1} \sigma_k^{(z)}$ is used to keep track of the relative signs under commutations of two fermions.

2.4.4. Initial state preparation

The initial state used for the adiabatic evolution will be the ground state of a tight binding Hamiltonian H_{TB} defined as

$$H_{TB} = H_H + H_{SO}, \tag{2.47}$$

that is, a Hamiltonian where the only energetic terms are among the sites. Alternatively, it is also possible to take the hopping Hamiltonian H_H as the starting point.

Both kinds of Hamiltonian satisfy the conditions to be a fermionic Gaussian state

[227, 234] defined as

$$H_G = \sum_{j,k=1}^{N} M_{jk} a_j^\dagger a_k + \sum_{j,k=1}^{N} (\Delta_{jk} a_j^\dagger a_k^\dagger + h.c.). \tag{2.48}$$

Jiang et al. in Ref. [227] show that the ground state of an arbitrary Gaussian Hamiltonian can be constructed efficiently on a quantum computer. In particular, it requires $\mathcal{O}(n^2)$ operations and $\mathcal{O}(n)$ depth, where n is the total number of qubits. The scaling for the problem here considered will be $n = \mathcal{O}(N_x N_y)$. In this work, the `Openfermion` [235] implementation for que quantum computing library `Cirq` [236] is used to construct this ground state.

Notice that the mapping used in this algorithm follows a 1D path, while the problem is 2D. This is a consequence of the fermionic features of the model. All interchanges of two fermions must carry a phase change. To the best of our knowledge, there is no 2D fermionic mapping suiting this problem, apart from the folding of a 1D chain into a larger dimensional space.

2.4.5. Adiabatic Evolution

Adiabatic evolution is the central piece of the algorithm here developed. In the adiabatic evolution the system is initially affected by a Hamiltonian whose ground state is known. Then, the Hamiltonian is slowly changed to another one encoding the problem to be solved and whose ground state is unknown. If the evolution is performed slowly enough, then the final state will be close to the ground state, the solution of the problem, of the final Hamiltonian [237, 216, 238]. The evolution time must be at least $\mathcal{O}(g^2)$ where g is the gap between the ground and first-excited states [237].

In our case, the initial Hamiltonian and ground state are H_{TB} and $|\psi_{TB}\rangle$. The problem Hamiltonian is H_{FH}, with ground state $|\psi_{FH}\rangle$. The time-depending Hamiltonian interpolating between both extrema during a total evolution time T is

$$H(s) = (1-s)H_{TB} + sH_{FH}, \qquad s = t/T. \tag{2.49}$$

By direct substitution from Eqs. (2.37) and (2.47) it is possible to rewrite the adiabatic time depending Hamiltonian as

$$H(s) = H_H + H_{SO} + sH_C, \tag{2.50}$$

that is, the Coulomb term is adiabatically turned on.

To perform the state evolution, the Schrödinger equation with the above time-dependent Hamiltonian is applied,

$$|\psi(T)\rangle = e^{-i\int_0^T H(t)dt} |\psi(0)\rangle \,. \tag{2.51}$$

This formal solution can be approximated by discretizing the evolution path as

$$|\psi(T)\rangle \approx \prod_{j=0}^{N} e^{-iH(j\delta t)\delta t} |\psi(0)\rangle \,, \tag{2.52}$$

where T is the total evolution time and $\delta t = T/N$ is the time taken in each step. The final state $|\psi(T)\rangle$ is approximated with an error in the relative fidelity of δt^2 [239].

2.4.6. Measurement

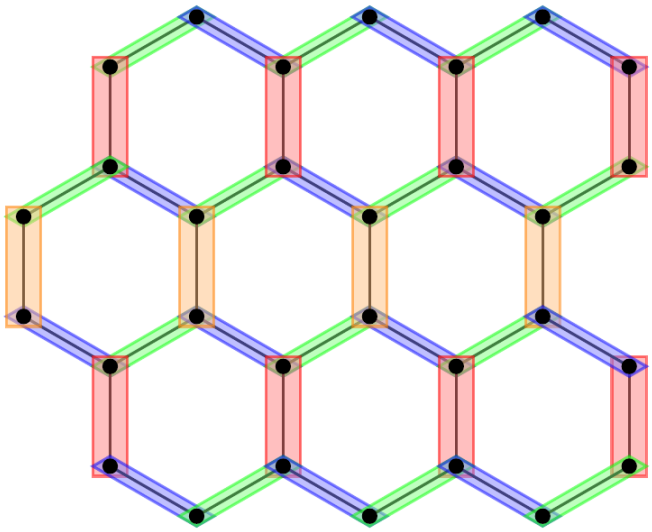

Figure 2.14.: *Measurement scheme for the lattice. All terms from H_{FH} coming from edges in the same color can be measured simultaneously. Horizontal terms can be measured directly since they do not commute. In the case of vertical terms, they are measured using swapping in a common substring in the full Jordan-Wigner mapping for all edges in the same row. Each of the four sets has two possible spins and regular and spin-orbit terms, amounting to a total of 16 independent measurements. Together with the Coulomb terms, the complete measurement can be done in only 17 steps, irrespective of the problem size. This figure was taken from Ref. [232].*

Once the adiabatic evolution is performed it is necessary to devise a measurement procedure to read out the energy of the system. A minimal set of measurements is obtained by grouping the different parts of the Hamiltonian into terms that commute with each other, so that they can be measured simultaneously. For each term, a set of swapping gates is applied to bring the relevant qubits together, in case they are not.

Then a change of basis is performed if the Hamiltonian term is non-diagonal. All Coulomb terms commute with each other, are diagonal, and involve adjacent qubits. They are of the form $|11\rangle\langle 11|$, where both qubits represent the two spins in each site. The total Coulomb energy is the sum of probabilities of measuring 11, P_{11}, in the two qubits of each site times the coupling U.

In the case of hopping terms, non-adjacent qubits are involved and swapping is needed. For horizontal terms, a set of even-odd and odd-even swaps for spins up and down suffices to bring both qubits together.

The corresponding Hamiltonian term, $|XX\rangle\langle YY|$, is diagonalized to $|01\rangle\langle 01|$ with the diagonalizing quantum circuit $\mathcal{D} = CNOT\ CH\ CNOT$, being CH the control Hadamard two-qubit gate. The energy of each term is then $P_{10} - P_{01}$.

Notice that the measurement strategy groups different 2-local Hamiltonian terms in such a way that all of them can be measured simultaneously, even though they do not commute given the Jordan-Wigner mapping. For vertical hopping terms the measurement must be done by taking many more qubits into account simultaneously. The grouping is done in even and odd rows of hexagons separately. Each pair of qubits in the vertical edge needs to be brought together to the right (or left) of the row, following the Jordan Wigner mapping and qubit chain.

The number of swaps needed scales as $\mathcal{O}(N)$. The measurement diagonalization is then done as in the previous case, but it must be carried through all qubits in the corresponding row. Hopping spin-orbit Rashba terms are analogous to the regular kinetic terms, except for the presence of an additional complex phase. The swapping is adapted to involve qubits corresponding to different spins.

All sets of measurements add up to seventeen different groups, see Fig. 2.14 for reference. For the Coulomb terms only one measurement is required. In the hopping case, only four different measurements are needed. Since there are two spins per electron, 8 terms are required. This same structure holds for the spin-orbit piece of the problem. The number of measurements corresponds to geometrical structures and does not depend on the size of the problem.

In conclusion, to take advantage of our method of overlapping quantum tomography in finite lattices, we must follow the steps presented in the Fig. 2.15.

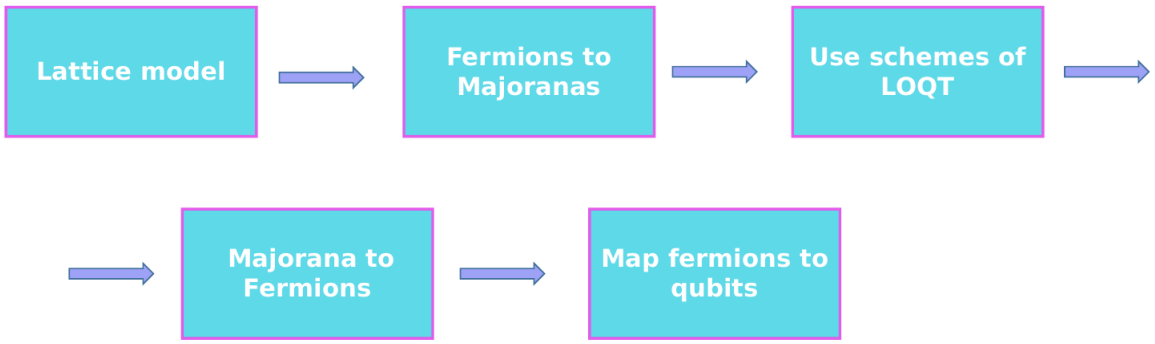

Figure 2.15.: *Applying LQOT for a quantum simulation in a quantum computing.* ***In first step:*** *select the lattice model.* **Second step:** *Convert the Dirac fermions to majorana fermions because the schemes to obtain fermionic k-RDMs are based in Majorana fermions.* **Third step:** *Apply our schemes of LOQT to get all proper Majorana combinations.* **Fourth step:** *Convert all Majorana fermions product combinations into Dirac fermions.* **Fifth step:** *Use a standard transformation to covert the Dirac fermions into qubits.*

2.5. Discussions

In this chapter, we have shown in section 2.3 the main results of an efficient set of strategies to perform overlapping quantum tomography for finite lattices. We also presented some outcomes (see Section 2.4) applying the knowledge acquired along this Ph.D., which connect the two parts of this thesis's manuscript. Thus, we proposed some schemes of measurements to obtain the ground state of an Fermi-Hubbard (**FH**) graphene system, one of the steps to building a quantum algorithm for artificial graphene (**AG**).

We have shown in our main results (see Ref. [181]) that:

- The full determination of the quantum state of a many-particle system is practically out of reach when increasing the system size. However, it is possible to access to partial, physically relevant information about this system with a much less demanding effort.
- We have studied local overlapping tomography of qubits and fermions in a lattice. We have specifically focused on k-RDMs (and k-LRMs) that are localized in neighboring sites of the lattice, which are often the subset that draws more interest in theoretical and practical terms.
- Resorting only to projective, product measurements, we have shown that

optimal measurement complexity can be directly tied to graph-coloring for the lowest values of k; and we have also studied optimal measurements tailored to several relevant geometries.

- An important result is that, unlike for the case of full RDMs, the amount of measurements to obtain these local matrices no longer depends on system size n. This has been seen in the studied geometries, in connection to graph-coloring, and also in the form of a general tiling argument.

Our work opens the path towards turning this form of local overlapping tomography into a viable candidate for measurements in practical scenarios. Thus, the application of our method is presented in Ref. [232].

3. Outlook

According to the knowledge acquired during this Ph.D., we can divide our research efforts for the near future into the following research lines.

3.1. Research line A: Quantum information in graphene.

In Part II of this thesis, I established some collaborations, and we started studies about how to use quantum information tools to explore physical questions in the graphene platforms. We can point out some ongoing works/research projects:

- **Formulation of an open quantum system theory for the intra-particle entanglement in a graphene monolayer based on quasiclassical theory:** We brought tools typically used in superconductivity physics as matrix quantum circuits- consisting of a semiclassical approach for studying coherent transport in nanostructures. Our analytical description includes all modes, different from using just a random matrix approach that is applied for zero-mode systems. We got original results and created a complete open quantum system theory for intra- and inter-particle correlations in graphene-based systems. In this formulation, we used the Keldysh formalism as well. So far, we have this paper in preparation: B.G.M. Araújo, A.M.S. Macêdo , *An open quantum theory for intraparticle quantum correlations in topological matter.* Main collaborator: Prof. A.M.S. Macêdo from UFPE, Brazil.

- **Emergence and detection of intra-particle entaglement in a Rashba SOC graphene monolayer in the non-equilibrium regime.** We showed that we do not have entanglement when considering the density matrix in equilibrium computed from the Fermi-Dirac statistics. But, when we added the non-equilibrium density matrix, we can verify that the spin-pseudospin entanglement emerges from the creation of currents. With this, we proposed the detection of entanglement through the correlations of the physical observables obtained by quantum spin hall experiments. Meanwhile, we have this work in

preparation: B.G.M.A., A.V., A. F. , *Detection of intraparticle entanglement in non-equilibrium.* Main collaborator: Dr. Aires Ferreira from University of York, UK.

- **Bayesian measurement strategies over continuous variables to obtain the heat current in some physical platforms:** Here we are using the Gaussian states (continuous variables) to study quantum thermodynamic properties of graphene/light-based systems, specifically, designing quantum thermometers as application. Main collaborator: Dr. Mohammad Mehboudi, University of Geneva, Switzerland.

- **Study hierarchical theory to solve complex problems in graphene-based platforms.** We have these original results: B.G.M. Araújo, A.M.S. Macêdo, *Theoretical reformulation of the spin-lifetime mechanisms in graphene using universality classes of hierarchical complex systems (H- theory)*. Main collaborator: Prof. Macêdo, UFPE, Brazil.

- **Study bipartite and n-partite correlations considering mixed states via random matrices ensembles in topological matter.**

In the coming two years, one of my research lines can be schematize in Fig. 3.1, connecting quantum thermodynamics with graphene-based systems.

3.2. Reseach line B: Quantum tomography techniques applied to variational quantum algorithms.

Regarding the main project of the second part of this thesis about (**LQOT**), we saw that the full determination of the information about many-particle quantum states is practically impossible for large systems. With this, we need to look for alternatives to contour this kind of obstacle in order to access the relevant physical information about these quantum states. Scalability is a critical issue.

We adapted the original method of overlapping quantum tomography (**QOT**) designed for free particles. We added constraints consisting of finite and periodic lattices geometries to obtain the k-particles RDMs. For this, we mainly perform partial quantum tomography for qubits and fermions. It focused on getting k-LRMs for the first neighbors of fermions in a lattice, which are essential from a theoretical

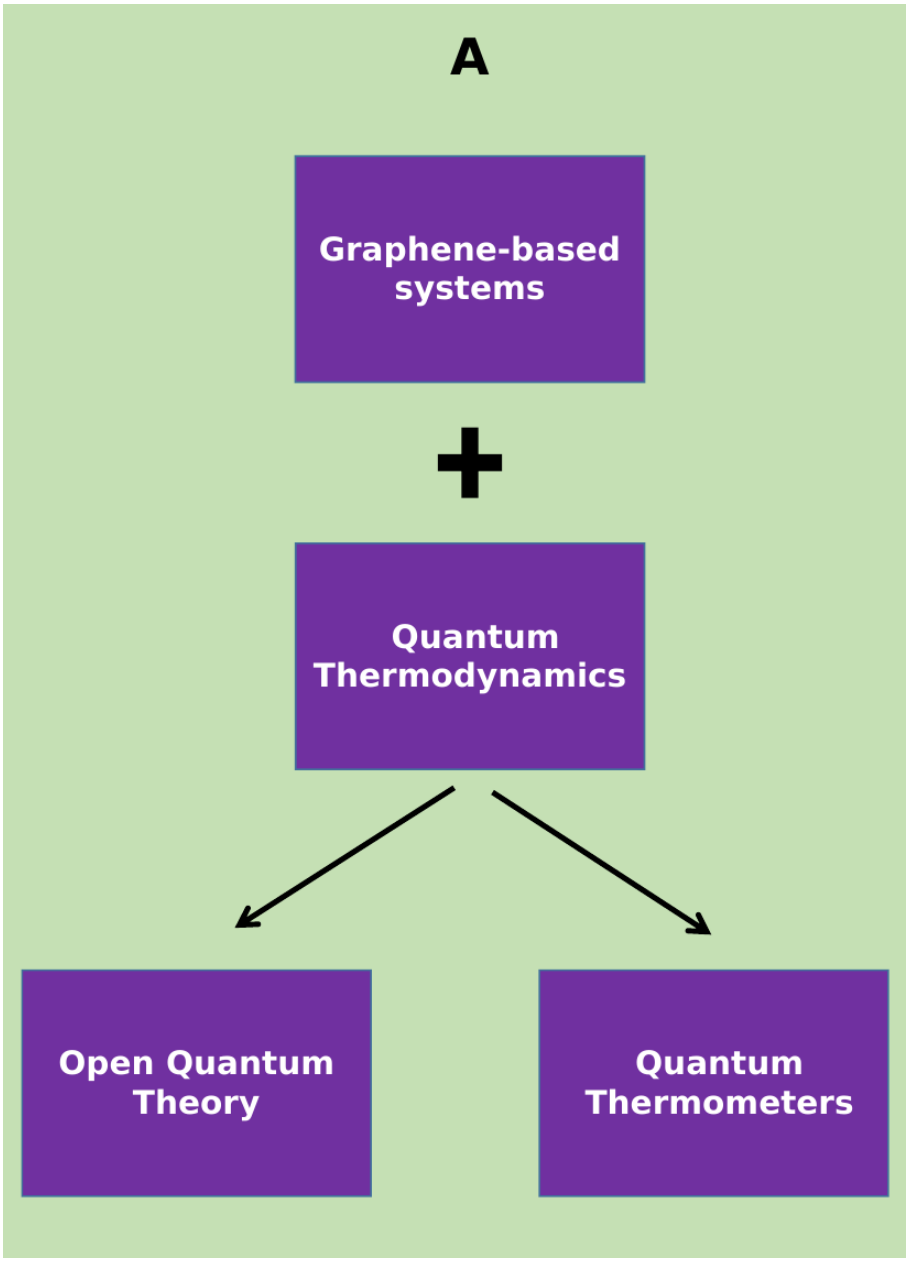

Figure 3.1.: ***Roadmap of Part I:*** *We are introducing new mathematical framework to explore some physical questions from quantum thermodynamics point of view in graphene systems. In this approach, we combine diverse tools from different research areas, such as: superconducting mathematical framework, H-theory, continuous variables, quantum transport tools, random matrices. From this, we are proposing since an open quantum theory framework to aspects more applied such as devising quantum thermometers for these graphene-based systems.*

and practical points of view. Our measurement schemes consists in obtained optimal strategies to get RDMs taking into consideration spatial locality (lattice constraint).

The main result consists of when we reduce one global degree of freedom of the original method and bring the free particles constrained to a lattice, giving us that the measurement scaling does not depend on the size of the system. These simple schemes open avenues to explore the local overlapping tomography for measuring practical physical setups, as we demonstrated in applying these ideas in a quantum algorithm.

From this, we plan to consider the following questions:

- We plan to study if we can devising an efficient method to obtain - in a unique mathematical construction, k-RDMs for N qubits or N fermions based on deterministic and randomized schemes of measurements. Specifically, try to build an explicit construction of overlapping tomography valid for any N and k particles through Young diagrams and explore applications of the resulting method.

- Adapt our **LQOT** for systems where symmetries add more constraints besides the lattice, for instance for non-periodic lattices, sparse models, or gauge lattice systems.

In the coming two years, my planned research effort along these lines is schematized in Fig. 3.2, which fits very well in the context of the study of variational quantum algorithms for many-body systems.

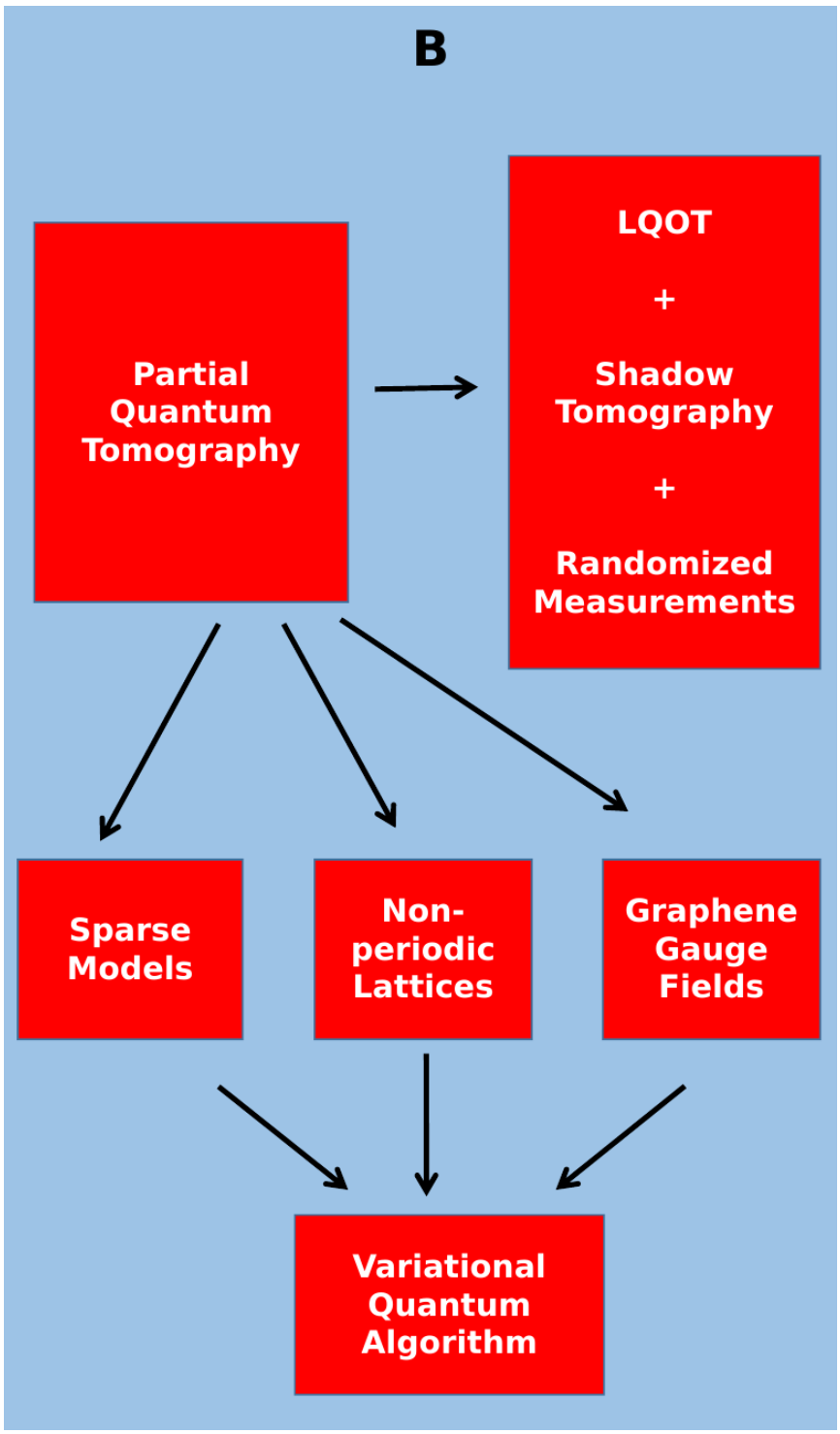

Figure 3.2.: ***Roadmap of Part II:*** *Design multiple partial quantum tomography methods to get RDMs and compute physical observables for use it as one of the steps to do variational quantum algorithms (* ***VQA****) for challenging systems.*

4. Appendix of Chapter 2

This appendix is a complementary material regarding the chapter 2.

4.1. Patching creases on looping geometries

Let us prove the statement that to measure plaquettes on the torus topology a third labeling is in general necessary. This happens because whenever $n_1 \bmod \ell_1 \neq 0$ and $n_2 \bmod \ell_2 \neq 0$ any labeling produces a vertical and a horizontal "crease" between lattice sites, across which plaquettes cannot be measured, and the additional labelings are meant to patch these creases (Fig.4.1). With only two labelings, we have two pairs of creases, each pair composed of a horizontal and a vertical crease.

The torus topology ensures that these pairs cross one another in at least two points, though. Any plaquette that encompasses one of the crossing points cannot be covered by the two labelings, requiring a third one.

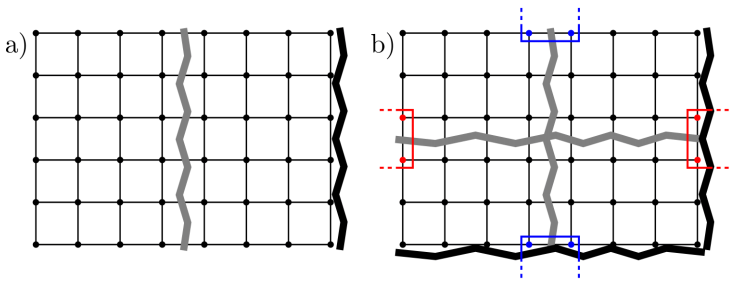

Figure 4.1.: *Creases on an 8×6 square lattice generated by different labelings. Black jagged lines: creases by labeling $\boldsymbol{a}$ from Eq. 2.24 on a) a cylinder and b) a torus. Gray jagged lines: creases by additional labeling $\boldsymbol{b}$ on each geometry [in the case of $\ell_1 = 4$, $\ell_2 = 3$, from Eq. 2.24 exactly]. Notice how on the cylinder a) the second labeling fully patches the creases of the first, but on the torus b) there are two crossing points between black and gray creases that remain unpatched (blue and red plaquettes still cannot be measured with two labelings); the scenario calls for a third labeling. This figure was preprinted in the Ref. [181].*

4.2. Majorana overlaps and commutation

Consider that two Majorana strings s_A, s_B are composed of substrings s_j, s_m, s_k of length j, m, k, and are ordered as

$$s_A = s_j s_m \ , \qquad s_B = s_m s_k \ , \tag{4.1}$$

i.e. such that the overlapping Majoranas are flushed to the right and left, respectively. This can be done without loss of generality, because this reordering merely costs a certain phase ± 1, and in the end the reordering can be undone, canceling the extra phase. Anticommutation relations imply

$$s_A s_B = s_j s_m s_m s_k = (-1)^{jm+mk+jk} s_m s_k s_j s_m \tag{4.2}$$

$$= (-1)^{(j+m)(k+m)-m^2} s_B s_A \ . \tag{4.3}$$

The two strings commute if, and only if, $(j+m)(k+m) - m^2$ is even. This condition is equivalent to the length of the overlap having the same parity as the product of the string lengths, as in the main text.

Bibliography

[1] A. Einstein, B. Podolsky, and N. Rosen. Can quantum-mechanical description of physical reality be considered complete? *Phys. Rev.*, 47:777–780, 1935.

[2] E. Schrödinger. Discussion of probability relations between separated systems. *Math. Proc. Camb. Philos. Soc.*, 31:555—-563, 1935.

[3] J. S. Bell. On the einstein podolsky rosen paradox. *Phys. Phys. Fiz.*, 1:195–200, 1964.

[4] Alain Aspect. *Bell's Theorem: The Naive View of an Experimentalist*, pages 119–153. Springer Berlin Heidelberg, Berlin, Heidelberg, 2002.

[5] Nicolas Brunner, Daniel Cavalcanti, Stefano Pironio, Valerio Scarani, and Stephanie Wehner. Bell nonlocality. *Rev. Mod. Phys.*, 86:419–478, 2014.

[6] B. Keimer and J. E. Moore. The physics of quantum materials. *Nat. Phys.*, 13:1045–1055, 2017.

[7] Xiao-Gang Wen. Choreographed entanglement dances: Topological states of quantum matter. *Science*, 363:eaal3099, 2019.

[8] Ryszard Horodecki, Paweł Horodecki, Michał Horodecki, and Karol Horodecki. Quantum entanglement. *Rev. Mod. Phys.*, 81:865–942, 2009.

[9] A. Galindo and M. A. Martín-Delgado. Information and computation: Classical and quantum aspects. *Rev. Mod. Phys.*, 74:347–423, 2002.

[10] Antonio Acín, Immanuel Bloch, Harry Buhrman, Tommaso Calarco, Christopher Eichler, Jens Eisert, Daniel Esteve, Nicolas Gisin, Steffen J Glaser, Fedor Jelezko, Stefan Kuhr, Maciej Lewenstein, Max F Riedel, Piet O Schmidt, Rob Thew, Andreas Wallraff, Ian Walmsley, and Frank K Wilhelm. The quantum technologies roadmap: a european community view. *New Journal of Physics*, 20(8):080201, aug 2018.

[11] Daniel Loss and Eugene V. Sukhorukov. Probing entanglement and nonlocality of electrons in a double-dot via transport and noise. *Phys. Rev. Lett.*, 84:1035–1038, 2000.

[12] Nikolai M. Chtchelkatchev, Gianni Blatter, Gordey B. Lesovik, and Thierry Martin. Bell inequalities and entanglement in solid-state devices. *Phys. Rev. B*, 66:161320, 2002.

[13] Shiro Kawabata. Test of bell's inequality using the spin filter effect in ferromagnetic semiconductor microstructures. *J. Phys. Soc. Japan*, 70:1210–1213, 2001.

[14] C. W. J. Beenakker, C. Emary, M. Kindermann, and J. L. van Velsen. Proposal for production and detection of entangled electron-hole pairs in a degenerate electron gas. *Phys. Rev. Lett.*, 91:147901, 2003.

[15] C. W. J. Beenakker, M. Titov, and B. Trauzettel. Optimal spin-entangled electron-hole pair pump. *Phys. Rev. Lett.*, 94:186804, 2005.

[16] W.-R. Hannes and M. Titov. Finite-temperature bell test for quasiparticle entanglement in the fermi sea. *Phys. Rev. B*, 77:115323, 2008.

[17] L. Hofstetter, S. Csonka, J. Nygard, and C. Schönenberger. Cooper pair splitter realized in a two-quantum-dot y-junction. *Nature*, 461:960—963, 2009.

[18] L. G. Herrmann, F. Portier, P. Roche, A. Levy Yeyati, T. Kontos, and C. Strunk. Carbon nanotubes as cooper-pair beam splitters. *Phys. Rev. Lett.*, 104:026801, 2010.

[19] L. Hofstetter, S. Csonka, A. Baumgartner, G. Fülöp, S. d'Hollosy, J. Nygård, and C. Schönenberger. Finite-bias cooper pair splitting. *Phys. Rev. Lett.*, 107:136801, 2011.

[20] Z. B. Tan, D. Cox, T. Nieminen, P. Lähteenmäki, D. Golubev, G. B. Lesovik, and P. J. Hakonen. Cooper pair splitting by means of graphene quantum dots. *Phys. Rev. Lett.*, 114:096602, 2015.

[21] Guido Burkard. Spin-entangled electrons in solid-state systems. *J. Phys.: Condens. Matter*, 19:233202, 2007.

[22] D. Vasilyev, F. O. Schumann, F. Giebels, H. Gollisch, J. Kirschner, and R. Feder. Spin-entanglement between two freely propagating electrons: Experiment and theory. *Phys. Rev. B*, 95:115134, 2017.

[23] Piotr Busz, Damian Tomaszewski, and Jan Martinek. Spin correlation and entanglement detection in cooper pair splitters by current measurements using magnetic detectors. *Phys. Rev. B*, 96:064520, 2017.

[24] Y. Hasegawa, R. Loidl, G. Badurek, M. Baron, and M. Rauch. Violation of a bell-like inequality in single-neutron interferometry. *Nature*, 425:45–48, 2003.

[25] Jürgen Klepp, Stephan Sponar, and Yuji Hasegawa. Fundamental phenomena of quantum mechanics explored with neutron interferometers. *Prog. Theor. Exp. Phys.*, 2014:082A01, 2014.

[26] M Yönaç, Ting Yu, and J. H. Eberly. Pairwise concurrence dynamics: a four-qubit model. *J. Phys. B*, 40:S45–S59, 2007.

[27] S. Adhikari, A. S. Majumdar, Dipankar Home, and A. K. Pan. Swapping path-spin intraparticle entanglement onto spin-spin interparticle entanglement. *EPL (Europhysics Letters)*, 89:10005, 2010.

[28] Yingwen Zhang, Megan Agnew, Thomas Roger, Filippus S. Roux, Thomas Konrad, Daniele Faccio, Jonathan Leach, and Andrew Forbes. Simultaneous entanglement swapping of multiple orbital angular momentum states of light. *Nat. Commun.*, 8:632, 2017.

[29] Asmita Kumari, Abhishek Ghosh, Mohit Lal Bera, and A. K. Pan. Swapping intraphoton entanglement to interphoton entanglement using linear optical devices. *Phys. Rev. A*, 99:032118, Mar 2019.

[30] D. Pesin and A.H. MacDonald. Spintronics and pseudospintronics in graphene and topological insulators. *Nat. Mater.*, 116:409–416, 2012.

[31] Di Xiao, Gui-Bin Liu, Wanxiang Feng, Xiaodong Xu, and Wang Yao. Coupled spin and valley physics in monolayers of mos_2 and other group-vi dichalcogenides. *Phys. Rev. Lett.*, 108:196802, 2012.

[32] John R. Schaibley, Hongyi Yu, Genevieve Clark, Pasqual Rivera, Jason S. Ross, Kyle L. Seyler, Yao Wang, and Xu Xiaodong. Valleytronics in 2d materials. *Nat. Rev. Mater.*, 1:16055, 2016.

[33] K. S. Novoselov, A. Mishchenko, A. Carvalho, and A. H. Castro Neto. 2d materials and van der waals heterostructures. *Science*, 353:aac9439, 2016.

[34] Emmanuel I. Rashba. Graphene with structure-induced spin-orbit coupling: Spin-polarized states, spin zero modes, and quantum hall effect. *Phys. Rev. B*, 79:161409, 2009.

[35] Dinh Van Tuan, Frank Ortmann, David Soriano, S. O. Valenzuela, and Stephan Roche. Pseudospin-driven spin relaxation mechanism in graphene. *Nat. Phys.*, 10:857–863, 2014.

[36] Dinh Van Tuan, Frank Ortmann, Aron W. , David Soriano, and Stephan Roche. Spin dynamics and relaxation in graphene dictated by electron-hole puddles. *Sci. Rep.*, 6:21046, 2016.

[37] Aron W. Cummings and Stephan Roche. Effects of dephasing on spin lifetime in ballistic spin-orbit materials. *Phys. Rev. Lett.*, 116:086602, 2016.

[38] Victor A. S. V. Bittencourt and Alex E. Bernardini. Lattice-layer entanglement in bernal-stacked bilayer graphene. *Phys. Rev. B*, 95:195145, 2017.

[39]

[40] K. S. Novoselov, A. K. Geim, S. V. Morozov, D. Jiang, M. I. Katsnelson, I. V. Grigorieva, S. V. Dubonos, and A. A. Firsov. Two-dimensional gas of massless dirac fermions in graphene. *Nature*, 438(7065):197–200, November 2005.

[41] Yuanbo Zhang, Yan-Wen Tan, Horst L. Stormer, and Philip Kim. Experimental observation of the quantum hall effect and berry's phase in graphene. *Nature*, 438(7065):201–204, nov 2005.

[42] R. R. Nair, P. Blake, A. N. Grigorenko, K. S. Novoselov, T. J. Booth, T. Stauber, N. M. R. Peres, and A. K. Geim. Fine structure constant defines visual transparency of graphene. *Science*, 320(5881):1308–1308, jun 2008.

[43] M. I. Katsnelson, K. S. Novoselov, and A. K. Geim. Chiral tunnelling and the klein paradox in graphene. *Nature Physics*, 2(9):620–625, aug 2006.

[44] Andrea F. Young and Philip Kim. Quantum interference and klein tunnelling in graphene heterojunctions. *Nature Physics*, 5(3):222–226, feb 2009.

[45] A. Oberlin, M. Endo, and T. Koyama. Filamentous growth of carbon through benzene decomposition. *Journal of Crystal Growth*, 32(3):335–349, March 1976.

[46] Melville S. Green. Markoff random processes and the statistical mechanics of time-dependent phenomena. ii. irreversible processes in fluids. *The Journal of Chemical Physics*, 22(3):398–413, 1954.

[47] D. S. Bethune, C. H. Klang, M. S. de Vries, G. Gorman, R. Savoy, J. Vazquez, and R. Beyers. Cobalt-catalysed growth of carbon nanotubes with single-atomic-layer walls. , 363(6430):605–607, June 1993.

[48] Wei Han, Roland K. Kawakami, Martin Gmitra, and Jaroslav Fabian. Graphene spintronics. *Nature Nanotechnology*, 9(10):794–807, oct 2014.

[49] Aires Ferreira, Tatiana G. Rappoport, Miguel A. Cazalilla, and A. H. Castro Neto. Extrinsic spin hall effect induced by resonant skew scattering in graphene. *Phys. Rev. Lett.*, 112:066601, Feb 2014.

[50] A. C. Ferrari, F. Bonaccorso, V. Fal'ko, K. S. Novoselov, S. Roche, P. Bøggild, S. Borini, F. H. L. Koppens, V. Palermo, N. Pugno, et al. Science and technology roadmap for graphene, related two-dimensional crystals, and hybrid systems. *Nanoscale*, 7:4598–4810, 2015.

[51] P. A. M. Dirac. The quantum theory of the electron. II. 118(779):351–361, March 1928.

[52] Luis E. F. Foa Torres, Stephan Roche, and Jean-Christophe Charlier. *Introduction to Graphene-Based Nanomaterials: From Electronic Structure to Quantum Transport*. Cambridge University Press, 2014.

[53] John von Neumann and Eugene Paul Wigner. On the behaviour of eigenvalues in adiabatic processes. 2000.

[54] J. L. Mañes, F. Guinea, and María A. H. Vozmediano. Existence and topological stability of fermi points in multilayered graphene. *Phys. Rev. B*, 75:155424, Apr 2007.

[55] G. Montambaux, F. Piéchon, J.-N. Fuchs, and M. O. Goerbig. Merging of dirac points in a two-dimensional crystal. *Phys. Rev. B*, 80:153412, Oct 2009.

[56] F. D. M. Haldane. Model for a quantum hall effect without landau levels: Condensed-matter realization of the "parity anomaly". *Phys. Rev. Lett.*, 61:2015–2018, Oct 1988.

[57] K. I. Bolotin, K. J. Sikes, Z. Jiang, M. Klima, G. Fudenberg, J. Hone, P. Kim, and H. L. Stormer. Ultrahigh electron mobility in suspended graphene. *Solid State Commun.*, 146(9-10):351–355, jun 2008.

[58] L. Banszerus, M. Schmitz, S. Engels, J. Dauber, M. Oellers, F. Haupt, K. Watanabe, T. Taniguchi, B. Beschoten, and C. Stampfer. Ultrahigh-mobility graphene devices from chemical vapor deposition on reusable copper. *Sci. Adv.*, 1(6):e1500222—-e1500222, jul 2015.

[59] Luca Banszerus, Michael Schmitz, Stephan Engels, Matthias Goldsche, Kenji Watanabe, Takashi Taniguchi, Bernd Beschoten, and Christoph Stampfer. Ballistic Transport Exceeding 28 μm in CVD Grown Graphene. *Nano Lett.*, 16(2):1387–1391, feb 2016.

[60] Hongki Min, J. E. Hill, N. A. Sinitsyn, B. R. Sahu, Leonard Kleinman, and A. H. MacDonald. Intrinsic and rashba spin-orbit interactions in graphene sheets. *Phys. Rev. B - Condens. Matter Mater. Phys.*, 74:165310, Oct 2006.

[61] Daniel Huertas-Hernando, F. Guinea, and Arne Brataas. Spin-orbit coupling in curved graphene, fullerenes, nanotubes, and nanotube caps. *Phys. Rev. B - Condens. Matter Mater. Phys.*, 74:155426, Oct 2006.

[62] M. Gmitra, S. Konschuh, C. Ertler, C. Ambrosch-Draxl, and J. Fabian. Band-structure topologies of graphene: Spin-orbit coupling effects from first principles. *Phys. Rev. B*, 80:235431, 2009.

[63] Sergej Konschuh, Martin Gmitra, and Jaroslav Fabian. Tight-binding theory of the spin-orbit coupling in graphene. *Phys. Rev. B*, 82:245412, 2010.

[64] M. Wojtaszek, I. J. Vera-Marun, E. Whiteway, M. Hilke, and B. J. van Wees. Absence of hyperfine effects in ^{13}c-graphene spin-valve devices. *Phys. Rev. B - Condens. Matter Mater. Phys.*, 89:035417, Jan 2014.

[65] Wei Han, Roland K Kawakami, Martin Gmitra, and Jaroslav Fabian. Graphene spintronics. *Nat. Nanotechnol.*, 9(10):794–807, oct 2014.

[66] Marcos H. D. Guimarães, A. Veligura, P. J. Zomer, T. Maassen, I. J. Vera-Marun, N. Tombros, and B. J. van Wees. Spin transport in high-quality suspended graphene devices. *Nano Lett.*, 12(7):3512–3517, jul 2012.

[67] Marc Drögeler, Frank Volmer, Maik Wolter, Bernat Terrés, Kenji Watanabe, Takashi Taniguchi, Gernot Güntherodt, Christoph Stampfer, and Bernd

Beschoten. Nanosecond spin lifetimes in single- and few-layer graphene-hBN heterostructures at room temperature. *Nano Lett.*, 14(11):6050–6055, nov 2014.

[68] Stephan Roche and Sergio O Valenzuela. Graphene spintronics: puzzling controversies and challenges for spin manipulation. *J. Phys. D. Appl. Phys.*, 47(9):094011, mar 2014.

[69] M. Venkata Kamalakar, Christiaan Groenveld, André Dankert, and Saroj P. Dash. Long distance spin communication in chemical vapour deposited graphene. *Nat. Commun.*, 6:6766, apr 2015.

[70] Marc Drogöler, Christopher Franzen, Frank Volmer, Tobias Pohlmann, Luca Banszerus, Maik Wolter, Kenji Watanabe, Takashi Taniguchi, Christoph Stampfer, and Bernd Beschoten. Spin Lifetimes Exceeding 12 ns in Graphene Nonlocal Spin Valve Devices. *Nano Lett.*, 16(6):3533–3539, jun 2016.

[71] Stephan Roche, Johan Åkerman, Bernd Beschoten, Jean-Christophe Charlier, Mairbek Chshiev, Saroj Prasad Dash, Bruno Dlubak, Jaroslav Fabian, Albert Fert, Marcos Guimarães, Francisco Guinea, Irina Grigorieva, Christian Schönenberger, Pierre Seneor, Christoph Stampfer, Sergio O Valenzuela, Xavier Waintal, and Bart J. van Wees. Graphene spintronics: the European Flagship perspective. *2D Mater.*, 2(3):30202, jul 2015.

[72] Jayakumar Balakrishnan, Gavin Kok Wai Koon, Ahmet Avsar, Yuda Ho, Jong Hak Lee, Manu Jaiswal, Seung-Jae Baeck, Jong-Hyun Ahn, Aires Ferreira, Miguel A. Cazalilla, Antonio H. Castro Neto, and Barbaros Özyilmaz. Giant spin Hall effect in graphene grown by chemical vapour deposition. *Nat. Commun.*, 5:4748, sep 2014.

[73] A. Avsar, J. Y. Tan, T. Taychatanapat, J. Balakrishnan, G.K.W. K W Koon, Y. Yeo, J. Lahiri, A. Carvalho, A. S. Rodin, E C T O'Farrell, G. Eda, A. H. Castro Neto, B. Özyilmaz, E.C.T. O'Farrell, G. Eda, A. H. Castro Neto, and B. Özyilmaz. Spin–orbit proximity effect in graphene. *Nat. Commun.*, 5:4875, sep 2014.

[74] Ahmet Avsar, Jong Hak Lee, Gavin Kok Wai Koon, and Barbaros Özyilmaz. Enhanced spin–orbit coupling in dilute fluorinated graphene. *2D Mater.*, 2(4):044009, nov 2015.

[75] E. C.T. T O'Farrell, A Avsar, J Y Tan, G Eda, and B. Özyilmaz. Quantum Transport Detected by Strong Proximity Interaction at a Graphene-WS<inf>2</inf>van der Waals Interface. *Nano Lett.*, 15(9):5682–5688, 2015.

[76] Zhe Wang, Dong–Keun Ki, Hua Chen, Helmuth Berger, Allan H. MacDonald, and Alberto F. Morpurgo. Strong interface-induced spin–orbit interaction in graphene on WS2. *Nat. Commun.*, 6:8339, sep 2015.

[77] J. B.S. Mendes, O. Alves Santos, L. M. Meireles, R. G. Lacerda, L. H. Vilela-Leão, F. L.A. Machado, R. L. Rodríguez-Suárez, A. Azevedo, and S. M. Rezende. Spin-Current to Charge-Current Conversion and Magnetoresistance in a Hybrid Structure of Graphene and Yttrium Iron Garnet. *Phys. Rev. Lett.*, 115(22):226601, nov 2015.

[78] Zhe Wang, Dong-Keun Keun Ki, Jun Yong Khoo, Diego Mauro, Helmuth Berger, Leonid S Levitov, and Alberto F Morpurgo. Origin and Magnitude of 'Designer' Spin-Orbit Interaction in Graphene on Semiconducting Transition Metal Dichalcogenides. *Phys. Rev. X*, 6(4):041020, oct 2016.

[79] André Dankert and Saroj P. Dash. Electrical gate control of spin current in van der Waals heterostructures at room temperature. *Nat. Commun.*, 8:16093, jul 2017.

[80] Bowen Yang, Mark Lohmann, David Barroso, Ingrid Liao, Zhisheng Lin, Yawen Liu, Ludwig Bartels, Kenji Watanabe, Takashi Taniguchi, and Jing Shi. Strong electron-hole symmetric Rashba spin-orbit coupling in graphene/monolayer transition metal dichalcogenide heterostructures. *Phys. Rev. B - Condens. Matter Mater. Phys.*, 96(4):041409, jul 2017.

[81] Alessandro Cresti, Dinh Van Tuan, David Soriano, Aron W Cummings, and Stephan Roche. Multiple quantum phases in graphene with enhanced spin-orbit coupling: From the quantum spin hall regime to the spin hall effect and a robust metallic state. *Phys. Rev. Lett.*, 113(24):246603, 2014.

[82] A Cresti, B K Nikolíc, J H Garćia, and S Roche. Charge, spin and valley Hall effects in disordered grapheme. *Riv. Nuovo Cim.*, 39(12):587–667, 2016.

[83] Wenjing Yan, Oihana Txoperena, Roger Llopis, Hanan Dery, Luis E. Hueso, and Fèlix Casanova. A two-dimensional spin field-effect switch. *Nat. Commun.*, 7:13372, nov 2016.

[84] Phong Tien Vo, Niels R Walet, and Francisco Guinea. Effective interactions in a graphene layer induced by the proximity to a ferromagnet. *2D Mater.*, dec 2017.

[85] A Dyrdał and J Barnaś. Anomalous, spin, and valley Hall effects in graphene deposited on ferromagnetic substrates. *2D Mater.*, 4(3):034003, jul 2017.

[86] C L Kane and E J Mele. Quantum Spin Hall Effect in Graphene. *Phys. Rev. Lett.*, 95(22):226801, 2005.

[87] Jairo Sinova, Sergio O Valenzuela, J Wunderlich, C H Back, and T Jungwirth. Spin Hall effects. *Rev. Mod. Phys.*, 87(4):1213–1260, 2015.

[88] Dinh van Tuan. *Charge and Spin Transport in Disordered Graphene-Based Materials*. Springer International Publishing, 2016.

[89] L. H. Thomas. *Nature*, **117**:514, 1926.

[90] Z. Qiao, H. Jiang, X. Li, Y. Yao, and Qian Niu. *Phys. Rev. B*, **85**:115439, 2012.

[91] Emmanuel I. Rashba. *Phys. Rev. B*, **79**:161409(R), 2009.

[92] Dinh Van Tuan and Stephan Roche. Spin manipulation in graphene by chemically induced pseudospin polarization. *Phys. Rev. Lett.*, 116:106601, 2016.

[93] Christian Ertler, Sergej Konschuh, Martin Gmitra, and Jaroslav Fabian. Electron spin relaxation in graphene: The role of the substrate. *Phys. Rev. B*, 80:041405, 2009.

[94] Hongki Min, J. E. Hill, N. A. Sinitsyn, B. R. Sahu, Leonard Kleinman, and A. H. MacDonald. Intrinsic and rashba spin-orbit interactions in graphene sheets. *Phys. Rev. B*, 74:165310, 2006.

[95] Yugui Yao, Fei Ye, Xiao-Liang Qi, Shou-Cheng Zhang, and Zhong Fang. Spin-orbit gap of graphene: First-principles calculations. *Phys. Rev. B*, 75:041401, 2007.

[96] J. C. Boettger and S. B. Trickey. *Phys. Rev. B*, **75**:121402(R), 2007.

[97] Christian R. Ast and Isabella Gierz. *Phys. Rev. B*, **86**:085105, 2012.

[98] Emmanuel I. Rashba. Graphene with structure-induced spin-orbit coupling: Spin-polarized states, spin zero modes, and quantum hall effect. *Phys. Rev. B*, 79:161409, 2009.

[99] H. Ochoa, A. H. Castro Neto, and F. Guinea. Elliot-yafet mechanism in graphene. *Phys. Rev. Lett.*, 108(20):206808, May 2012.

[100] *2D Materials: Properties and Devices*. Cambridge University Press, 2017.

[101] P. Zhang and M.W. Wu. Electron spin relaxation in graphene with random rashba field: comparison of the d'yakonov–perel' and elliott–yafet-like mechanisms. *New Journal of Physics*, 14(3):033015, 2012.

[102] Taro Wakamura, Francesco Reale, Pawel Palczynski, Sophie Guéron, Cecilia Mattevi, and Hélène Bouchiat. Strong Spin-Orbit Interaction Induced in Graphene by Monolayer WS$_2$. *ArXiv:1710.07483*, 2017.

[103] Bowen Yang, Min-Feng Tu, Jeongwoo Kim, Yong Wu, Hui Wang, Jason Alicea, Ruqian Wu, Marc Bockrath, and Jing Shi. Tunable spin-orbit coupling and symmetry-protected edge states in graphene/WS$_2$. *2D Mater.*, 3(3):31012, sep 2016.

[104] Talieh S Ghiasi, Josep Ingla-Aynés, Alexey A Kaverzin, and Bart J. van Wees. Large Proximity-Induced Spin Lifetime Anisotropy in Transition-Metal Dichalcogenide/Graphene Heterostructures. *Nano Lett.*, nov 2017.

[105] L Antonio Benítez, Juan F Sierra, Williams Savero Torres, Aloïs Arrighi, Frédéric Bonell, Marius V Costache, and Sergio O Valenzuela. Strongly anisotropic spin relaxation in graphene–transition metal dichalcogenide heterostructures at room temperature. *Nat. Phys.*, dec 2017.

[106] Simon Zihlmann, Aron W Cummings, Jose H Garcia, Kenji Watanabe, Takashi Taniguchi, Christian Schönenberger, and Péter Makk. Large spin relaxation anisotropy and valley-Zeeman spin-orbit coupling in WSe$_2$/Gr/hBN heterostructures. *Prep.*

[107] E. McCann, K. Kechedzhi, Vladimir I. Fal'ko, H. Suzuura, T. Ando, and B. L. Altshuler. Weak-Localization Magnetoresistance and Valley Symmetry in Graphene. *Phys. Rev. Lett.*, 97(14):146805, oct 2006.

[108] Dinh Van Tuan, J M Marmolejo-Tejada, Xavier Waintal, Branislav K. Nikolic, and Stephan Roche. Spin Hall Effect and Nonlocal Resistance in Chemically Functionalized Graphene. *Phys. Rev. Lett.*, 117(October):176602, 2016.

[109] Mário Ribeiro, Stephen R. Power, Stephan Roche, Luis. E. Hueso, and Fèlix Casanova. Scale-invariant large nonlocality in CVD graphene. *ArXiv:1706.02539*, 2017.

[110] J. M. Marmolejo-Tejada, J. H. García, P. H. Chang, X. L. Sheng, A. Cresti, S. Roche, and B. K. Nikolic. Origin of nonlocal resistance in multiterminal graphene on hexagonal-boron-nitride: Fermi surface edge states or Fermi sea topological valley currents. *ArXiv:1706.09361*, 2017.

[111] Edward McCann, Vladimir I. Fal'ko, Vladimir I Fal'ko, K Kechedzhi, Vladimir I. Fal'ko, H Suzuura, T Ando, B L Altshuler, and Vladimir I Fal'ko. z->-z Symmetry of Spin-Orbit Coupling and Weak Localization in Graphene. *Phys. Rev. Lett.*, 108(16):166606, apr 2012.

[112] Yilin Wang, Xinghan Cai, Janice Reutt-Robey, and Michael S. Fuhrer. Neutral-current Hall effects in disordered graphene. *Phys. Rev. B - Condens. Matter Mater. Phys.*, 92(16):161411, oct 2015.

[113] Martin Gmitra, Denis Kochan, Petra Högl, and Jaroslav Fabian. Trivial and inverted bands and the emergence of quantum spin hall states in graphene on transition-metal dichalcogenides. *Phys. Rev. B*, 93:155104, 2016.

[114] Abdulrhman M Alsharari, Mahmoud M Asmar, and Sergio E Ulloa. Mass inversion in graphene by proximity to dichalcogenide monolayer. *Phys. Rev. B - Condens. Matter Mater. Phys.*, 94(24):241106, dec 2016.

[115] Aron W Cummings, Jose H. Garcia, Jaroslav Fabian, and Stephan Roche. Giant Spin Lifetime Anisotropy in Graphene Induced by Proximity Effects. *Phys. Rev. Lett.*, 119(20):206601, nov 2017.

[116] Denis Kochan, Susanne Irmer, and Jaroslav Fabian. Model spin-orbit coupling Hamiltonians for graphene systems. *Phys. Rev. B - Condens. Matter Mater. Phys.*, 95(16):165415, apr 2017.

[117] Yu A Bychkov and E I Rashba. Oscillatory effects and the magnetic susceptibility of carriers in inversion layers. *J. Phys. C Solid State Phys.*, 17(33):6039–6045, 1984.

[118] Klaus Zollner, Aron W. Cummings, Stephan Roche, and Jaroslav Fabian. Graphene on two-dimensional hexagonal bn, aln, and gan: Electronic, spin-orbit, and spin relaxation properties. *Phys. Rev. B*, 103:075129, Feb 2021.

[119] N. Gisin. Bell's inequality holds for all non-product states. *Physics Letters A*, 154(5):201–202, 1991.

[120] Sandu Popescu and Daniel Rohrlich. Generic quantum nonlocality. *Physics Letters A*, 166(5):293–297, 1992.

[121] B. S. Cirel'Son. Quantum generalizations of Bell's inequality. *Letters in Mathematical Physics*, 4(2):93–100, March 1980.

[122] William K. Wootters. Entanglement of formation of an arbitrary state of two qubits. *Phys. Rev. Lett.*, 80:2245–2248, 1998.

[123] Scott Hill and William K. Wootters. Entanglement of a pair of quantum bits. *Phys. Rev. Lett.*, 78:5022–5025, Jun 1997.

[124] Charles H. Bennett, Gilles Brassard, Sandu Popescu, Benjamin Schumacher, John A. Smolin, and William K. Wootters. Purification of noisy entanglement and faithful teleportation via noisy channels. *Phys. Rev. Lett.*, 76:722–725, Jan 1996.

[125] Charles H. Bennett, Gilles Brassard, Claude Crépeau, Richard Jozsa, Asher Peres, and William K. Wootters. Teleporting an unknown quantum state via dual classical and einstein-podolsky-rosen channels. *Phys. Rev. Lett.*, 70:1895–1899, 1993.

[126] Zhi-Hao Ma, Zhi-Hua Chen, Jing-Ling Chen, Christoph Spengler, Andreas Gabriel, and Marcus Huber. Measure of genuine multipartite entanglement with computable lower bounds. *Phys. Rev. A*, 83:062325, 2011.

[127] Klaus Zollner, Martin Gmitra, and Jaroslav Fabian. Heterostructures of graphene and hbn: Electronic, spin-orbit, and spin relaxation properties from first principles. *Phys. Rev. B*, 99:125151, 2019.

[128] Bruna Gabrielly de Moraes, Aron W. Cummings, and Stephan Roche. Emergence of intraparticle entanglement and time-varying violation of bell's inequality in dirac matter. *Physical Review B*, 102(4), jul 2020.

[129] Karol Życzkowski, Karol A. Penson, Ion Nechita, and Benoît Collins. Generating random density matrices. *Journal of Mathematical Physics*, 52(6):062201, 2011.

[130] Alexandre Roulet and Christoph Bruder. Quantum synchronization and entanglement generation. *Phys. Rev. Lett.*, 121:063601, 2018.

[131] Karol Zyczkowski and Hans-Jürgen Sommers. Induced measures in the space of mixed quantum states. *J. Phys. A: Math. Gen.*, 34:7111–7125, 2001.

[132] John F. Clauser, Michael A. Horne, Abner Shimony, and Richard A. Holt. Proposed experiment to test local hidden-variable theories. *Phys. Rev. Lett.*, 23:880–884, 1969.

[133] Frank Verstraete and Michael M. Wolf. Entanglement versus bell violations and their behavior under local filtering operations. *Phys. Rev. Lett.*, 89:170401, 2002.

[134] Frank Arute et al. Quantum supremacy using a programmable superconducting processor. *Nature*, 574(7779):505–510, oct 2019.

[135] Julian Kelly, Zijun Chen, Ben Chiaro, Brooks Foxen, and John M. Martinis. Operating and characterizing a 72 superconducting qubit processor "Bristlecone". In *APS Meeting Abstracts*, 2019.

[136] Frank Arute et al. Hartree-Fock on a superconducting qubit quantum computer. *Science*, 369(6507):1084–1089, aug 2020.

[137] Yulin Wu, Wan-Su Bao, Sirui Cao, Fusheng Chen, Ming-Cheng Chen, Xiawei Chen, Tung-Hsun Chung, Hui Deng, Yajie Du, Daojin Fan, Ming Gong, Cheng Guo, Chu Guo, Shaojun Guo, Lianchen Han, Linyin Hong, He-Liang Huang, Yong-Heng Huo, Liping Li, Na Li, Shaowei Li, Yuan Li, Futian Liang, Chun Lin, Jin Lin, Haoran Qian, Dan Qiao, Hao Rong, Hong Su, Lihua Sun, Liangyuan Wang, Shiyu Wang, Dachao Wu, Yu Xu, Kai Yan, Weifeng Yang, Yang Yang, Yangsen Ye, Jianghan Yin, Chong Ying, Jiale Yu, Chen Zha, Cha Zhang, Haibin Zhang, Kaili Zhang, Yiming Zhang, Han Zhao, Youwei Zhao, Liang Zhou, Qingling Zhu, Chao-Yang Lu, Cheng-Zhi Peng, Xiaobo Zhu, and Jian-Wei Pan. Strong quantum computational advantage using a superconducting quantum processor. *Physical Review Letters*, 127(18):180501, October 2021.

[138] Adrian Cho. IBM promises 1000-qubit quantum computer—a milestone—by 2023. *Science (New York, N.Y.)*, September 2020.

[139] Han-Sen Zhong et al. Quantum computational advantage using photons. *Science*, 370(6523):1460–1463, dec 2020.

[140] Han-Sen Zhong, Yu-Hao Deng, Jian Qin, Hui Wang, Ming-Cheng Chen, Li-Chao Peng, Yi-Han Luo, Dian Wu, Si-Qiu Gong, Hao Su, Yi Hu, Peng Hu, Xiao-Yan Yang, Wei-Jun Zhang, Hao Li, Yuxuan Li, Xiao Jiang, Lin Gan, Guangwen Yang, Lixing You, Zhen Wang, Li Li, Nai-Le Liu, Jelmer J. Renema, Chao-Yang Lu, and Jian-Wei Pan. Phase-programmable gaussian boson sampling using

stimulated squeezed light. *Physical Review Letters*, 127(18):180502, October 2021.

[141] Joseph W. Britton, Brian C. Sawyer, Adam C. Keith, C.-C. Joseph Wang, James K. Freericks, Hermann Uys, Michael J. Biercuk, and John J. Bollinger. Engineered two-dimensional Ising interactions in a trapped-ion quantum simulator with hundreds of spins. *Nature*, 484(7395):489–492, April 2012.

[142] Catherine McGeoch and Pau Farré. The advantage system: Performance update. Technical report, D-Wave Systems, Inc., 2021.

[143] Chao Song, Kai Xu, Wuxin Liu, Chui-ping Yang, Shi-Biao Zheng, Hui Deng, Qiwei Xie, Keqiang Huang, Qiujiang Guo, Libo Zhang, Pengfei Zhang, Da Xu, Dongning Zheng, Xiaobo Zhu, H. Wang, Y.-A. Chen, C.-Y. Lu, Siyuan Han, and Jian-Wei Pan. 10-Qubit entanglement and parallel logic operations with a superconducting circuit. *Physical Review Letters*, 119(18):180511, November 2017.

[144] Marcus Cramer, Martin B. Plenio, Steven T. Flammia, Rolando Somma, David Gross, Stephen D. Bartlett, Olivier Landon-Cardinal, David Poulin, and Yi-Kai Liu. Efficient quantum state tomography. *Nature Communications*, 1(1):149, December 2010.

[145] B. P. Lanyon, C. Maier, M. Holzäpfel, T. Baumgratz, C. Hempel, P. Jurcevic, I. Dhand, A. S. Buyskikh, A. J. Daley, M. Cramer, M. B. Plenio, R. Blatt, and C. F. Roos. Efficient tomography of a quantum many-body system. *Nature Physics*, 13(12):1158–1162, December 2017.

[146] Giacomo Torlai, Guglielmo Mazzola, Juan Carrasquilla, Matthias Troyer, Roger Melko, and Giuseppe Carleo. Neural-network quantum state tomography. *Nature Physics*, 14(5):447–450, May 2018.

[147] Juan Carrasquilla, Giacomo Torlai, Roger G. Melko, and Leandro Aolita. Reconstructing quantum states with generative models. *Nature Machine Intelligence*, 1(3):155–161, March 2019.

[148] Scott E. Smart and David A. Mazziotti. Lowering tomography costs in quantum simulation with a symmetry projected operator basis. *Physical Review A*, 103(1):012420, January 2021.

[149] Scott Aaronson. Shadow tomography of quantum states. In *Proceedings of the 50th Annual ACM SIGACT Symposium on Theory of Computing*, pages 325–338, New York, NY, USA, June 2018. ACM.

[150] Fernando G. S. L. Brandão, Amir Kalev, Tongyang Li, Cedric Yen-Yu Lin, Krysta M. Svore, and Xiaodi Wu. Quantum SDP Solvers: Large Speed-ups, Optimality, and Applications to Quantum Learning, April 2019.

[151] Hsin-Yuan Yuan Huang, Richard Kueng, and John Preskill. Predicting many properties of a quantum system from very few measurements. *Nature Physics*, 16(10):1050–1057, October 2020.

[152] Sitan Chen, Jordan Cotler, Hsin-Yuan Huang, and Jerry Li. Exponential separations between learning with and without quantum memory, November 2021.

[153] Géza Tóth, Christian Knapp, Otfried Gühne, and Hans J. Briegel. Optimal spin squeezing inequalities detect bound entanglement in spin models. *Physical Review Letters*, 99(25):250405, December 2007.

[154] Géza Tóth, Christian Knapp, Otfried Gühne, and Hans J. Briegel. Spin squeezing and entanglement. *Physical Review A*, 79(4):042334, April 2009.

[155] J. Tura, R. Augusiak, A. B. Sainz, T. Vértesi, M. Lewenstein, and A. Acín. Detecting nonlocality in many-body quantum states. *Science (New York, N.Y.)*, 344(6189):1256–1258, June 2014.

[156] Jordan Cotler and Frank Wilczek. Quantum overlapping tomography. *Physical Review Letters*, 124(10):100401, March 2020.

[157] Xavier Bonet-Monroig, Ryan Babbush, and Thomas E. O'Brien. Nearly optimal measurement scheduling for partial tomography of quantum states. *Physical Review X*, 10(3):031064, September 2020.

[158] Wassily Hoeffding. Probability inequalities for sums of bounded random variables. *Journal of the American Statistical Association*, 58(301):13–30, 1963.

[159] Herman Chernoff. A Measure of Asymptotic Efficiency for Tests of a Hypothesis Based on the sum of Observations. *The Annals of Mathematical Statistics*, 23(4):493 – 507, 1952.

[160] Nengkun Yu. Quantum closeness testing: A streaming algorithm and applications, April 2019.

[161] Guillermo García-Pérez, Matteo A. C. Rossi, Boris Sokolov, Elsi-Mari Borrelli, and Sabrina Maniscalco. Pairwise tomography networks for many-body quantum systems. *Physical Review Research*, 2(2):023393, June 2020.

[162] Tim J. Evans, Robin Harper, and Steven T. Flammia. Scalable bayesian hamiltonian learning, December 2019.

[163] Jules Tilly, P. V. Sriluckshmy, Akashkumar Patel, Enrico Fontana, Ivan Rungger, Edward Grant, Robert Anderson, Jonathan Tennyson, and George H. Booth. Reduced density matrix sampling: Self-consistent embedding and multiscale electronic structure on current generation quantum computers. *Physical Review Research*, 3(3):033230, September 2021.

[164] Zhang Jiang, Amir Kalev, Wojciech Mruczkiewicz, and Hartmut Neven. Optimal fermion-to-qubit mapping via ternary trees with applications to reduced quantum states learning. *Quantum*, 4:276, June 2020.

[165] Andrew Zhao, Nicholas C. Rubin, and Akimasa Miyake. Fermionic partial tomography via classical shadows. *Physical Review Letters*, 127(11):110504, September 2021.

[166] Colin D. Bruzewicz, John Chiaverini, Robert McConnell, and Jeremy M. Sage. Trapped-ion quantum computing: Progress and challenges. *Applied Physics Reviews*, 6(2):021314, June 2019.

[167] T. Hensgens, T. Fujita, L. Janssen, Xiao Li, C. J. Van Diepen, C. Reichl, W. Wegscheider, S. Das Sarma, and L. M. K. Vandersypen. Quantum simulation of a Fermi–Hubbard model using a semiconductor quantum dot array. *Nature*, 548(7665):70–73, August 2017.

[168] A. Singha, M. Gibertini, B. Karmakar, S. Yuan, M. Polini, G. Vignale, M. I. Katsnelson, A. Pinczuk, L. N. Pfeiffer, K. W. West, and V. Pellegrini. Two-dimensional mott-hubbard electrons in an artificial honeycomb lattice. *Science (New York, N.Y.)*, 332(6034):1176–1179, June 2011.

[169] Nicholas C. Rubin, Ryan Babbush, and Jarrod McClean. Application of fermionic marginal constraints to hybrid quantum algorithms. *New Journal of Physics*, 20(5):053020, May 2018.

[170] Sergey B. Bravyi and Alexei Yu. Kitaev. Fermionic quantum computation. *Annals of Physics*, 298(1):210–226, May 2002.

[171] G. Vidal, J. I. Latorre, E. Rico, and A. Kitaev. Entanglement in quantum critical phenomena. *Physical Review Letters*, 90(22):227902, June 2003.

[172] Christina V. Kraus. *A Quantum Information Perspective of Fermionic Quantum Many-Body Systems*. PhD thesis, Technische Universität München, 2009.

[173] P. Jordan and E. Wigner. über das paulische äquivalenzverbot. *Zeitschrift für Physik*, 47(9-10):631–651, September 1928.

[174] F. Verstraete and J. I. Cirac. Mapping local Hamiltonians of fermions to local Hamiltonians of spins. *Journal of Statistical Mechanics: Theory and Experiment*, 2005(09):P09012–P09012, September 2005.

[175] Masatoshi Imada, Atsushi Fujimori, and Yoshinori Tokura. Metal-insulator transitions. *Reviews of Modern Physics*, 70(4):1039–1263, October 1998.

[176] Robert Jördens, Niels Strohmaier, Kenneth Günter, Henning Moritz, and Tilman Esslinger. A Mott insulator of fermionic atoms in an optical lattice. *Nature*, 455(7210):204–207, September 2008.

[177] Norbert Schuch and Bela Bauer. Matrix product state algorithms for Gaussian fermionic states. *Physical Review B*, 100(24):245121, December 2019.

[178] Thomas Durt, Christian Kurtsiefer, Antia Lamas-Linares, and Alexander Ling. Wigner tomography of two-qubit states and quantum cryptography. *Physical Review A*, 78(4):042338, October 2008.

[179] Z. E. D. Medendorp, F. A. Torres-Ruiz, L. K. Shalm, G. N. M. Tabia, C. A. Fuchs, and A. M. Steinberg. Experimental characterization of qutrits using symmetric informationally complete positive operator-valued measurements. *Physical Review A*, 83(5):051801, May 2011.

[180] Zhibo Hou, Jun-Feng Tang, Jiangwei Shang, Huangjun Zhu, Jian Li, Yuan Yuan, Kang-Da Wu, Guo-Yong Xiang, Chuan-Feng Li, and Guang-Can Guo. Deterministic realization of collective measurements via photonic quantum walks. *Nature Communications*, 9(1):1414, December 2018.

[181] Bruna G. M. Araújo, Márcio M. Taddei, Daniel Cavalcanti, and Antonio Acín. Local quantum overlapping tomography, 2021.

[182] Marek Kubale, editor. *Graph Colorings*, volume 352 of *Contemporary Mathematics*. American Mathematical Society, Providence, Rhode Island, 2004.

[183] Lowell W. Beineke and Robin J. Wilson, editors. *Topics in Chromatic Graph Theory*. Cambridge University Press, Cambridge, 2015.

[184] Vadim. G. Vizing. On an estimate of the chromatic class of a p-graph. *Diskret. Analiz.*, 3:25–30, 1964.

[185] Michael Stiebitz, Diego Scheide, Bjarne Toft, and Lene M. Favrholdt. *Graph Edge Coloring: Vizing's Theorem and Goldberg's Conjecture*. Wiley, Hoboken, 2012.

[186] Frank Arute et al. Quantum supremacy using a programmable superconducting processor. *Nature*, 574(7779):505–510, Oct 2019.

[187] Han-Sen Zhong, Hui Wang, Yu-Hao Deng, Ming-Cheng Chen, Li-Chao Peng, Yi-Han Luo, Jian Qin, Dian Wu, Xing Ding, Yi Hu, et al. Quantum computational advantage using photons. *Science*, 370(6523):1460–1463, 2020.

[188] Lov K. Grover. A fast quantum mechanical algorithm for database search. In *Proceedings of the twenty-eighth annual ACM symposium on Theory of computing - STOC '96*. ACM Press, 1996.

[189] Peter W. Shor. Polynomial-time algorithms for prime factorization and discrete logarithms on a quantum computer. *SIAM Journal on Computing*, 26(5):1484–1509, October 1997.

[190] Gilles Brassard, Peter Høyer, Michele Mosca, and Alain Tapp. Quantum amplitude amplification and estimation. pages 53–74, 2002.

[191] Alberto Peruzzo, Jarrod McClean, Peter Shadbolt, Man-Hong Yung, Xiao-Qi Zhou, Peter J. Love, Alán Aspuru-Guzik, and Jeremy L. O'Brien. A variational eigenvalue solver on a photonic quantum processor. *Nature Communications*, 5(1), July 2014.

[192] Edward Farhi, Jeffrey Goldstone, and Sam Gutmann. A quantum approximate optimization algorithm, 2014.

[193] Marcos Lopez de Prado. Generalized optimal trading trajectories: A financial quantum computing application. *SSRN Electronic Journal*, 2015.

[194] Gili Rosenberg, Poya Haghnegahdar, Phil Goddard, Peter Carr, Kesheng Wu, and Marcos Lopez de Prado. Solving the optimal trading trajectory problem using a quantum annealer. *IEEE Journal of Selected Topics in Signal Processing*, 10(6):1053–1060, Sep 2016.

[195] Nikolaj Moll et al. Quantum optimization using variational algorithms on near-term quantum devices. *Quantum Science and Technology*, 3(3):030503, Jun 2018.

[196] Patrick Rebentrost, Masoud Mohseni, and Seth Lloyd. Quantum support vector machine for big data classification. *Physical Review Letters*, 113(13):130503, Sep 2014.

[197] Yunchao Liu, Srinivasan Arunachalam, and Kristan Temme. A rigorous and robust quantum speed-up in supervised machine learning. *Nature Physics*, 17:1013–1017, July 2021.

[198] Maria Schuld, Alex Bocharov, Krysta M. Svore, and Nathan Wiebe. Circuit-centric quantum classifiers. *Physical Review A*, 101(3), March 2020.

[199] Adrián Pérez-Salinas, Alba Cervera-Lierta, Elies Gil-Fuster, and José I. Latorre. Data re-uploading for a universal quantum classifier. *Quantum*, 4:226, February 2020.

[200] Edward Farhi and Hartmut Neven. Classification with quantum neural networks on near term processors, 2018.

[201] Sonika Johri, Shantanu Debnath, Iordanis Kerenidis, et al. Nearest centroid classification on a trapped ion quantum computer, 2020.

[202] Vojtěch Havlíček, Antonio D. Córcoles, Kristan Temme, Aram W. Harrow, Abhinav Kandala, Jerry M. Chow, and Jay M. Gambetta. Supervised learning with quantum-enhanced feature spaces. *Nature*, 567(7747):209–212, March 2019.

[203] J. Ignacio Cirac and Peter Zoller. Goals and opportunities in quantum simulation. *Nature Physics*, 8(4):264–266, April 2012.

[204] Andrew M. Childs, Dmitri Maslov, Yunseong Nam, Neil J. Ross, and Yuan Su. Toward the first quantum simulation with quantum speedup. *Proceedings of the National Academy of Sciences*, 115(38):9456–9461, September 2018.

[205] I. M. Georgescu, S. Ashhab, and Franco Nori. Quantum simulation. *Reviews of Modern Physics*, 86(1):153–185, March 2014.

[206] Richard P. Feynman. Simulating physics with computers. *International Journal of Theoretical Physics*, 21(6-7):467–488, June 1982.

[207] Sam McArdle, Suguru Endo, Alán Aspuru-Guzik, Simon C. Benjamin, and Xiao Yuan. Quantum computational chemistry. *Rev. Mod. Phys.*, 92:015003, Mar 2020.

[208] Abhinav Kandala, Antonio Mezzacapo, Kristan Temme, Maika Takita, Markus Brink, Jerry M. Chow, and Jay M. Gambetta. Hardware-efficient variational quantum eigensolver for small molecules and quantum magnets. *Nature*, 549(7671):242–246, September 2017.

[209] Cornelius Hempel, Christine Maier, Jonathan Romero, Jarrod McClean, Thomas Monz, Heng Shen, Petar Jurcevic, Ben P. Lanyon, Peter Love, Ryan Babbush, Alán Aspuru-Guzik, Rainer Blatt, and Christian F. Roos. Quantum chemistry calculations on a trapped-ion quantum simulator. *Physical Review X*, 8(3), July 2018.

[210] Yunseong Nam, Jwo-Sy Chen, Jungsang Kim, et al. Ground-state energy estimation of the water molecule on a trapped-ion quantum computer. *npj Quantum Information*, 6(1), April 2020.

[211] P. J. J. O'Malley et al. Scalable quantum simulation of molecular energies. *Physical Review X*, 6(3), July 2016.

[212] Philipp Frey and Stephan Rachel. Realization of a discrete time crystal on 57 qubits of a quantum computer, 2022.

[213] S. I. Doronin, E. B. Fel'dman, E. I. Kuznetsova, and A. I. Zenchuk. Simulation of multiple-quantum nmr dynamics of spin dimer on quantum computer, 2021.

[214] Hsin-Yuan (Robert) Huang, Michael Blythe Broughton, Jordan Cotler, Sitan Chen, Jerry Li, Masoud Mohseni, Hartmut Neven, Ryan Babbush, Richard Kueng, John Preskill, and Jarrod Ryan McClean. Demonstrating quantum advantage in learning from experiments. 2021.

[215] Hsin-Yuan Huang, Michael Broughton, Masoud Mohseni, Ryan Babbush, Sergio Boixo, Hartmut Neven, and Jarrod R. McClean. Power of data in quantum machine learning. *Nature Communications*, 12(1), May 2021.

[216] Tosio Kato. On the adiabatic theorem of quantum mechanics. *Journal of the Physical Society of Japan*, 5(6):435–439, November 1950.

[217] Tameem Albash and Daniel A. Lidar. Adiabatic quantum computation. *Reviews of Modern Physics*, 90(1), January 2018.

[218] A. K. Geim and K. S. Novoselov. The rise of graphene. *Nature Materials*, 6(3):183–191, March 2007.

[219] Haoxin Zhou, Tian Xie, Takashi Taniguchi, Kenji Watanabe, and Andrea F. Young. Superconductivity in rhombohedral trilayer graphene. *Nature*, 598(7881):434–438, September 2021.

[220] K. S. Novoselov, A. K. Geim, S. V. Morozov, D. Jiang, Y. Zhang, S. V. Dubonos, I. V. Grigorieva, and A. A. Firsov. Electric field effect in atomically thin carbon films. *Science*, 306(5696):666–669, October 2004.

[221] Belal G. Nassef, Galal A. Nassef, and Mohamed A. Daha. Graphene and its industrial applications c a review. *International Journal of Materials Engineering*, 10(1):1–12, February 2020.

[222] Marco Gibertini, Achintya Singha, Vittorio Pellegrini, Marco Polini, Giovanni Vignale, Aron Pinczuk, Loren N. Pfeiffer, and Ken W. West. Engineering artificial graphene in a two-dimensional electron gas. *Physical Review B*, 79(24), June 2009.

[223] J. Hubbard. Electron correlations in narrow energy bands. *Proceedings of the Royal Society of London. Series A. Mathematical and Physical Sciences*, 276(1365):238–257, November 1963.

[224] Steven R. White. Density-matrix algorithms for quantum renormalization groups. *Physical Review B*, 48(14):10345–10356, October 1993.

[225] Ulrich Schollwöck. The density-matrix renormalization group in the age of matrix product states. *Annals of Physics*, 326(1):96–192, January 2011.

[226] Chris Cade, Lana Mineh, Ashley Montanaro, and Stasja Stanisic. Strategies for solving the fermi-hubbard model on near-term quantum computers. *Phys. Rev. B*, 102:235122, Dec 2020.

[227] Zhang Jiang, Kevin J. Sung, Kostyantyn Kechedzhi, Vadim N. Smelyanskiy, and Sergio Boixo. Quantum algorithms to simulate many-body physics of correlated fermions. *Phys. Rev. Applied*, 9:044036, Apr 2018.

[228] Barcelona Supercomputing Center. Marenostrum 4.

[229] Stavros Efthymiou, Sergi Ramos-Calderer, Carlos Bravo-Prieto, Adrián Pérez-Salinas, Diego García-Martín, Artur Garcia-Saez, José Ignacio Labashtorre, and

Stefano Carrazza. Qibo: a framework for quantum simulation with hardware acceleration. *Quantum Science and Technology*, 7(1):015018, dec 2021.

[230] Johnnie Gray. quimb: A python package for quantum information and many-body calculations. *Journal of Open Source Software*, 3(29):819, 2018.

[231] Sergio Sanchez-Ramirez, Javier Conejero, Francesc Lordan, Anna Queralt, Toni Cortes, Rosa M Badia, and Artur Garcia-Saez. RosneT: A block tensor algebra library for out-of-core quantum computing simulation. In *2021 IEEE/ACM Second International Workshop on Quantum Computing Software (QCS)*. IEEE, November 2021.

[232] Axel Pérez-Obiol, Adrián Pérez-Salinas, Sergio Sánchez-Ramírez, Bruna G. M. Araújo, and Artur Garcia-Saez. Adiabatic quantum algorithm for artificial graphene, 2022.

[233] Michael A. Nielsen. The fermionic canonical commutation relations and the jordan-wigner transform. 2005.

[234] Volker Bach, Elliott H. Lieb, and Jan Philip Solovej. Generalized hartree-fock theory and the hubbard model. *Journal of Statistical Physics*, 76(1-2):3–89, July 1994.

[235] Jarrod R McClean et al. OpenFermion: the electronic structure package for quantum computers. *Quantum Science and Technology*, 5(3):034014, jun 2020.

[236] Cirq Developers. Cirq, August 2021.

[237] M. Born and V. Fock. Beweis des adiabatensatzes. *Zeitschrift für Physik*, 51(3-4):165–180, March 1928.

[238] Joseph E. Avron and Alexander Elgart. Adiabatic theorem without a gap condition. *Communications in Mathematical Physics*, 203(2):445–463, June 1999.

[239] Seth Lloyd. Universal quantum simulators. *Science*, 273(5278):1073–1078, August 1996.